Thulium Doped Garnets for Quantum Repeaters and Optical Quantum Memory

Davidson, J.H.

DOI
10.4233/uuid:4533fe3c-f5ed-495a-ae15-67ce2cdc80df

Publication date
2022

Document Version
Final published version

Citation (APA)
Davidson, J. H. (2022). *Thulium Doped Garnets for Quantum Repeaters and Optical Quantum Memory*. [Dissertation (TU Delft), Delft University of Technology]. https://doi.org/10.4233/uuid:4533fe3c-f5ed-495a-ae15-67ce2cdc80df

THULIUM DOPED GARNETS FOR QUANTUM REPEATERS AND OPTICAL QUANTUM MEMORY

THULIUM DOPED GARNETS FOR QUANTUM REPEATERS AND OPTICAL QUANTUM MEMORY

Dissertation

for the purpose of obtaining the degree of doctor
at Delft University of Technology,
by the authority of the Rector Magnificus Prof.dr.ir. T.H.J.J. van der Hagen;
Chair of the Board for Doctorates
to be defended publicly on
Thursday 17th of February 2022 at 15:00 o'clock

by

Jacob Harley DAVIDSON

Masters of Science in Physics and Astronomy,
University of Calgary, Alberta, Canada
born in Philadelphia, Pennsylvania, United States of America.

This dissertation has been approved by the promotors.

promotor: prof. dr. W. Tittel
copromotor: prof.dr.ir. R. Hanson

Composition of the promotion committee:

Rector Magnificus,	voorzitter
Prof. dr. W. Tittel,	Technische Universiteit Delft
Prof. dr. ir. R. Hanson,	Technische Universiteit Delft
Independent Members:	
Prof. dr. ir. L.M.K. Vandersypen,	Technische Universiteit Delft
Dr. J. Borregaard,	Technische Universiteit Delft
Prof. dr. J.D. Thompson,	Princeton University
Prof. dr. D.D Awschalom ,	University of Chicago
Prof. dr. ir. H. De Riedmatten,	Institut de Ciencies Fotoniques
Reserve member:	
Prof. dr. S. Otte,	Technische Universiteit Delft

Printed by: Gildeprint

ISBN 000-00-0000-000-0

An electronic version of this dissertation is available at
http://repository.tudelft.nl/.

I say, when life gives you a lemon, wing it right back and add some lemons of your own!

- Bill Waterson

CONTENTS

SUMMARY

Quantum memories will prove to be an invaluable tool for distributing entangled quantum states over distance. Many novel materials for this purpose are being investigated and key among them are rare earth ion doped crystals. These materials possess a great number of potential combinations of host crystal and ion species for further study, some of which will likely be used to create the first quantum repeaters. Choosing a specific combination, thulium doped garnets, and a unique goal of making memory devices which can function simultaneously across many spectral channels, I take a unique perspective through which to push the performance of quantum memories.

I first describe the broad framework of quantum information science, and highlight the narrower scope of this thesis, a single device in the whole scheme, an optical quantum memory. Indeed, these memories are designed for use in a particular kind of quantum repeater, a frequency multiplexed quantum repeater, that defines its own set of criteria for determining what makes a good quantum memory (Chapters 1 & 2). This thesis then focuses on detailing a route from preliminary results to improved memory properties based upon detailed spectroscopic measurements, coherent population excitation, and construction of impedance matched optical cavities.

The results of the early experiments in this thesis demonstrate clearly that these thulium doped garnet materials show promise for this application if a few key hurdles can be overcome. First, using Tm:YAG, I demonstrate storage of heralded single photons in an impedance matched cavity quantum memory. We show that efficiency gains for weakly absorbing materials can be made even for heralded single photons, and how they rely on designing improved light matter interaction using critically coupled cavities (Chapter 3).

To extend another key parameter of our memories, I switch to a new garnet material Tm:YGG. Optical coherence of over 1 ms, and storage of classical pulses for 100 μs make this host immediately a potential quantum memory candidate. Additionally, this investigation allows a glimpse of the huge multiplexing capacity that is a requirement for frequency multiplexed quantum repeaters (Chapter 4).

The limits of these experiments indicate clear avenues for improvement in memory parameters that are pursued through the remaining chapters. To build improved monolithic cavity devices at a large scale I take a pair of routes detailed in chapters 5 & 6. The first is to determine the optical properties of relatively unknown Tm:YGG material and develop a nano fabrication process for constructing thin film cavity mirrors directly on this rare earth ion doped crystal.

In addition to the material properties, the second avenue is to improve our knowledge of the ion's magnetic properties, which is essential to crafting well understood AFC quantum memories. I confirm the ion site structure, determine the level splittings as a function of magnetic field, and identify optical clock transitions in the thulium ion spin Hamiltonian.

Applying our newfound knowledge, I use a frequency dependent rate equation model of Tm:YGG to explain and improve our optical initialization process for the memory transition (Chapter 7). With the addition of adiabatic pulse shaping for coherent population excitation, I describe the concrete causes and effects between the experimental limits of our optical initialization process, spectral diffusion over long time scales, and the resulting memory features.

I conclude (Chapter 8) with the outlook for thulium doped garnet materials, and their use as quantum memories in frequency multiplexed quantum repeaters. I discuss a concrete path forwards for creating further improvements to our second generation of optical quantum memory devices.

The results of this thesis show the potential of rare earth ion doped materials, in particular thulium doped garnets, in the quickly developing field of optical quantum memories, and quantum repeaters. More specifically, they demonstrate the link between basic material science, spectroscopy, and the resulting improvements in quantum memory performance.

SAMENVATTING

Kwantumgeheugens zullen een hulpmiddel van onschatbare waarde blijken te zijn voor het distribueren van verstrengelde kwantumtoestanden over afstand. Veel nieuwe materialen voor dit doel worden onderzocht en de belangrijkste daarvan zijn zeldzame-aarde-ionen gedoteerde kristallen. Deze materialen bevatten een groot aantal mogelijke combinaties van gastheerkristal en ionensoorten voor verder onderzoek, waarvan sommige waarschijnlijk zullen worden gebruikt om de eerste kwantumrepeaters te maken. Door een specifieke combinatie te kiezen, met thulium gedoteerde granaten en een uniek doel om geheugenapparaten te maken die tegelijkertijd over vele spectrale kanalen kunnen functioneren, neem ik een uniek perspectief om de prestaties van kwantumherinneringen te stimuleren.

Ik beschrijf eerst het brede raamwerk van kwantuminformatiewetenschap, en benadruk de beperkte reikwijdte van dit proefschrift, een enkel apparaat in het hele schema, een optisch kwantumgeheugen. Deze geheugens zijn inderdaad ontworpen voor gebruik in een bepaald soort kwantumrepeater, een frequentiegemultiplexte kwantumrepeater, die zijn eigen set criteria definieert om te bepalen wat een goed kwantumgeheugen is (hoofdstukken 1 en 2). Dit proefschrift richt zich vervolgens op het detailleren van een route van voorlopige resultaten naar verbeterde geheugeneigenschappen op basis van gedetailleerde spectroscopische metingen, coherente populatie-excitatie en constructie van op impedantie afgestemde optische holtes.

De resultaten van de vroege experimenten in dit proefschrift laten duidelijk zien dat deze met thulium gedoteerde granaatmaterialen veelbelovend zijn voor deze toepassing als een paar belangrijke hindernissen kunnen worden overwonnen. Ten eerste, met behulp van Tm:YAG, demonstreer ik opslag van aangekondigde enkele fotonen in een kwantumgeheugen met aangepaste holte met impedantie. We laten zien dat efficientiewinsten voor zwak absorberende materialen kunnen worden behaald, zelfs voor aangekondigde enkelvoudige fotonen, en hoe ze afhankelijk zijn van het ontwerpen van verbeterde interactie tussen licht en materie met behulp van kritisch gekoppelde holtes (Hoofdstuk 3).

Om een andere belangrijke parameter van ons geheugen uit te breiden, schakel ik over op een nieuw granaatmateriaal Tm:YGG. Optische coherentie van meer dan 1 ms en opsalg van klassieke pulsen voor 100 μs maken deze host onmiddellijk een potentiele kandidaat voor kwantumgeheugen. Bovendien geeft dit onderzoek een glimp van de enorme multiplexcapaciteit die een vereiste is voor frequentiegemultiplexte kwantumrepeaters (hoofdstuk 4).

De beperkingen van deze experimenten geven duidelijke wegen aan voor verbetering van geheugenparameters die in de resterende hoofdstukken worden nagestreefd. Om op grote schaal verbeterde monolithische holte-apparaten te bouwen, volg ik een paar routes die worden beschreven in de hoofdstukken 5 en 6. De eerste is om de optische eigenschappen van relatief onbekend Tm:YGG-materiaal te bepalen en een nanofabri-

cageproces te ontwikkelen voor het construeren van dunne-filmholtespiegels direct op dit zeldzame-aarde-ion-gedoteerde kristal.

Naast de materiaaleigenschappen, is de tweede weg om onze kennis van de magnetische eigenschappen van het ion te verbeteren, wat essentieel is voor het maken van goed begrepen AFC-kwantumgeheugens. Ik bevestig de structuur van de ionenplaats, bepaal de niveausplitsingen als functie van het magnetische veld, en identificeer optische klokovergangen in de thuliumion-spin Hamiltoniaan.

Door onze nieuwe kennis toe te passen, gebruik ik een frequentieafhankelijk snelheidsvergelijkingsmodel van Tm:YGG om ons optische initialisatieproces voor de geheugenovergang uit te leggen en te verbeteren (Hoofdstuk 7). Met de toevoeging van adiabatische pulsvorming voor coherente populatie-excitatie, beschrijf ik de concrete oorzaken en effecten tussen de experimentele limieten van ons optische initialisatieproces, spectrale diffusie over lange tijdschalen en de resulterende geheugenkenmerken.

Ik besluit (Hoofdstuk 8) met de vooruitzichten voor met thulium gedoteerde granaatmaterialen, en hun gebruik als kwantumgeheugens in frequentiegemultiplexte kwantumrepeaters. Ik bespreek een concreet pad voorwaarts voor het creeren van verdere verbeteringen aan onze tweede generatie optische kwantumgeheugenapparaten.

De resultaten van dit proefschrift tonen het potentieel aan van met zeldzame aarde gedoteerde materialen, in het bijzonder met thulium gedoteerde granaten, in het zich snel ontwikkelende veld van optische kwantumgeheugens en kwantumrepeaters. Meer specifiek demonstreren ze het verband tussen elementaire materiaalwetenschap, spectroscopie en de resulterende verbeteringen in de prestaties van het kwantumgeheugen.

1

INTRODUCTION

Whoever said that the definition of insanity is doing the same thing over and over again and expecting different results has obviously never had to reboot a computer.

William Petersen

Computers are commonplace, but they belong to a communication and computation infrastructure that took many years to develop. A time when quantum elements are part of this infrastructure is on the horizon. Now, as all the devices that will play key roles are being imagined and designed, people are crafting quantum information devices from many different physical systems. In this chapter I briefly discuss some of the general goals and frameworks that underpin the creation of useful quantum technology.

1

1.1. SMALLER IS STRONGER

QUANTUM mechanics has been one of the most successful theories for predicting the outcome of experiments in the natural world for just over a century now. The process of extending a quantum mechanical description of the world to more complex systems over larger distances is ongoing as quantum systems became more well understood from those initial theories long ago. In this time, a quantum mechanical description of just a few diverse systems has lead us to amazing advances in technology including our use of computers, lasers, and more, that have changed every aspect of how we live our lives [1, 2].

This trend can be expected to continue for reasons that are at least two fold. The first is the well known and somewhat ironically[1] named Moore's law [3] which states that the number of transistors per computer chip can be observed to roughly double every two years. Mr. Moore, back in 1965, was also "crazy" enough to predict technology we know and love today such as the cell phone and personal computer with which I write this very document. He predicted this law could last maybe 10 years, but half a century later his prediction still rings true. Smaller components in higher quantities have come year after year, and transistors today can reach the 7 nm scale with 2 nm well on the way [4]. This shrinking of the corner stone of computers has allowed machines to increase in power while maintaining reasonable size and energy capacity. The many minds who have developed quantum mechanics have a lot to say about the physics of objects on the angstrom scale that these devices are steadily approaching. If the doubling, and the benefits derived therein, is to continue, quantum effects will only become more important in the design of newer, faster, more efficient technologies that keep on pace with Mr. Moore's exponential prediction.

Alongside this idea, one of the first to consider this process of miniaturization of technology was Feynman with his speech "There is plenty of room at the bottom" [5]. However, interestingly enough, there is even more potential benefit to be had than simple sizing gains. The other side of this race to the bottom is the potential for a quantum advantage.

Today's information devices rely on different implementations of bits, 1s and 0s that are capable of performing algorithms to complete tasks. Operations on a set of bits belongs to the realm of Boolean algebra from which all computing logic has blossomed over the past half century [6]. However, working instead with quantum bits, termed qubits, the available state space becomes larger and the special properties of entanglement and super-position become resources [7–9]. These added properties have been shown in a number of contexts to have benefits for completing the tasks we often set for modern computers such as searching huge amounts of data, solving extremely complex mathematical problems and simulations, and even providing secure communication over networks. Additionally, if we can make the needed hardware, problems which have no solution on today's strongest machines show potential for success [10, 11]. Putting these appealing features together with the sizing trend of current computing devices it seems clear that the future for machines with higher capabilities will rely on continued progress mastering quantum mechanical properties.

[1] Mr.Moore's law of lots **more** transistors.

Taking a glance, in the way that Moore has done, at quantum scaling [12–14], considering qubits instead of transistors as the most basic element, ignoring the skeptics [15–17] and the additional complexity behind connectivity and circuit depth [18, 19], potentially places success during my lifetime in the 2040s or 2050s. With that optimism in hand the following section breaks the field down into a few different sub-areas in which research groups and companies alike look to make progress towards demonstrating that the quantum properties of real systems show benefits for working technology.

1.2. QUANTUM INFORMATION TECHNOLOGY

Quantum effects are the beating heart of a number of different technologies that are all emerging today [20]. There are proven benefits to each of the major categories listed below, but there also remains the untapped potential for new technology, in the way that no one could imagine the benefits of the computers and the internet of today before their invention.

- **Quantum Computing** Starting with the sub-area that has received the most press, the task of constructing a universal quantum computer is a major goal [21, 22]. The field has already progress to what is referred to the NISQ era of noisy intermediate scale quantum machines with 50 to 100 qubits. The ideal machine itself will posses classical components and well controlled quantum hardware that is capable of performing even more complex quantum algorithms, for example [23, 24],which have been proven to provide speed ups for difficult problems compared to a classical computer. In fact the entire field of complexity theory has begun to take notice as the answer to a mathematical millennium problem shares a close connection to quantum computing complexity [25, 26]. Work in this field focuses on building, testing and scaling hardware that can reach the appropriate size to perform useful algorithms. This often involves engineering a universal gate set of interactions between many qubits to form a larger processor [27], but there do exist other more exotic approaches [28]. Quantum computers are reliant on the potential for quantum error correction that will hopefully lead to fault tolerance [29, 30].

- **Quantum Simulation** While quantum computing aims for hardware that can be programmed to tackle any problem, quantum simulation is a closely related sub-area that looks to gain deeper understanding about certain highly controllable quantum systems and models [31]. Thus, quantum computing is to digital computers as quantum simulation is to analog machines that are more specific in their purpose, but may have potential to unlock new understanding about the underlying physics of the quantum system they attempt to simulate [32]. Building, controlling, and modeling large interacting quantum systems is currently the target for many in the field as this task remains extremely difficult for classical technology[7]. This field hearkens back closely to the ideas of Feynman and his ideas of simulating a quantum universe with a controlled quantum device [33, 34].

- **Quantum Sensing** The goal of quantum sensing is to build devices that can measure properties of the natural world with improved precision or accuracy com-

pared to the classical case [35]. Quantum sensors seek to measure all types of quantities from magnetic fields produced by single atoms within larger molecules [36], to macroscopic properties such as quantum radar [37], and even increments of time using to most accurate clocks to ever exist [38]. Not all natural properties can be measured with a single implementation, but new physics is discovered every day which leads to development of improved quantum sensors.

- **Quantum Networking and Cryptography** Whether to communicate between different cities and countries, or to tie together different portions of a universal quantum computer, quantum networking seeks to distribute arbitrary quantum states over distance [39]. Additionally there are also a number of protocols for secure communication [40–42], blind quantum computing [43], and quantum voting [44] which put quantum networking on the forefront of cryptography. While most more advanced quantum networking applications and hardware are still in the research and development phase [45], the first quantum cryptography machines with security beyond that of classical algorithms are already for sale commercially [46]. A number of different schemes exist to overcome major inefficiencies in distribution[47–49], and many different physical platforms are currently being investigated to serve as the basis for different components of a complete network[50–53].

Members of the each sub-field are looking for winning systems that can perform a useful task better than any possible classical counter part. To give guidelines for which physical systems hold the most potential there exists a set of fairly loose yet useful qualities, called the Divincenzo criteria [54],to look for in quantum systems that hold potential. Certain of these criteria become more important in each of the different subfields above but all of them require a rigorous understanding of the physical system in question. Physical systems for which the community has the deepest understanding and which fit well within the Divincenzo criteria are well positioned to become building blocks of tomorrow's quantum technology.

1.3. QUANTUM REPEATERS FOR QUANTUM NETWORKING

Classical infrastructure for communication and distributing information around the globe exists today and the way in which it was developed shows a decent potential route towards success for the quantum case. The infrastructure we use today evolved from the early days laying undersea telegraph cables to modern fiber optic internet [55]. This evolution has been in constant flux to allow the faithful transmission of information at an ever increasing rate.

Current telecommunications networks rely on nodes which attempt to communicate with one another, carriers to transmit the information over distance, and a way of encoding the desired message signals in the carrier so that each node can recover the transmitted information [56]. Each implementation of these elements comes with its own challenges which have required mastery of the theory and hardware behind everything from Morse code and AM/FM radio modulation, to creating and detecting extremely short pulses of light.

One such element of modern networks that becomes particularly important when extending to the quantum version is called a repeater. An element required to strengthen and boost signals as they are lost due to attenuation over long distances [57]. In the classical case this is done by amplification of the starting signal, or a copying of the initial signal to ensure it is capable of reaching the end point. This strategy is an impossibility in the quantum case [58, 59] making the task of constructing a quantum repeater an ongoing challenge that will be one focus of this thesis.

There are a number of proposals currently being researched to extend the distance over which quantum information carriers can distribute a quantum state [60]. The merits of a functioning repeater are judged on the rate at which it can distribute entangled states, the quality or fidelity of the entangled state created, and the distance over which a given repeater can function for its given resources. One strategy which does not produce entanglement but can still accomplish some initial goals, involves trusted nodes where the quantum information is entirely decoded and measured to become a set of classical outcomes along the route [61]. Another is to create large cluster states of entangled signal carriers or photons [62, 63]that rely on quantum error correction to produce entanglement[29]. However, currently, the most common strategy for building quantum repeaters relies on assembling a chain of entangled segments each of a shorter limited length,termed an elementary link. If an entangled state can be reliably generated along each individual piece of the chain then through entanglement swapping [64], the entire chain can be connected to create long distance entanglement[65].

Each link of the established chain relies on a number of different devices that have been demonstrated individually before. This includes quantum memories [66], another main subject of this thesis, as well as entangled photon sources [67], and finally Bell state measurements [68], a key operation for entanglement swapping.

However even with versions of all of these devices working perfectly, for a quantum network to truly succeed there must be many channels acting simultaneously, so called multiplexing, to reach useful rates of entanglement and communication. To facilitate multiplexing, there must be some degree of freedom which differentiates one channel from another, either in time, space, shape, color, etc. [69]. The number of channels or modes available using any combination of these methods will need to be capable of reaching into the thousands or millions to counteract the effects of lossy channels and imperfect devices while attempting to generate long distance entanglement.

1.4. THESIS OVERVIEW

With this firm backing, the remainder of this thesis centers on the creation of a quantum memories made from rare earth ion doped crystals [66, 70], required for building elementary links of quantum repeaters [71]. These devices will be shown to be capable of performing some of the networking tasks discussed above[72]. There is hope that they might enable the building of quantum networks for multiplexed high rate entanglement generation across long distances[48, 52, 73].

- **Chapter** 2 picks up here and leads from a discussion of frequency multiplexed quantum repeaters [74] through atomic frequency comb quantum memories [75] built from rare earth ion doped crystals to the specific materials used in this thesis.

- **Chapter** 3 shows a promising initial result in which a Tm doped garnet crystal is used for storage of heralded single photons in an impedance matched cavity AFC quantum memory.
- In **chapter** 4 As another initial result, the main shortcoming of the previous chapter, short storage time, is improved by switching to a different garnet material to create a single pass optical quantum memory. This result foreshadows the creation of improved devices with significantly improved efficiencies and storage times together.
- **Chapter** 5 details measurements of material properties that underpin fabrication of these improved devices out of the yttrium gallium garnet material. This chapter also include details about the nano fabrication process of creating Bragg mirrors on these garnet materials to realize the cavity devices discussed in chapter 3.
- In **chapter** 6 I dive into a detailed material study of the dopant ions in Tm:YGG to determine their magnetic hyperfine tensors. This study results in information about the magnetic behavior, needed to put our understanding about Tm:YGG on equal footing with Tm:YAG, and reveals special orientations of external magnetic fields that potentially allow increasing atomic coherence through use of clock transitions.
- In **chapter** 7 we turn the question of how to understand, improve, and optimize the optical pumping process for creating AFC quantum memories in Tm:YGG. This includes adiabatic pulse design and shaping for pump pulses, fitting frequency dependent rate equation models for said optical pumping to spectral hole burning results, and the change of those spectral features over time with the addition of magnetic spectral diffusion processes.
- **Chapter** 8 gives an outlook on the potential for future studies in Tm doped garnets, optical quantum memories for frequency multiplexed quantum repeaters, and quantum networking.

BIBLIOGRAPHY

[1] R. Feynman, R. Leighton, and M. Sands, *The feynman lectures on physics*, Addison-Wesley world student series (Addison-Wesley Publishing Company, 1963).

[2] J. P. Dowling and G. J. Milburn, "Quantum technology: the second quantum revolution", Philosophical Transactions of the Royal Society of London. Series A: Mathematical, Physical and Engineering Sciences **361**, 1655–1674 (2003).

[3] G. E. Moore, "Cramming more components onto integrated circuits, reprinted from electronics, volume 38, number 8, april 19, 1965, pp.114 ff.", IEEE Solid-State Circuits Society Newsletter **11**, 33–35 (2006).

[4] N. Loubet et al., "Stacked nanosheet gate-all-around transistor to enable scaling beyond finfet", in 2017 symposium on vlsi technology (2017), T230–T231.

[5] R. P. Feynman, "There's plenty of room at the bottom [data storage]", Journal of Microelectromechanical Systems **1**, 60–66 (1992).

[6] J. Whitesitt, *Boolean algebra and its applications*, Dover Books on Computer Science (Dover Publications, 2012).

[7] A. S. Holevo, "Bounds for the quantity of information transmitted by a quantum communication channel", Problemy Peredachi Informatsii **9**, 3–11 (1973).

[8] A. Einstein, B. Podolsky, and N. Rosen, "Can quantum-mechanical description of physical reality be considered complete?", Phys. Rev. **47**, 777–780 (1935).

[9] J. S. Bell, "On the einstein podolsky rosen paradox", Physics Physique Fizika **1**, 195–200 (1964).

[10] D. Deutsch and R. Jozsa, "Rapid solution of problems by quantum computation", Proceedings of the Royal Society of London. Series A: Mathematical and Physical Sciences **439**, 553–558 (1992).

[11] R. Cleve, A. Ekert, C. Macchiavello, and M. Mosca, "Quantum algorithms revisited", Proceedings of the Royal Society of London. Series A: Mathematical, Physical and Engineering Sciences **454**, 339–354 (1998).

[12] I. L. Chuang, N. Gershenfeld, and M. Kubinec, "Experimental implementation of fast quantum searching", Phys. Rev. Lett. **80**, 3408–3411 (1998).

[13] F. Arute et al., "Quantum supremacy using a programmable superconducting processor", Nature **574**, 505–510 (2019).

[14] H.-S. Zhong et al., "Quantum computational advantage using photons", Science **370**, 1460–1463 (2020).

[15] M. Dyakonov, *Will we ever have a quantum computer?*, SpringerBriefs in physics (Springer, 2020).

[16] G. Kalai and G. Kindler, "Gaussian noise sensitivity and bosonsampling", arXiv preprint arXiv:1409.3093 (2014).

[17] J. Gea-Banacloche, "Minimum energy requirements for quantum computation", Phys. Rev. Lett. **89**, 217901 (2002).

[18] A. W. Cross, L. S. Bishop, S. Sheldon, P. D. Nation, and J. M. Gambetta, "Validating quantum computers using randomized model circuits", Phys. Rev. A **100**, 032328 (2019).

[19] A. Y. Kitaev, "Fault-tolerant quantum computation by anyons", Annals of Physics **303**, 2–30 (2003).

[20] A. Acın et al., "The quantum technologies roadmap: a european community view", New Journal of Physics **20**, 080201 (2018).

[21] European Comission, *Quantum Technologies Flagship*, https://digital-strategy.ec.europa.eu/en/policies/quantum-technologies-flagship, 2021.

[22] 115th Congress of the United States, *NATIONAL QUANTUM INITIATIVE ACT*, https://www.quantum.gov/, 2018.

[23] L. K. Grover, "A fast quantum mechanical algorithm for database search", in Proceedings of the twenty-eighth annual acm symposium on theory of computing, STOC '96 (1996), pp. 212–219.

[24] P. W. Shor, "Polynomial-time algorithms for prime factorization and discrete logarithms on a quantum computer", SIAM Journal on Computing **26**, 1484–1509 (1997).

[25] A. M. S. S. Course, S. Lomonaco, and A. M. Society, *Quantum computation: a grand mathematical challenge for the twenty-first century and the millennium : american mathematical society, short course, january 17-18, 2000, washington, dc*, AMS short course lecture notes (American Mathematical Society, 2002).

[26] Stephen Cook, *THE P VERSUS NP PROBLEM*, https://www.claymath.org/millennium-problems/p-vs-np-problem, 1971.

[27] J. Preskill, "Quantum Computing in the NISQ era and beyond", Quantum **2**, 79 (2018).

[28] H. J. Briegel, D. E. Browne, W. Dür, R. Raussendorf, and M. Van den Nest, "Measurement-based quantum computation", Nature Physics **5**, 19–26 (2009).

[29] P. W. Shor, "Scheme for reducing decoherence in quantum computer memory", Phys. Rev. A **52**, R2493–R2496 (1995).

[30] J. Preskill, "Fault-tolerant quantum computation", in *Introduction to quantum computation and information* (World Scientific, 1998), pp. 213–269.

[31] I. M. Georgescu, S. Ashhab, and F. Nori, "Quantum simulation", Rev. Mod. Phys. **86**, 153–185 (2014).

[32] J. I. Cirac and P. Zoller, "Goals and opportunities in quantum simulation", Nature Physics **8**, 264–266 (2012).

[33] R. Feynman, "Engineering & science magazine", California Institute of Technology, USA (1960).

[34] R. P. Feynman, "Simulating physics with computers", International Journal of Theoretical Physics **21**, 467–488 (1982).

[35]C. L. Degen, F. Reinhard, and P. Cappellaro, "Quantum sensing", Rev. Mod. Phys. **89**, 035002 (2017).

[36]M. H. Abobeih, J. Randall, C. E. Bradley, H. P. Bartling, M. A. Bakker, M. J. Degen, M. Markham, D. J. Twitchen, and T. H. Taminiau, "Atomic-scale imaging of a 27-nuclear-spin cluster using a quantum sensor", Nature **576**, 411–415 (2019).

[37]S. Barzanjeh, S. Pirandola, D. Vitali, and J. M. Fink, "Microwave quantum illumination using a digital receiver", Science Advances **6**, eabb0451 (2020).

[38]N. Huntemann, C. Sanner, B. Lipphardt, C. Tamm, and E. Peik, "Single-ion atomic clock with 3×10^{-18} systematic uncertainty", Phys. Rev. Lett. **116**, 063001 (2016).

[39]H. J. Kimble, "The quantum internet", Nature **453**, 1023–1030 (2008).

[40]H.-K. Lo, M. Curty, and B. Qi, "Measurement-device-independent quantum key distribution", Phys. Rev. Lett. **108**, 130503 (2012).

[41]C. H. Bennett and G. Brassard, "Quantum cryptography: public key distribution and coin tossing", Theoretical Computer Science **560**, Theoretical Aspects of Quantum Cryptography – celebrating 30 years of BB84, 7–11 (2014).

[42]M. Lucamarini, Z. L. Yuan, J. F. Dynes, and A. J. Shields, "Overcoming the rate–distance limit of quantum key distribution without quantum repeaters", Nature **557**, 400–403 (2018).

[43]A. M. Childs, Quantum Information and Computation **5**, 10.26421/qic5.6 (2005).

[44]M. Hillery, M. Ziman, V. Bužek, and M. Bieliková, "Towards quantum-based privacy and voting", Physics Letters A **349**, 75–81 (2006).

[45]S. Wehner, D. Elkouss, and R. Hanson, "Quantum internet: a vision for the road ahead", Science **362**, eaam9288 (2018).

[46]ID Quantique, *Quantum-Safe Security*, https://www.idquantique.com/quantum-safe-security/overview/, 2021.

[47]L.-M. Duan, M. D. Lukin, J. I. Cirac, and P. Zoller, "Long-distance quantum communication with atomic ensembles and linear optics", Nature **414**, 413–418 (2001).

[48]C. Simon, H. de Riedmatten, M. Afzelius, N. Sangouard, H. Zbinden, and N. Gisin, "Quantum repeaters with photon pair sources and multimode memories", Phys. Rev. Lett. **98**, 190503 (2007).

[49]T. Pellizzari, "Quantum networking with optical fibres", Phys. Rev. Lett. **79**, 5242–5245 (1997).

[50]S. Ritter et al., "An elementary quantum network of single atoms in optical cavities", Nature **484**, 195–200 (2012).

[51]M. Pompili et al., "Realization of a multinode quantum network of remote solid-state qubits", Science **372**, 259–264 (2021).

[52]D. Lago-Rivera, S. Grandi, J. V. Rakonjac, A. Seri, and H. de Riedmatten, "Telecom-heralded entanglement between multimode solid-state quantum memories", Nature **594**, 37–40 (2021).

[53] I. V. Inlek, C. Crocker, M. Lichtman, K. Sosnova, and C. Monroe, "Multispecies trapped-ion node for quantum networking", Phys. Rev. Lett. **118**, 250502 (2017).

[54] D. P. DiVincenzo, "The physical implementation of quantum computation", Fortschritte der Physik: Progress of Physics **48**, 771–783 (2000).

[55] A. Clarke, *How the world was one*, Author Portal Arthur C Clarke (Orion, 2011).

[56] R. Gallager, *Principles of digital communication* (Cambridge University Press, 2008).

[57] B. Lathi and Z. Ding, *Modern digital and analog communication systems*, Oxford Series in Electrical an (Oxford University Press, 2009).

[58] M. A. Nielsen and I. Chuang, *Quantum computation and quantum information*, 2002.

[59] W. K. Wootters and W. H. Zurek, "A single quantum cannot be cloned", Nature **299**, 802–803 (1982).

[60] W. J. Munro, K. Azuma, K. Tamaki, and K. Nemoto, "Inside quantum repeaters", IEEE Journal of Selected Topics in Quantum Electronics **21**, 78–90 (2015).

[61] T.-Y. Chen et al., "Implementation of a 46-node quantum metropolitan area network", npj Quantum Information **7**, 134 (2021).

[62] K. Azuma, K. Tamaki, and H.-K. Lo, "All-photonic quantum repeaters", Nature Communications **6**, 6787 (2015).

[63] J. Borregaard, H. Pichler, T. Schröder, M. D. Lukin, P. Lodahl, and A. S. Sørensen, "One-way quantum repeater based on near-deterministic photon-emitter interfaces", Phys. Rev. X **10**, 021071 (2020).

[64] J.-W. Pan, D. Bouwmeester, H. Weinfurter, and A. Zeilinger, "Experimental entanglement swapping: entangling photons that never interacted", Phys. Rev. Lett. **80**, 3891–3894 (1998).

[65] H.-J. Briegel, W. Dür, J. I. Cirac, and P. Zoller, "Quantum repeaters: the role of imperfect local operations in quantum communication", Phys. Rev. Lett. **81**, 5932–5935 (1998).

[66] A. I. Lvovsky, B. C. Sanders, and W. Tittel, "Optical quantum memory", Nature Photonics **3**, 706–714 (2009).

[67] X. Ma, C.-H. F. Fung, and H.-K. Lo, "Quantum key distribution with entangled photon sources", Phys. Rev. A **76**, 012307 (2007).

[68] N. Lütkenhaus, J. Calsamiglia, and K.-A. Suominen, "Bell measurements for teleportation", Phys. Rev. A **59**, 3295–3300 (1999).

[69] J. Wang et al., "Terabit free-space data transmission employing orbital angular momentum multiplexing", Nature Photonics **6**, 488–496 (2012).

[70] G. Liu and B. Jacquier, *Spectroscopic properties of rare earths in optical materials*, Vol. 83 (Springer Science & Business Media, 2006).

[71] N. Sangouard, C. Simon, H. de Riedmatten, and N. Gisin, "Quantum repeaters based on atomic ensembles and linear optics", Rev. Mod. Phys. **83**, 33–80 (2011).

[72] W. Tittel, M. Afzelius, T. Chaneliére, R. Cone, S. Kröll, S. Moiseev, and M. Sellars, "Photon-echo quantum memory in solid state systems", Laser & Photonics Reviews **4**, 244–267 (2010).

[73] C. Simon et al., "Quantum memories", The European Physical Journal D **58**, 1–22 (2010).

[74] N. Sinclair et al., "Spectral multiplexing for scalable quantum photonics using an atomic frequency comb quantum memory and feed-forward control", Phys. Rev. Lett. **113**, 053603 (2014).

[75] M. Afzelius, C. Simon, H. de Riedmatten, and N. Gisin, "Multimode quantum memory based on atomic frequency combs", Phys. Rev. A **79**, 052329 (2009).

2

Rare Earth Ion Doped Crystals for Frequency Multiplexed Quantum Repeaters

What's the difference between a seal and a sea lion?
...
...
One electron.

Rare-Earth-Ion-Doped crystals (REIC) provide a promising platform for creating good quantum memories. In the general context of quantum repeaters, their large ensembles of stationary ions and easily addressable spin and optical transitions with long coherence times make for good avenues to create efficient light matter interaction. In this chapter I discuss the essential elements of quantum repeaters and provide background on what makes a good optical quantum memory. I will delve into the specifics of what makes rare earth ions attractive, including specifically thulium ions in garnet hosts.

2.1. FREQUENCY MULTIPLEXED QUANTUM REPEATERS

WITH the goal to distribute entangled quantum states over long distance we turn to more specific designs of quantum repeaters. Crafting a chain of elementary links to create a distributed entangled state means isolating a very sensitive quantum system over a large distance. Arguably the first versions of a full elementary link have just recently been demonstrated [1, 2], and though both demonstrations produce a flying entangled state at either side of the link, they suffer from inefficiencies that would prevent extending these exact devices over many adjacent links. The claims of [1] also take full advantage of temporal multiplexing in order to claim one of the fastest remote entanglement generation rates demonstrated thus far, while leaving room for further improvement. Each of these experiments assembles the main building blocks of a repeater in a configuration similar to Figure 2.1.

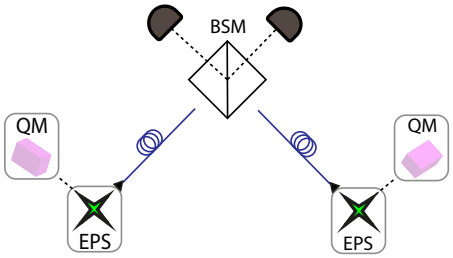

Figure 2.1: Impression of an elementary link based on three main components. They are labeled Quantum Memory (QM), Entangled Photon Pair Source (EPS), and Bell State Measurement (BSM). One photon per entangled pair is sent to the QM, the other to the BSM. Once two photons arrive at the BSM station, one from each EPS, they interfere on the beam beam splitter present there, and are detected. Information recorded in the detection patterns is returned classically to the quantum memories to herald the creation of entanglement between the two distant quantum memories by means of entanglement swapping

The process begins locally at two entangled photon pair sources. Often based on non-linear processes, with potential also demonstrated by quantum dots, these sources are still a broad area of research to generate the needed entangled quantum states [3, 4]. For each source, one member of the pair, usually at telecom frequency is transmitted over distance to a Bell state measurement, while the other is stored locally in a quantum memory. The telecom member, upon covering the needed distance is directed to a beam splitter, as is a matching photon from the other pair source, which has covered the other half of the distance [5]. With this pair of photons incident upon the same beam splitter, interference occurs, and the resulting detection pattern casts the pair into one of the four Bell states with a maximum success probability, often below 50%, that depends on the number of ancilla used and technical limitations from certain qubit encoding [6–8]. When a pair of photons produces a desired set of detections the result is reported classically back across the link to the two quantum memories, to herald which stored photons have been entangled. Each particular photon, or mode, is then allowed to transmit onward, outside of a single elementary link to create a shared state between multiple links.

Since the likelihood of success for a single mode or photon pair is quite small when totaling up the losses between generation, transmission, detection, and storage, many

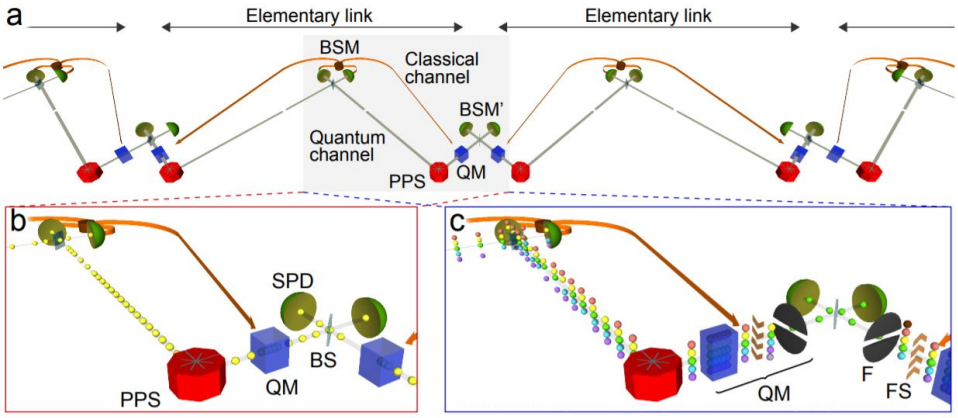

Figure 2.2: **a** Distribution of elementary links over distance. Each elementary link as described above is shown in sequence with additional BSM measurements to tie together entanglement from different elementary links. **b** Depicts roughly half of an elementary link as above, but with temporal multiplexing shown as a stream of successive photons in time. **c** The frequency multiplexed counterpart of part **b**. Note that there are many photons of different colors or frequencies transmitted simultaneously through the architecture. Figure reproduced from [14] with permission.

modes are required to produce a single successful attempt across the elementary link. This can be done by repeating the process described above in time, or by engineering many simultaneous signals in another degree of freedom. These different degrees of freedom include, polarization [9], spatial [10, 11], temporal [1, 12, 13], and frequency [14]. The first mode of these different repeater designs may work similarly, but the method of adding additional modes differs from case to case. These differences show themselves in the way that each of the individual repeater components must function to accommodate scaling to more modes.

For the frequency multiplexed case, a functioning repeater should generate entanglement at a rate and success probability described by [15]. As pictured in Figure 2.2, frequency multiplexed sources must emit simultaneous photon pairs at multiple frequencies. The memories must then be capable of simultaneously storing modes of many different colors, and the Bell state measurements must be able to produce results from interference at many simultaneous frequencies while differentiating successful results each particular mode. Additionally, there must be information fed-forward from a bell state measurement to the memory devices such that only successfully entangled frequency modes can be allowed to interfere with other elementary links. This places added complexity on constructing each of these devices, with the hope that in the long run the difficulty will lead to improved scaling for the multiplexing capacity to many, many more modes. Additionally, devices for this repeater design need to consider the spacing and bandwidth of each distinct frequency mode as key operating parameters to make the most of usable frequency space.

Frequency multiplexed sources and BSMs are current topics of research [3, 14, 16, 17], but the remainder of this thesis will focus on the quantum memories required for a frequency multiplexed quantum repeater. In my work, and in both of the repeater

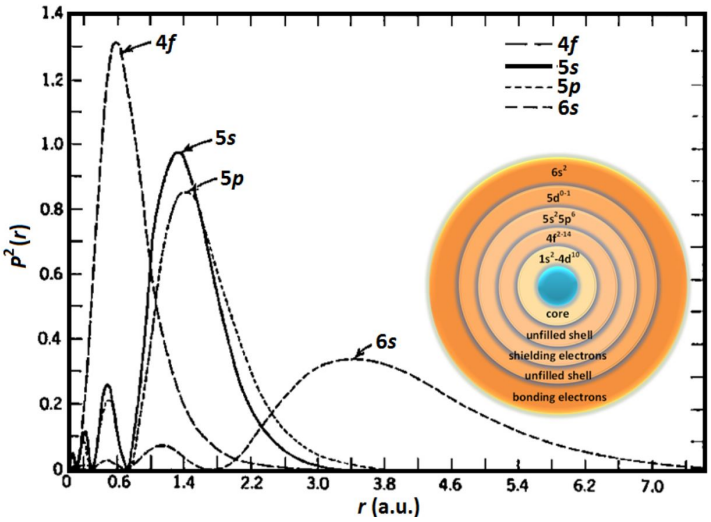

Figure 2.3: Radial probability distribution for the electrons of the $4f^N$ shell of rare earth ions. The curves corresponding to each shell are labeled compared to their relative radius. There is a noted difference in expected radius such that electrons in the 4f shell remain spatially isolated within the radius of most bonding and shielding electrons from the 5s and 5p shells. Figure reproduced with permission from (2012) V.A.G. Rivera. Originally published in [21] under CC BY 3.0 license.

demonstrations [1, 2], the optical quantum memory component of the link employs REIC and the atomic frequency comb (AFC) scheme for quantum memory, both of which will be described in the remainder of this chapter.

2.2. RARE EARTH ION DOPED CRYSTALS

To begin simply, nodes of a quantum networks and repeaters should stay still for us humans to interact with them. Thus, at the most basic level, nodes will be made of matter, because matter holds still. Rare earth ion doped crystals have proven an excellent source of matter to work with as they provide a fairly isolated ensemble of one particular species of atoms in a controlled environment. The crystals in question were initially investigated for their spectroscopic properties, and use in laser physics, but now show great promise in a number of fields [18–20]. The ions present can also be accessed without the complex engineering that goes into trapping ions and neutral molecules at extremely high vacuums or the excessively low temperatures of superconducting systems.

In many different crystals, atoms from the sixth row of the periodic table, the Lanthanides, often referred to as rare earths, form triply ionized defects that replace host ions at specific sites. Lanthanides are attractive because of the radial distribution of their electrons. Shown in Figure 2.3 is the radial distribution of electrons in the $4f^N$ shells for these ions.

The electrons in these shells lie spatially separated from the electrons involved in bonding to the host. In addition, asymmetries in the crystal field structure of these crystalline hosts cause a mixing of the wave functions for electrons of this shell that weakly

permit transitions that would otherwise be forbidden via selection rules. This combination of effects, electronic radius, and wave-function mixing, leads to long radiative lifetimes, and when cooled to cryogenic temperatures long optical and spin coherence times for transitions between levels of the $4f^N$ shells. These ions make an attractive platform, but there are still many different combinations of ion and host each of which possess optical transitions at different wavelengths, as well as differing surrounding level structure to be used for potential applications such as quantum memory.

There is a wealth of spectroscopic information available for different ion species in different host materials [18–20]. But the ultimate choices of ion and host species generally come down to the desired application, and the amount of background knowledge for a particular combination. Shown in Figure 2.4 are the calculated optical transitions of all the rare earth species for a single host crystal, lanthanum fluoride.

Depending on the application different properties of a particular ion host combination become important. For example, erbium and ytterbium ions are being built into nano-photonic cavities to become photon sources and interfaces between microwave and optical photons, respectively [22–24]. Erbium is selected for a source because it possesses a telecom wavelength transition at 1532nm that can also be seen in Figure 2.4. Meanwhile, ytterbium 171 is selected for transduction because of the many of ground and excited states in its hyperfine structure with splittings that can be tuned to match superconducting qubit frequencies. These are just a few examples, but they serve to show that the structure of the optical or spin transitions make a particular rare earth species attractive for a particular application. Research groups have interest in a number of particular ions for their properties at zero magnetic field including ZEFOZ transitions [25], frozen core effects [26], well understood crystal structure and easily accessible transitions [27], long coherence times [28], and more as each species of ion is slowly investigated further.

Just as important as the ion species is the host crystal. These days many host crystals are often grown by well controlled Czochralski growth methods which leads to very reproducible crystals with few impurities, and low strain [29, 30]. While changes to the optical and spin transition frequencies between different hosts are quite small, properties such as coherence times can change drastically [18, 31]. Host choice selects symmetry of the ion site as well as the noise environment that the ions will experience due to the host atomic composition. Some hosts such as Y_2SiO_5 have very few strong spins present leaving the magnetic dynamics within the crystal fairly weak compared to the added REI themselves[32].For other crystals like $LiNbO_3$ local spins in the crystalline environment have been shown to create super hyperfine splittings and echo modulations that can be either feature or bug [33]. Hosts such as the garnets that will be discussed throughout most of this thesis contain other atomic species, aluminum or gallium, which have spins that can actively reduce the lifetimes for REI of interest [34]. Still more hosts are attractive because coupling to local spins can provide a usable register for quantum information purposes [35].

Selecting a particular host and ion combination for a particular application can be a difficult task, so the final section of this chapter enumerates a number of key reasons why thulium doped garnet materials make a decent choice for optical quantum memory, particularly memories for frequency multiplexed quantum repeaters.

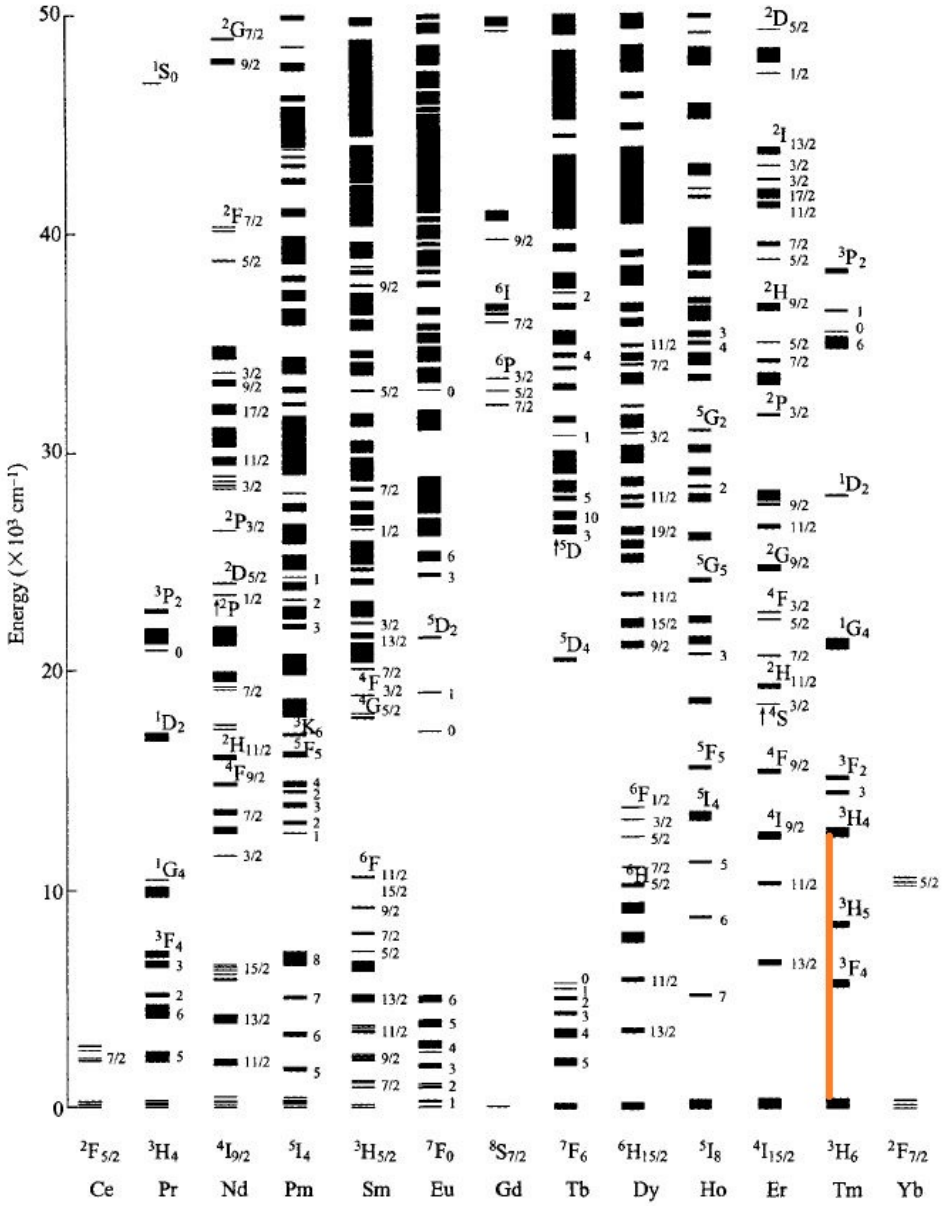

Figure 2.4: Transition energies calculated from free ion and crystal field terms of the ion Hamiltonian in Re^{3+} Lanthanum Fluoride. Each Rare earth has some relevant energy transitions. The optical transition in thulium for this work is shown in orange. Figure reproduced with alterations from [18] with permission.

2.3. AFC SCHEME FOR QUANTUM MEMORY

To create a quantum memory from a particular atomic absorption line, there are a number of different options [13]. This thesis focuses on creation of AFC quantum memories [36].

An atomic frequency comb quantum memory is a periodic spectral structure crafted from the inhomogeneous absorption line of a particular atomic transition. This spectral feature is pictured in Figure 2.5. Once light, classical or quantum, matching the bandwidth of the spectral structure has been absorbed by the remaining atoms the resulting state can be described as a Dicke state [37]

$$|\psi\rangle = \sum_{j=1}^{N} c_j e^{i2\pi\delta_j t} e^{-ikz_j} |g_1 ... e_j ... g_N\rangle \tag{2.1}$$

$$\text{for} \quad \delta_j = n\Delta \tag{2.2}$$

$$e^{i2\pi n\Delta t} = 1 \quad \text{for} \quad t = 1/\Delta. \tag{2.3}$$

Here, k is the the wave number, z the position in the crystal, c_j the amplitude of each component of the state, frequency detuning δ_j, and Δ the periodicity of the spectral structure. The resulting state is a sum over N, the number of ions, with the N terms each containing a single excitation of a different ion in the state vector shown in Eqn.7.1 . The dephasing of this state is given by the exponential factor $e^{i2\pi\delta_j t}$. However, it can rephase automatically. Indeed, when crafted correctly, the shape of the original AFC is periodic fulfilling the condition of Eqn.7.2, which makes the detunings δ_j of the atoms participating in the comb periodic as well. This results in a periodic rephasing of the exponential factor in Eqn.7.3 at the designated time, and a re-emission of an echo pulse of light determined by the periodicity of the AFC structure.

AFC memories have been shown to be effective for storage of quantum and classical light [14, 28, 38–40] making our goal now to improve our AFC quantum memories across a number of different figures of merit for the application of frequency multiplexed quantum repeaters.

- **Storage Time** An ideal optical quantum memory could be used to store pulses of light indefinitely and have them reproduced at some (potentially constant) requested time. For realistic quantum memories the time between storage and re-emission, either with an on demand, or fixed delay, should be limited by the coherence times of the transitions used for storage. In a real experiment, however, creation of good AFC memories often also comes down to technical limitations related to crafting optimal periodic spectral features. A discussion of the experimental limits to producing good AFC structures in Tm doped garnet materials is the focus of chapter 7. In some cases the storage time determines the distance over which a quantum repeater can operate [5], and also plays a role in the memory's multiplexing capacity discussed below. Current state of the art for light storage times are on the order of ms to minutes [28, 41]. Note that these experiments involve potentially inefficient and noisy transitions to atomic spin levels with longer lifetimes. For the frequency multiplexed case, storage times with a fixed delay, and thus coherence times, on the order of hundreds of microseconds can be sufficient [14, 42].

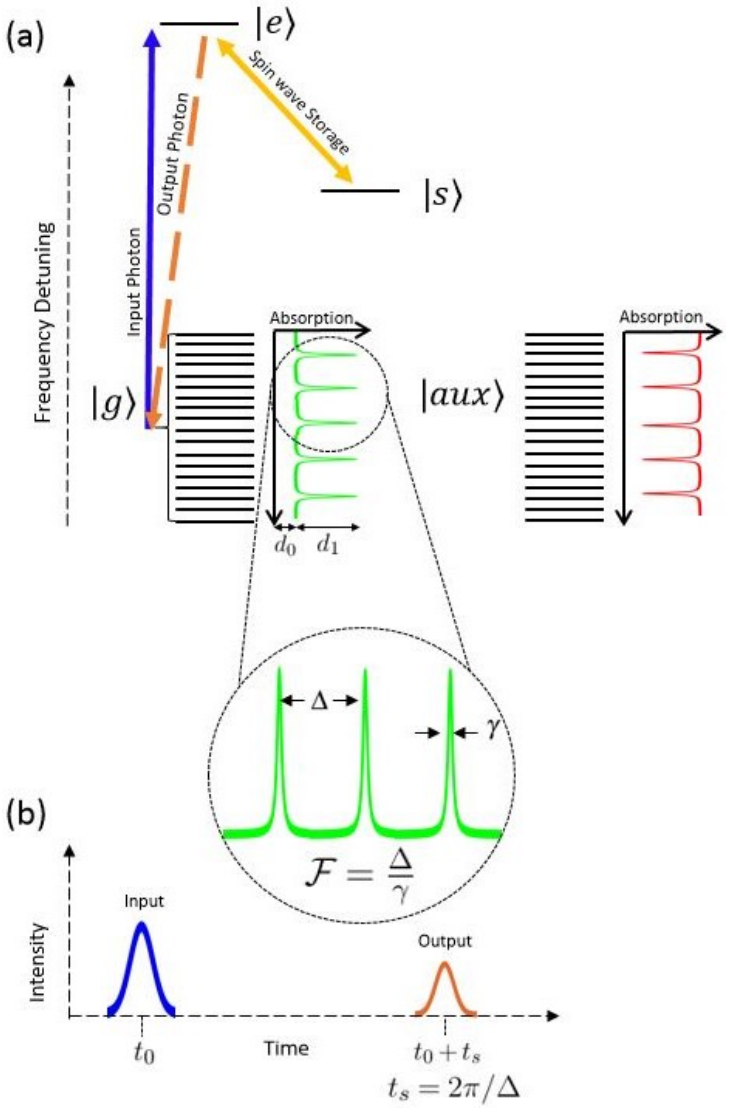

Figure 2.5: Pictured here is an arbitrary atomic level structure with inhomogeneous broadening including ground state, $|g\rangle$, excited state, $|e\rangle$, and nearby spin and auxiliary levels $|s\rangle$ and $|aux\rangle$. Atomic population at certain frequencies is pumped out of $|g\rangle$ and decays to $|aux\rangle$ leaving a periodic absorption structure (an AFC) over a certain bandwidth. When light at the frequency shown in blue spans the bandwidth of the AFC it is absorbed, creating a collective optical coherence between the ground and excited states of many atoms. Some interval later, determined by AFC tooth spacing, an echo pulse is re-emitted. This protocol also includes the possibility to transfer the optical coherence to the longer lived spin level $|s\rangle$ with a pair of control pulses at the frequency shown in yellow.

- **Efficiency** measures the ratio of energy output vs energy input for a quantum memory. For an ideal device it is unity, meaning no energy is lost in the storage process. For the case of single photons this metric becomes a matter of the likelihood that a photon incident on the memory will be stored and re-emitted after the storage time. Efficiency of AFC quantum memories can theoretically be nearly 100 % although in practice it is often limited by insufficient atomic absorption, and our inability to craft good spectral structures. A common expression for efficiency of AFC quantum memories assuming Gaussian shaped teeth is given by

$$\eta = (d_1/F)^2 e^{-7/F^2} e^{-d_1/F} e^{-d_0} \tag{2.4}$$

  Here d_1 is the optical depth of an AFC absorption peak, F is the finesse (the ratio of absorption peak spacing to peak width) and d_0 is the residual optical depth that does not form the desired spectral comb structure. Each of the four factors captures potential losses due to a different effect; likelihood of absorbing the input pulse, likelihood to re-phase any absorbed signal, likelihood for re-absorption of the echo signal, and loss due to absorption that cannot re-phase, respectively. Current state of the art in optical quantum memory efficiency is approximately 90%, but the most efficient AFC quantum memory demonstrations have been limited to 50-60% using a cavity based implementation [40, 43–48]. These results are extremely impressive, but also often come due to sacrifices in a number of the other figures of merit listed here. For creating repeaters, frequency multiplexed or otherwise, additional losses due to poor memory efficiency will be catastrophic. Figure 2.6 contains a good, if slightly outdated, summary of many quantum memory results based only on the metrics of storage time and efficiency.

- **Fidelity** describes the overlap between the input and output of the quantum memory where an ideal memory has a fidelity of one and the memory reproduces exactly the input quantum state. It is defined mathematically as:

$$F(\rho) = Tr\left(\sqrt{\sqrt{\rho'}\rho\sqrt{\rho'}}\right), \tag{2.5}$$

  where ρ is the density matrix of the input quantum state and ρ' the output. Fidelity above a bound of 2/3 certifies that an optical memory is indeed an optical quantum memory that outperforms any possible classical counterpart [49–52]. For an entire repeater, fidelity becomes extremely important as noise is expected to scale poorly [53] without methods such a purification. For AFC quantum memories high fidelities have been demonstrated since the efficiency is not included in the calculation for certain qubit implementations [54, 55]. Memory fidelity as high as possible is needed for fault tolerant quantum technology.

- **Bandwidth** Bandwidth of an optical quantum memory is the range of frequencies over which the memory can store information [56]. Larger bandwidth memories can store the shorter optical signals that are commonly created by current photon sources [3, 16]. Common bandwidths for AFC and other optical quantum memories are 1-10 MHz [43–46, 52], although strategies that sacrifice efficiency have

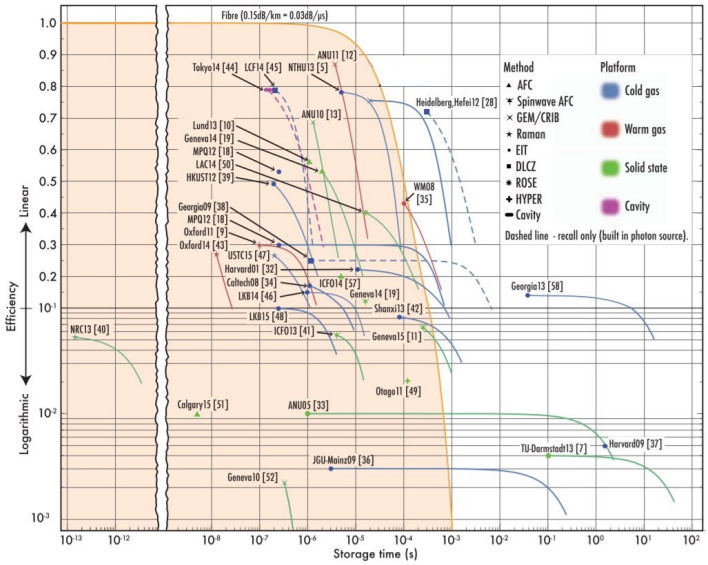

Figure 2.6: Comparison of many results in optical quantum memory across storage time and memory efficiency. Results are compared against a delay line of SMF-28 optical fiber at 1550nm. Figure Reprinted with permission from Ref.[45] © The Optical Society.

been employed to extend AFC quantum memories up to 10 GHz [57]. For AFC quantum memories, the theoretical bandwidth limitation is generally given by the hyperfine structure of the ion and the characteristics of the host crystal. Pump laser power in relation to the lifetimes of levels used to create the AFC is often an experimental limit for creating good spectral features over large bandwidths. In the frequency multiplexed case, though bandwidth of a single AFC channel is important, the additional figure of merit becomes the total bandwidth over which many channels can be created simultaneously storing different frequency modes. It is upper bounded by the inhomogeneous broadening of the transition for storage.

- **Time Bandwidth Product** (TBP) is a metric to characterize the multiplexing capacity of a quantum memory. It is the ratio of maximum storage time to the maximum duration of stored pulse [56, 58, 59]. This unit-less number gives an idea of the temporal multiplexing capacity and how many subsequent photons can be stored in the memory before the first is re-emitted. It also captures the balance between memory bandwidth and longer storage times if one is sacrificed for the other. Though TBP does not completely account for the multi-mode capacity of a quantum memory, higher TBP memories have more near term applications [60]. AFC quantum memories in general perform quite well for this particular metric with TBPs of better than 100, because their bandwidths are not dependent on available optical depth [46, 57]. In the frequency multiplexed case, TBP characterizes the temporal multiplexing capacity of a single spectral mode, but does not

describe the multiplexing capacity gained from some number of additional frequency modes beyond the bandwidth of an individual channel.

- **Ease of use** is an attempt to fold all intangibles into a single category. Of the many potential physical systems available for crafting quantum memories there are a number of other factors that differentiate them in terms of conducting experiments and building quantum repeater stations that may need to exist every 100km or less around the globe. Systems that require ultra high vacuum, ultra low temperatures, or ultra stable lasers may be worth the expenditure in a lab setting for initial demonstrations, but may be too difficult to produce on a wide scale across the globe. Concerning AFC using rare earth ions, the vacuum and temperature requirements are not too extreme, although most experiments require temperatures below 4k for long coherence. Perhaps the most stringent requirement is in terms of laser stability, which, for extremely long storage times using optical coherence may requires laser stability of below 1kHz for storage times of better than 100 us. It is also convenient to add operating wavelength to this category. There is a distinct benefit in the scaling of loss with transmission distance if the information carriers in a quantum network exist at frequencies between ~1300nm and ~1600nm (save the common OH- absorption peak) for the existing low loss telecommunication infrastructure. Quantum memories implemented using AFC in erbium doped materials or other quantum memory schemes have been demonstrated in this frequency range [33, 61–63].

  It may seem at times that frequency multiplexing and ease of use oppose one another since devices that can work simultaneously at multiple colors are distinctly more complex to operate. The prevailing idea is that thought the first 5 modes of these devices may be more difficult in the short term, the 100th or 1000th mode may be added to these devices much more easily in the far flung future.

- **Potential for Other Multiplexing** Multiplexing capacity cannot be stressed enough as one of the most important factors for creating good quantum memories. The number of modes available for simultaneous storage in a quantum memory should scale favorably with the optical depth of the memory platform [64, 65], and there should be zero cross talk between all simultaneously stored modes. In general, pairing memory and repeater architecture requires creativity.For AFC quantum memories, the multiplexing capacity is independent of optical depth making this scheme attractive for temporal and frequency multiplexing. For the frequency multiplexed case specifically, capacity is theoretically limited by the inhomogeneous broadening of the selected transition, which, in some cases, can reach many 10s of GHz [66]. In fact, no other quantum memory scheme is capable of providing such an extreme range of frequencies that are required for this a frequency multiplexed repeater design.

While many quantum memories, rare earth based, AFC, or otherwise, show promise in one or two of these figures of merit, single devices with strong characteristics across every category simply do not exist yet. From a theoretical perspective there is no clear front runner among rare earth ion species or hosts which possesses all of the necessary

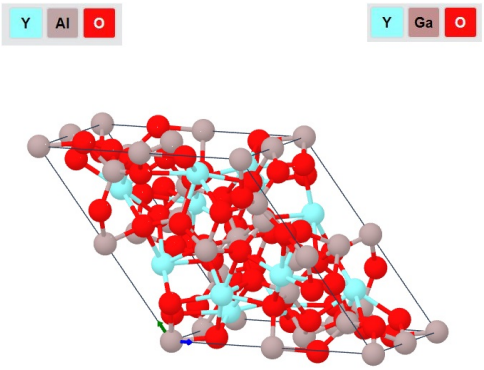

Figure 2.7: Simulated primitive cell of a garnet crystal structure. Three constituents make up the garnet structure, yttrium pictured in cyan, oxygen pictured in red, and a third species that may include Al,Ga,Fe, etc. shown in brown. The yttrium, or its substitutes, and the additional species bond only to surrounding oxygen in the structure. Image used with permission from the materials project [68, 69].

spectroscopic properties required to build a perfect quantum memory that would prove useful across many potential quantum repeater designs. Adding to this quandary, the technological limitations that plague many current AFC implementations are beginning to creep into the realm of ease of use problems. Nonetheless, the field has seen steady improvement across all figures of merit, so there is no fundamental reason to believe that these advances cannot continue. The strategy has become selecting a particular ion and host combination that seems it will apply well for a particular repeater design and going to work to improve all possible memory properties. In the next section I will discuss why we go to work on Tm ions in garnet host materials which may one day make one of the best potential options for frequency multiplexed quantum memories for quantum repeaters.

2.4. CHOOSING TM IONS IN GARNET MATERIALS

We have selected thulium ions in garnet host materials as the focus of our attempts to make good optical quantum memories. This decision can be justified with a few key properties of this ion and host combination. The garnet crystal structure is pictured in figure 2.7, where Tm^{3+} substitutes for a small portion of the yttrium atoms shown in cyan. The optical structure of Tm^{3+} is shown in figure 2.4 with the 795nm optical transition, easily addressed with commercially available diode lasers and often pursued for quantum information applications, highlighted in orange. Additional transitions, mentioned in chapter 5, are commonly pursued for applications in laser physics and optical amplification [67].

The key pair of metrics for thulium ions in garnet are the homogeneous and inhomogeneous linewidths of the 795nm optical transition in these materials. To benefit from the increase in light matter interaction, we work with large ensembles of ions in these hosts, which, feature broad inhomogeneous lines as pictured in figure 2.8. The homogeneous line-with of each individual ion in these hosts is small, in fact the smaller the

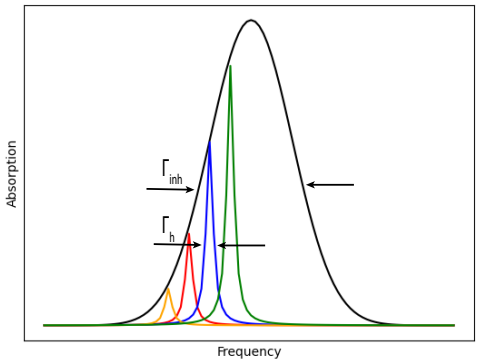

Figure 2.8: Inhomogeneous Γ_{inh} and homogeneous Γ_h linewidths of a rare earth ion ensemble. Though the absorption of each individual ion is a Lorentzian function, the summation of many of these homogeneous lines each shifted due to their slightly different electromagnetic environment sum to produce a larger Gaussian curve [70].

better for improved coherence and storage times. However, the inhomogeneous broadening in these materials is quite large, shaped by a sum of all overlapping lines for this transition belonging to all ions in the ensemble. Tm doped garnet materials show some of the longest coherence times available in rare earth ion doped materials as detailed in chapter 4. This combination of narrow homogeneous linewidth and broad inhomogeneous linewidth is fairly unique among the many potential ion host combinations and becomes immediately attractive for creating a quantum memory. Specifically, for the frequency multiplexed case, 10s of GHz inhomogeneous broadening coupled with a homogeneous linewidth for storage times above 100μs covers some of the most basic properties required for this repeater scheme.

With this initial indication of value, it becomes worth diving deeper into the details that lie underneath this initial choice of material. Since the nucleus of ^{169}Tm, the only isotope of this ion, has spin 1/2, crystal field levels have no hyperfine splitting at zero field leaving only a pair of degenerate spin levels. With an applied field, both ground and excited states of the 795nm transition split into a pair of spin states with a splitting on the order of 10s-100s of MHz/T, depending on the host. Details on the magnetic behavior of the relevant energy levels are available in chapter 6. By creating a small splitting between spin states, the small probability for spin crossing transitions to occur allows optical pumping in this material, the topic of detailed study in chapter 7. Thus, via optical pumping, high resolution spectral features can be created, in part due to the simple magnetic structure. Alongside the broad inhomogeneous line, the absence of crowded hyperfine structure removes bandwidth limits to each spectral channel which shows potential for quantum memory gains in storage bandwidth and TBP in these materials.

Growing a bit more specific, suitable magnetic structure and optical pumping dynamics are extremely important for crafting good spectral features and AFC quantum memories in general [71, 72]. For Tm there are no additional hyperfine levels which rules out memory schemes that involve coherent transfers to local spin levels. However, when using an AFC as a fixed delay memory for frequency multiplexing, the only needed levels

are for containing population to be excluded from the AFC structure. Thulium ions then remain a potential candidate, but only for fixed delay AFC memories.

These hyperfine features are due to the choice of Tm ions and arise regardless of host. Yet the host contributes the homogeneous and inhomogeneous linewidths that are essential for making this material attractive. However, garnets also introduce some complexity to their use. Firstly, the absorption coefficient in these materials is fairly weak[18]. Thus, enhancement of the absorption by other means such as optical cavities is generally required for making memories of high efficiency without a doping concentration that creates ion-ion interactions [47, 48]. Additionally, garnets have a cubic crystal structure in which there are 6 magnetically equivalent yet orientationally inequivalent yttrium sites to host dopant ions. This is confirmed for the case of Tm:YGG in chapter 6. Having so many sites means that it becomes difficult to isolate specific subsets of ions using specific magnetic or optical fields because many share close projections on each ion's transition dipole moments. Nonetheless, garnet being isotropic, there is no preferred axis for propagation, which leaves a number of options for casting the Tm ions into potentially useful subsets that are characterized by site orientation. Again, for the frequency multiplexed case, these potential drawbacks, if they can be overcome, represent a small price to pay for good coherence times and large potential working bandwidths.

As you can see above, each potential shortcoming for generic devices can luckily be cast as a feature for a specific application. With the ion, host, and spectrally multiplexed quantum repeaters in mind, it is time to go to work to improve the potential memories that can be made. The following chapters detail a number of investigations that demonstrate improved understanding of the material properties of Tm garnet materials and the improved capabilities of these devices as frequency multiplexed quantum memories.

BIBLIOGRAPHY

[1] D. Lago-Rivera, S. Grandi, J. V. Rakonjac, A. Seri, and H. de Riedmatten, "Telecom-heralded entanglement between multimode solid-state quantum memories", Nature **594**, 37–40 (2021).

[2] X. Liu, J. Hu, Z.-F. Li, X. Li, P.-Y. Li, P.-J. Liang, Z.-Q. Zhou, C.-F. Li, and G.-C. Guo, "Heralded entanglement distribution between two absorptive quantum memories", Nature **594**, 41–45 (2021).

[3] M. Grimau Puigibert, G. H. Aguilar, Q. Zhou, F. Marsili, M. D. Shaw, V. B. Verma, S. W. Nam, D. Oblak, and W. Tittel, "Heralded single photons based on spectral multiplexing and feed-forward control", Phys. Rev. Lett. **119**, 083601 (2017).

[4] A. Orieux, M. A. M. Versteegh, K. D. Jöns, and S. Ducci, "Semiconductor devices for entangled photon pair generation: a review", **80**, 076001 (2017).

[5] N. Sangouard, C. Simon, H. de Riedmatten, and N. Gisin, "Quantum repeaters based on atomic ensembles and linear optics", Rev. Mod. Phys. **83**, 33–80 (2011).

[6] R. Valivarthi et al., "Efficient bell state analyzer for time-bin qubits with fast-recovery wsi superconducting single photon detectors", Opt. Express **22**, 24497–24506 (2014).

[7] N. Lütkenhaus, J. Calsamiglia, and K.-A. Suominen, "Bell measurements for teleportation", Phys. Rev. A **59**, 3295–3300 (1999).

[8] F. Ewert and P. van Loock, "3/4-efficient bell measurement with passive linear optics and unentangled ancillae", Phys. Rev. Lett. **113**, 140403 (2014).

[9] P. Vernaz-Gris, K. Huang, M. Cao, A. S. Sheremet, and J. Laurat, "Highly-efficient quantum memory for polarization qubits in a spatially-multiplexed cold atomic ensemble", Nature Communications **9**, 363 (2018).

[10] Y.-F. Pu, N. Jiang, W. Chang, H.-X. Yang, C. Li, and L.-M. Duan, "Experimental realization of a multiplexed quantum memory with 225 individually accessible memory cells", Nature Communications **8**, 15359 (2017).

[11] Z.-Q. Zhou, Y.-L. Hua, X. Liu, G. Chen, J.-S. Xu, Y.-J. Han, C.-F. Li, and G.-C. Guo, "Quantum storage of three-dimensional orbital-angular-momentum entanglement in a crystal", Phys. Rev. Lett. **115**, 070502 (2015).

[12] C. Laplane, P. Jobez, J. Etesse, N. Timoney, N. Gisin, and M. Afzelius, "Multiplexed on-demand storage of polarization qubits in a crystal", **18**, 013006 (2015).

[13] C. Simon et al., "Quantum memories", The European Physical Journal D **58**, 1–22 (2010).

[14] N. Sinclair et al., "Spectral multiplexing for scalable quantum photonics using an atomic frequency comb quantum memory and feed-forward control", Phys. Rev. Lett. **113**, 053603 (2014).

[15] S. Guha, H. Krovi, C. A. Fuchs, Z. Dutton, J. A. Slater, C. Simon, and W. Tittel, "Rate-loss analysis of an efficient quantum repeater architecture", Phys. Rev. A **92**, 022357 (2015).

[16] A. Seri, D. Lago-Rivera, A. Lenhard, G. Corrielli, R. Osellame, M. Mazzera, and H. de Riedmatten, "Quantum storage of frequency-multiplexed heralded single photons", Phys. Rev. Lett. **123**, 080502 (2019).

[17] O. Pietx I Casas, *A spectrally-multiplexed bell-state measurements*, 2021.

[18] G. Liu and B. Jacquier, *Spectroscopic properties of rare earths in optical materials*, Vol. 83 (Springer Science & Business Media, 2006).

[19] C. Thiel, T. Böttger, and R. Cone, "Rare-earth-doped materials for applications in quantum information storage and signal processing", Journal of Luminescence **131**, Selected papers from DPC'10, 353–361 (2011).

[20] R. MACFARLANE and R. SHELBY, "Chapter 3 - coherent transient and holeburning spectroscopy of rare earth ions in solids", in *Spectroscopy of solids containing rare earth ions*, Vol. 21, edited by A. KAPLYANSKII and R. MACFARLANE, Modern Problems in Condensed Matter Sciences (Elsevier, 1987), pp. 51–184.

[21] V. Rivera, F. Ferri, and E. M. Jr., "Localized surface plasmon resonances: noble metal nanoparticle interaction with rare-earth ions", in *Plasmonics*, edited by K. Y. Kim (InTechOpen, Rijeka, 2012) Chap. 11.

[22] B. Merkel, A. Ulanowski, and A. Reiserer, "Coherent and purcell-enhanced emission from erbium dopants in a cryogenic high-Q resonator", Phys. Rev. X **10**, 041025 (2020).

[23] S. Chen, M. Raha, C. M. Phenicie, S. Ourari, and J. D. Thompson, "Parallel single-shot measurement and coherent control of solid-state spins below the diffraction limit", Science **370**, 592–595 (2020).

[24] J. G. Bartholomew, J. Rochman, T. Xie, J. M. Kindem, A. Ruskuc, I. Craiciu, M. Lei, and A. Faraon, "On-chip coherent microwave-to-optical transduction mediated by ytterbium in yvo4", Nature Communications **11**, 3266 (2020).

[25] E. Fraval, M. J. Sellars, and J. J. Longdell, "Method of extending hyperfine coherence times in $Pr^{3+}:Y_2SiO_5$", Phys. Rev. Lett. **92**, 077601 (2004).

[26] M. Zhong, M. P. Hedges, R. L. Ahlefeldt, J. G. Bartholomew, S. E. Beavan, S. M. Wittig, J. J. Longdell, and M. J. Sellars, "Optically addressable nuclear spins in a solid with a six-hour coherence time", Nature **517**, 177–180 (2015).

[27] O. Guillot-Noël, P. Goldner, E. Antic-Fidancev, and J. L. Le Gouët, "Analysis of magnetic interactions in rare-earth-doped crystals for quantum manipulation", Phys. Rev. B **71**, 174409 (2005).

[28] Y. Ma, Y.-Z. Ma, Z.-Q. Zhou, C.-F. Li, and G.-C. Guo, "One-hour coherent optical storage in an atomic frequency comb memory", Nature Communications **12**, 2381 (2021).

[29] C. Sun and D. Xue, "Pulling growth technique towards rare earth single crystals", Science China Technological Sciences **61**, 1295–1300 (2018).

[30] C. Brandle and A. Valentino, "Czochralski growth of rare earth gallium garnets", Journal of Crystal Growth **12**, 3–8 (1972).

[31] C. Venet, B. Car, L. Veissier, F. Ramaz, and A. Louchet-Chauvet, "Deep and persistent spectral holes in thulium-doped yttrium orthosilicate for imaging applications", Phys. Rev. B **99**, 115102 (2019).

[32] E. Fraval, "Minimising the decoherence of rare earth ion solid state spin qubits", PhD thesis (Research School of Physical Sciences, Engineering, and The Australian National University, 2005).

[33] M. F. Askarani, M. G. Puigibert, T. Lutz, V. B. Verma, M. D. Shaw, S. W. Nam, N. Sinclair, D. Oblak, and W. Tittel, "Storage and reemission of heralded telecommunication-wavelength photons using a crystal waveguide", Phys. Rev. Applied **11**, 054056 (2019).

[34] R. L. Ahlefeldt, M. F. Pascual-Winter, A. Louchet-Chauvet, T. Chanelière, and J.-L. Le Gouët, "Optical measurement of heteronuclear cross-relaxation interactions in tm:yag", Phys. Rev. B **92**, 094305 (2015).

[35] A. Ruskuc, C.-J. Wu, J. Rochman, J. Choi, and A. Faraon, *Nuclear spin-wave quantum register for a solid state qubit*, 2021.

[36] M. Afzelius, C. Simon, H. de Riedmatten, and N. Gisin, "Multimode quantum memory based on atomic frequency combs", Phys. Rev. A **79**, 052329 (2009).

[37] P. Zarkeshian et al., "Entanglement between more than two hundred macroscopic atomic ensembles in a solid", Nature Communications **8**, 906 (2017).

[38] M. Businger, A. Tiranov, K. T. Kaczmarek, S. Welinski, Z. Zhang, A. Ferrier, P. Goldner, and M. Afzelius, "Optical spin-wave storage in a solid-state hybridized electron-nuclear spin ensemble", Phys. Rev. Lett. **124**, 053606 (2020).

[39] E. Saglamyurek et al., "Broadband waveguide quantum memory for entangled photons", Nature **469**, 512–515 (2011).

[40] M. Sabooni, Q. Li, S. Kröll, and L. Rippe, "Efficient quantum memory using a weakly absorbing sample", Phys. Rev. Lett. **110**, 133604 (2013).

[41] A. Ortu, A. Holzäpfel, J. Etesse, and M. Afzelius, *Storage of photonic time-bin qubits for up to 20 ms in a rare-earth doped crystal*, 2021.

[42] M. F. Askarani et al., "Long-lived solid-state optical memory for high-rate quantum repeaters", Phys. Rev. Lett. **127**, 220502 (2021).

[43] Y. Wang, J. Li, S. Zhang, K. Su, Y. Zhou, K. Liao, S. Du, H. Yan, and S.-L. Zhu, "Efficient quantum memory for single-photon polarization qubits", Nature Photonics **13**, 346–351 (2019).

[44] M. Cao, F. Hoffet, S. Qiu, A. S. Sheremet, and J. Laurat, "Efficient reversible entanglement transfer between light and quantum memories", Optica **7**, 1440–1444 (2020).

[45] Y.-W. Cho et al., "Highly efficient optical quantum memory with long coherence time in cold atoms", Optica **3**, 100–107 (2016).

[46] P. Jobez, I. Usmani, N. Timoney, C. Laplane, N. Gisin, and M. Afzelius, "Cavity-enhanced storage in an optical spin-wave memory", **16**, 083005 (2014).

[47] M. Afzelius and C. Simon, "Impedance-matched cavity quantum memory", Phys. Rev. A **82**, 022310 (2010).

[48]S. A. Moiseev, S. N. Andrianov, and F. F. Gubaidullin, "Efficient multimode quantum memory based on photon echo in an optimal qed cavity", Phys. Rev. A **82**, 022311 (2010).

[49]S. Massar and S. Popescu, "Optimal extraction of information from finite quantum ensembles", Phys. Rev. Lett. **74**, 1259–1263 (1995).

[50]V. Bu žek and M. Hillery, "Quantum copying: beyond the no-cloning theorem", Phys. Rev. A **54**, 1844–1852 (1996).

[51]H. P. Specht, C. Nölleke, A. Reiserer, M. Uphoff, E. Figueroa, S. Ritter, and G. Rempe, "A single-atom quantum memory", Nature **473**, 190 EP - (2011).

[52]M. Gündo ğan, P. M. Ledingham, A. Almasi, M. Cristiani, and H. de Riedmatten, "Quantum storage of a photonic polarization qubit in a solid", Phys. Rev. Lett. **108**, 190504 (2012).

[53]W. J. Munro, K. Azuma, K. Tamaki, and K. Nemoto, "Inside quantum repeaters", IEEE Journal of Selected Topics in Quantum Electronics **21**, 78–90 (2015).

[54]C. Liu et al., "Reliable coherent optical memory based on a laser-written waveguide", Optica **7**, 192–197 (2020).

[55]M. U. Staudt et al., "Fidelity of an optical memory based on stimulated photon echoes", Phys. Rev. Lett. **98**, 113601 (2007).

[56]W. Tittel, M. Afzelius, T. Chaneliére, R. Cone, S. Kröll, S. Moiseev, and M. Sellars, "Photon-echo quantum memory in solid state systems", Laser & Photonics Reviews **4**, 244–267 (2010).

[57]M. l. G. Puigibert et al., "Entanglement and nonlocality between disparate solid-state quantum memories mediated by photons", Phys. Rev. Research **2**, 013039 (2020).

[58]J. Nunn, N. Langford, W. S Kolthammer, T. Champion, M. R Sprague, P. Michelberger, X.-M. Jin, D. England, and I. Walmsley, "Enhancing multiphoton rates with quantum memories", Physical review letters **110**, 133601 (2013).

[59]M. R. Sprague et al., "Broadband single-photon-level memory in a hollow-core photonic crystal fibre", Nature Photonics **8**, 287 EP - (2014).

[60]K. Heshami, D. G. England, P. C. Humphreys, P. J. Bustard, V. M. Acosta, J. Nunn, and B. J. Sussman, "Quantum memories: emerging applications and recent advances", Journal of Modern Optics **63**, PMID: 27695198, 2005–2028 (2016).

[61]A. Wallucks, I. Marinković, B. Hensen, R. Stockill, and S. Gröblacher, "A quantum memory at telecom wavelengths", Nature Physics **16**, 772–777 (2020).

[62]E. Saglamyurek, J. Jin, V. B. Verma, M. D. Shaw, F. Marsili, S. W. Nam, D. Oblak, and W. Tittel, "Quantum storage of entangled telecom-wavelength photons in an erbium-doped optical fibre", Nature Photonics **9**, 83–87 (2015).

[63]I. Craiciu, M. Lei, J. Rochman, J. G. Bartholomew, and A. Faraon, "Multifunctional on-chip storage at telecommunication wavelength for quantum networks", Optica **8**, 114–121 (2021).

[64] N. Sangouard, C. Simon, M. Afzelius, and N. Gisin, "Analysis of a quantum memory for photons based on controlled reversible inhomogeneous broadening", Phys. Rev. A **75**, 032327 (2007).

[65] J. Nunn, K. Reim, K. C. Lee, V. O. Lorenz, B. J. Sussman, I. A. Walmsley, and D. Jaksch, "Multimode memories in atomic ensembles", Phys. Rev. Lett. **101**, 260502 (2008).

[66] C. W. Thiel, N. Sinclair, W. Tittel, and R. L. Cone, "Optical decoherence studies of Tm^{3+} : $Y_3Ga_5O_{12}$", Phys. Rev. B **90**, 214301 (2014).

[67] F. Stutzki, C. Gaida, M. Gebhardt, F. Jansen, C. Jauregui, J. Limpert, and A. Tünnermann, "Tm-based fiber-laser system with more than 200mw peak power", Opt. Lett. **40**, 9–12 (2015).

[68] K. Persson, *Materials data on y3al5o12 (sg:230) by materials project*, An optional note, July 2014.

[69] K. Persson, *Materials data on y3ga5o12 (sg:230) by materials project*, An optional note, July 2014.

[70] L. Allen and J. Eberly, *Optical resonance and two-level atoms*, Dover Books on Physics (Dover Publications, 2012).

[71] M. Bonarota, J. Ruggiero, J. .-. L. Gouët, and T. Chanelière, "Efficiency optimization for atomic frequency comb storage", Phys. Rev. A **81**, 033803 (2010).

[72] P. Jobez, N. Timoney, C. Laplane, J. Etesse, A. Ferrier, P. Goldner, N. Gisin, and M. Afzelius, "Towards highly multimode optical quantum memory for quantum repeaters", Phys. Rev. A **93**, 032327 (2016).

3

Improved Light-Matter Interaction for Storage of Quantum States of Light in a Thulium-Doped Crystal Cavity

Jacob H. Davidson, Pascal Lefebvre, Jun Zhang, Daniel Oblak, and Wolfgang Tittel

Cavities are made by sugar.
So if you need to dig a hole, then lay down some candy bars!

Mitch Hedberg

We design and implement an atomic frequency comb quantum memory for 793 nm wavelength photons using a monolithic cavity based on a thulium-doped $Y_3Al_5O_{12}$ (Tm:YAG) crystal. Approximate impedance matching results in the absorption of 90% of input photons and a memory efficiency of (27.5± 2.7)% over a 500 MHz bandwidth. The cavity enhancement leads to a significant improvement over the previous efficiency in Tm-doped crystals using a quantum memory protocol. In turn, this allows us for the first time to store and recall quantum states of light in such a memory. Our results demonstrate progress toward efficient and faithful storage of single-photon qubits with large time-bandwidth product and multi-mode capacity for quantum networking.

Parts of this chapter, marked with a *, have been published in Physical Review A **101**, 042333 (2020) [1].

3.1. PREAMBLE

The results of this paper demonstrate the effectiveness of impedance matched cavities for improving AFC quantum memory efficiency. These cavities will be required to prevent excessive loss from poor absorption of rare earth ion doped crystals which need low doping concentrations to prevent dephasing due to ion-ion interaction. The entanglement distribution rate of all networking demonstrations depend on this figure of merit. This experiment shows that these memory improvements will persist even when single photons are the signal being stored.

3.2. INTRODUCTION*

QUANTUM memories (QM) that can map fast moving quantum states of light reversibly onto matter are an invaluable component of future quantum networks[2]. These light-matter interfaces increase the efficiency of complex quantum networking schemes, and allow network tasks to be accomplished over large distances, and via error correction and local processing [3]. For instance, quantum memories for light play a crucial role in the efficient distribution of entanglement over large distances, thereby securing classical communication by means of quantum key distribution and allowing the lossless distribution of qubits through quantum teleportation. Common to all these applications is the need for efficient quantum memories that can store many qubits encoded into different modes of light, which is often referred-to as the multiplexing capacity or time-bandwidth product [4].

For quantum networking it has been shown that the rate of entanglement generation, or complex multi-photon state generation, scales with the product of memory efficiency and time-bandwidth product [5, 6]. The intuition behind this follows from that of classical communications: higher efficiency devices allow more equipment to be connected over greater distances before loss takes a toll. Similarly, communication rates scale with the number of temporal and spectral channels, e.g. a memory's multiplexing capacity or time-bandwidth product [7–9]. Finally, quantum memories for light should feature sufficiently large bandwidths to interface with a diverse range of single photon sources, including spontaneous parametric down-conversion (SPDC), quantum dots, and single molecule emitters [10–12].

Starting with the description of suitable quantum storage protocols around 15 years ago [13, 14], cryogenically-cooled rare-earth crystals have rapidly demonstrated their potential as suitable storage materials. In particular, in conjunction with the so-called atomic frequency comb (AFC) protocol [15] they have allowed storing non-classical states of light such as single and entangled photons [16–20]. In order to increase efficiencies to values close to 100 %, there has been a push towards cavity-enhanced light-matter interaction [21]. A lot of progress has been reported towards this end [22–24], but cavity-enhanced storage of non-classical light remains to be demonstrated, in part due to the limited available memory bandwidth. Here we demonstrate a 500 MHz-broad quantum memory with efficiency up to 27.5%, as well as high-fidelity storage of heralded single photons over more than 1.5 GHz bandwidth using an impedance-matched cavity. Our findings further support the potential of rare-earth crystals to meet the stringent demands of future quantum networks for memories that allow quantum state storage.

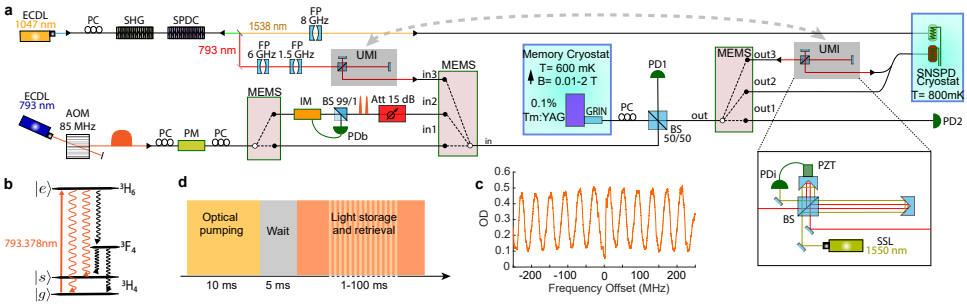

Figure 3.1: **(a)** Schematic of experimental setup; FP Fabry Perot Filter Cavity; ECDL External Cavity Diode Laser; SSL Solid State Laser; SHG Second Harmonic Generation; SPDC Spontaneous Parametric Downconversion; FP Fabry-Perot cavity filter; BS Beam-Splitter; PC Polarization Controller; GRIN Gradient Index Lens; UMI Unbalanced Michelson Interferometer; PZT Piezo-electric actuator; Att Optical Attenuator; AOM Acousto-Optic Modulator; PD Photo Diode; MEMS Micro Electro-Mechanical Switches; SNSPD Superconducting Nanowire Single Photon Detectors; IM Intensity Modulator; PM Phase Modulator. Light from 3 paths was directed to an input beam splitter for AFC creation and photon storage. After re-emission from the memory, the light was switched between different analyzers. **(b)** Level structure of Tm:YAG. **(c)**Example 500 MHz AFC scan of a weak read pulse across the comb. **(d)** Experimental duty cycle, spectral hole burning time, period of spontaneous emission, and a period for memory use.

3.3. EXPERIMENTAL SETUP*

The memory cavity is made of a $l = 4$ mm long 0.1% Tm: $Y_3Al_5O_{12}$ (Tm:YAG) crystal and placed in a cryostat operating at a temperature of 600 mK. The end facets of the crystal are reflection coated, with reflectivities R_2 =99% on the rear and $R_1 = 40\%$ on the front side. The reflectivity value for the front facet is chosen to allow for impedance matching at the 793 nm Tm:YAG absorption wavelength by meeting the condition $R_1 = R_2 e^{(-2\alpha l)}$ with α the average absorption coefficient across the cavity resonance bandwidth [21]. These coatings create a planar optical cavity with a free spectral range of 20 GHz, and a finesse of 7.

The Tm:YAG crystal was cut and mounted such that a magnetic field (aligned along the [001] crystal axis) splits the Zeeman degeneracy for 4 of the 6 crystallographic sites equally to create a lambda system for optical pumping [25]. Optical access was provided by ferrule-tipped (single mode) fibers and collimation lensing through the planar crystal cavity, and alignment to the fundamental cavity mode was achieved through nano-positioning stages that allow angular steering of the ferrules. All input signals were routed into the memory by a set of MEMS switches and a 50:50 fiber beam-splitter, which also allowed collection of the reflected signals (see Fig. 4.2(a)).

A single AFC memory consists of a spectrally periodic distribution of atomic absorption peaks with spacing δ (see [15, 18, 26] for more information). Overlapping an optical signal field with this shaped absorption feature causes the AFC to absorb the input pulse of light. The rare-earth dopants within the crystal are put into an entangled superposition state, primed for re-emission after a pre-set interval $\tau = 1/\delta$. We addressed the rare earth ion-doped crystal sample using three paths, as seen in Fig.4.2(a) – one for creation of the AFC, and two more for delivering various signals for storage. We sculpt this spectral comb feature through optical pumping on the Tm $^3H_6 \rightarrow {}^3H_4$ tran-

sition, shown in Fig.4.2(b), to drive population with transition frequencies matching the comb troughs into magnetically separated Zeeman level, $|s\rangle$. When the Zeeman level splitting is matched to the desired comb tooth spacing, a spectral grating with finesse (the ratio between peak spacing δ and peak width) $F_{AFC} \approx 2$ is prepared without altering the average optical depth. The pumping process, pictured in Fig.4.2(d), allowed the creation of memory features between 100 MHz-10 GHz bandwidth with tooth spacing from 4-100 MHz. These memories allow storage of 100 ps-10 ns long pulses for times between 10 and 250 ns, limited by pump laser linewidth. An example of one such comb, created in an uncoated region of the crystal, is pictured in Fig.4.2(c).

The impedance matching scheme relies on interference between electric field leaking through the front cavity facet after each cavity round trip, and the incoming field initially reflected from the front facet. At the impedance matched condition, these fields create perfectly destructive interference resulting in perfect intake of light by the lossy cavity mode. In our case, the engineered loss (in the form of an AFC) guarantees heightened interaction between light and rare-earth ions.

3.4. RESULTS*

In the following we describe initial characterizations of the memory. First, we examined how cavity resonances interact with the Tm:YAG absorption profile. Using an intensity modulator (IM) to carve Gaussian pulses of 4 ns duration at 1000 Hz repetition rate, we slowly swept the laser frequency across the inhomogeneous Tm absorption line centered at 793 nm. Shown in Fig.3.2(a), the reflected part of the input pulse was detected and normalized to the input pulse intensity. No signal was detected transmitting through the cavity. On resonance with the cavity mode and ~ 4 GHz from thulium line center, more than 90% of the input energy was absorbed within the rare-earth cavity system.

Next, we created a 500 MHz-wide AFC and moved its center frequency in 500 MHz increments from the Tm:YAG absorption peak past the cavity resonance. For each detuning, we measured the storage efficiency using laser pulses containing many photons. As expected, the optimum central AFC frequency matched the minimum of the cavity's reflection spectrum. As seen in Fig. 3.2(b), the absorption and re-emission of light then becomes more likely than the reflection of the signal light from the cavity, peaking at a system efficiency of 12± 1%. Taking into account 50% loss of the input-output splitter as well as 6% coupling and lensing loss, we find a memory efficiency of 27.5±2.7%. It decreases to 7% for a 1.6 GHz wide AFC due to the limited bandwidth of the impedance-matched cavity (see Supplemental Material for details). These values, which are insensitive to the type of input signal (strong or weak laser pulses, or heralded single photons), correspond to a 20 to 30-fold increase of the single-pass efficiency in the same crystal (no cavity), which we estimate to be below 1%. Note as well that, due to the combination of our sample's small single-pass absorption and the broad bandwidth of our spectral features, we measured no evidence of strong dispersion, which has previously limited bandwidths of similar cavity-based memories [22, 23, 27].

We used several light sources to test the memory. First, to create time-bin qubits encoded into temporal modes of attenuated laser pulses, we employed an AOM combined with an IM to tailor a continuous-wave laser beam at 793 nm wavelength. Early and late temporal modes were of 800 ps lengths and separated by 1.4 ns, with spectral

and phase control achieved via laser diode grating adjustment and a serrodyne-driven phase modulator. Second, we prepared quantum-correlated pairs of photons at 1538 and 793 nm wavelength by means of spontaneous parametric down-conversion (SPDC) in a periodically-poled lithium niobate waveguide. After filtering, their spectra were narrowed to 8 GHz and 1.5 GHz, respectively. Third, passing the 793 nm photons before storage through an unbalanced Michelson interferometer, we could furthermore generate heralded time-bin qubits with the same mode separation. All single-photon-level signals were detected using low jitter WSi superconducting nanowire single-photon detects (SNSPDs) [28] followed by suitable coincidence electronics. In addition, to analyze photons in qubit states, we employed an actively phase-locked Michelson interferometer with 42 cm path-length difference.

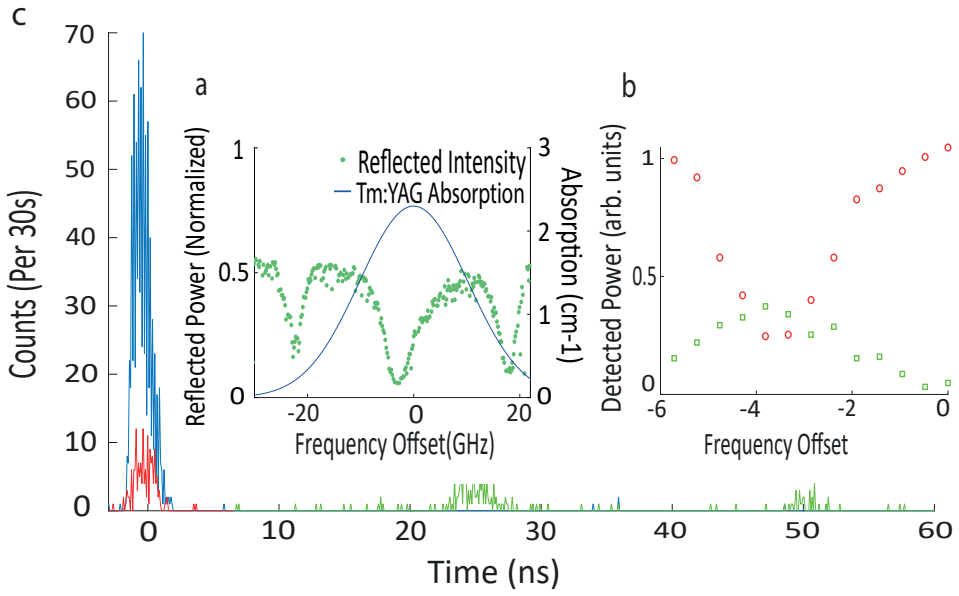

Figure 3.2: **(a)** The line (blue) shows the absorption of the Tm:YAG crystal without cavity [29], while the points (green) show the normalized reflected power obtained by sweeping 4 ns-long pulses of light in frequency across the cavity features. Close-to-perfect impedance matching is obtained at a detuning of -4 GHz. **(b)** Detected intensity of strong 2 ns-long light pulses after reflection (red circles), and re-emission after 50 ns storage from the cavity (green squares). The maximum re-emission is visible at (approximate) impedance matching. All AFCs were of 500 MHz width. **(c)** Detection histograms for 25 ns storage of weak coherent pulses. The upper(blue) peak occuring at 0ns offset is the memory input pulse; the lower(red) peak occuring at 0ns is the portion of the input pulse that is reflected from the cavity (not stored), the (green) peaks at 25 and 50 ns show recalled pulses after a multiples of the storage time.

To study how well our memory stores non-classical light, we first used photon pairs and measured cross correlations between heralding 1538 nm photons and 793 nm photons. At maximum pump laser power with no memory in place, we found a cross-correlation coefficient of $g^{(2)} = 61.8 \pm 3.8$. For values of $g^{(2)} > 2$, the correlations violate the Cauchy-Schwartz inequality, implying that they are non-classical in nature [30]. Adding the memory for the 793 nm photons, we measured $g^{(2)} = 9.1 \pm 1.2$ after 25 ns storage, and we

found Cauchy Schwartz violations after as much as 100 ns (see Fig. 3.3). This shows the preservation of quantum correlations during storage in the cavity memory, and hence establishes that the cavity-enhanced memory as a quantum memory for light.

Next, we created and stored various time-bin qubits encoded into attenuated laser pulses with a mean photon number of $\mu = 0.7$. For these measurements we set the storage time to 25 ns. For Z basis states, $|Z+\rangle \equiv |e\rangle$ and $|Z-\rangle \equiv |l\rangle$, we found a mean fidelity of $\mathscr{F}_z = 97.6 \pm 0.02\%$. Furthermore, characterization of $|X_\pm\rangle \equiv \frac{|e\rangle \pm |l\rangle}{\sqrt{2}}$ and $|Y_\pm\rangle \equiv \frac{|e\rangle \pm i|l\rangle}{\sqrt{2}}$ yielded $\mathscr{F}_{x,y} = 93.7 \pm 0.1\%$, resulting in a memory fidelity averaged over all six states of $\mathscr{F} = \frac{1}{3}\mathscr{F}_z + \frac{2}{3}\mathscr{F}_{x,y} = 95 \pm 0.1\%$ (see Fig. 3.4, the Supplemental Material, and [11] for more details). Taking into account the recall efficiency of 7% and the mean photon number of $\mu = 0.7$, all fidelities significantly exceed the upper bound of $\mathscr{F}(\mu, \eta) = 80.3\%$, established conservatively for classical memories under the assumption of intercept-resend attacks [31–33], as well as that imposed by the optimal universal quantum cloning machine [34].

Finally, we repeated these measurements after replacing the source of attenuated laser pulses by heralded single photons. But instead of using interferometers to analyze the qubits after storage in the X- and Y-basis, we configured the memory for double-comb storage with storage-time separation matching the qubit time-bin separation. This method allows for a convenient analysis of time-bin qubit states in the superposition bases [35]. The series of measurements resulted in a heralded single-photon qubit fidelity of $\mathscr{F} = 85 \pm 0.02\%$(See Supplemental Material), again exceeding the thresholds imposed by classical storage and quantum cloning. It also allowed us to establish the density matrices of recalled qubits for various inputs by means of quantum state tomography (see Fig. 3.4(a)), and in turn to perform quantum process tomography [36, 37]. The resulting storage process matrix, χ, depicted in Fig. 3.4(b), complete describes the mapping between arbitrary input and output qubit states[32]. As expected, the dominant term describes the identity operation, but some small imperfections with magnitudes ≤ 0.1 are also visible.

Another way of presenting these imperfections is to look at the ensemble of output states averaged over all possible input states. This results in a deformed Bloch sphere, as shown in Fig. 3.4(c). But note that this deformation as well as the unexpected elements in the process matrix in Fig. 3.4(b) provide the upper bound to imperfections in the storage process. Indeed, they are mostly caused by imperfect state preparation and measurement, rather than by an imperfect memory. For example, non-ideal PM drive-pulse duration and timing cause small frequency shifts between temporal input modes, making them distinguishable and therefore reducing the quality of the interference required for analysis. Furthermore, imbalances of the beamsplitters used to split and couple temporal modes in our analysis interferometer also lower the measured fidelities.

3.5. CONCLUSION*

To summarize, we have demonstrated that solid-state quantum memory based on ensembles of rare-earth ions and cavity-enhanced light-matter interaction in a monolithic and fibre-coupled cavity allows storing quantum states of light. Our memory operates in the domain of pre-set storage times and allows feed-forward based mode mapping using external frequency shifters [7]. It is capable of storing broadband quantum light with a

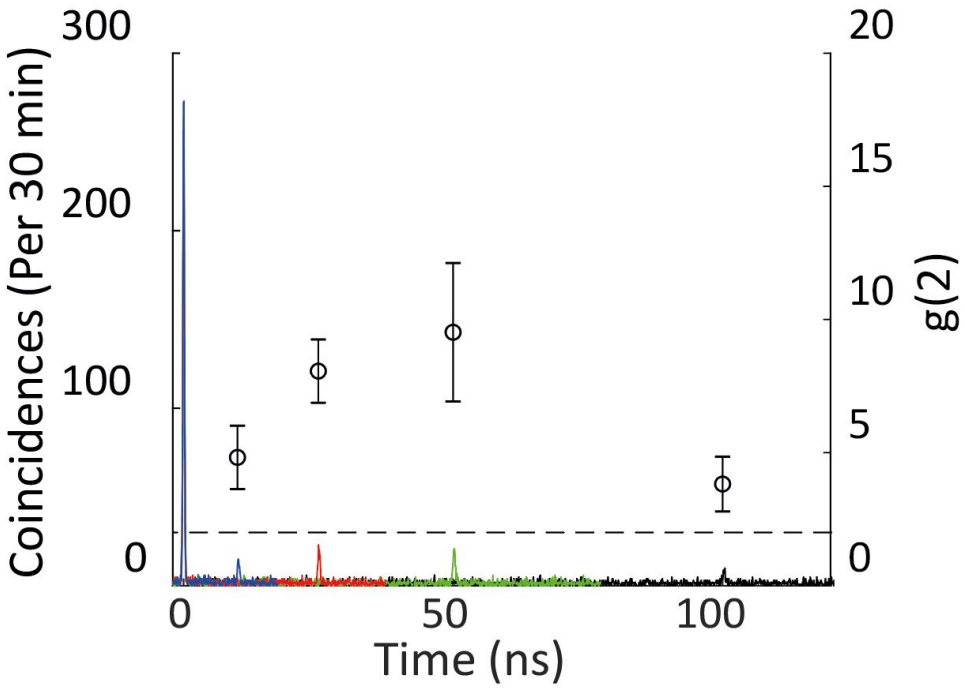

Figure 3.3: Time-resolved coincidence detections of a 1538 nm heralding photon and a 793 nm photon stored in the cavity memory for various, different storage times. The peaks visible at each of the set storage times(10,25,50, 100 ns) verify that the non-classical correlations created by SPDC persist after storage. The righthand axis depicts the $g^{(2)}$ value for each peak with error bars multiple standard deviations above the classical limit (dashed line).

fidelity of at least 95%, an efficiency η of up to 27.5%, and a time-bandwidth product TB of up to 100 ns *1.5 GHz=150, where 100 ns is the longest time after which we observed a violation of the Cauchy-Schwartz inequality. We note that the factor $\eta * TB = 1050$ (with $\eta = 7\%$), which is comparable to that obtained in previous demonstrations of rare-earth-ensemble-based storage of attenuated laser pulses [38].

To further improve key properties, several modifications are required. First, to reach an efficiency close to 100%, the finesse of the AFC has to be increased beyond its current value of two. As this is only possible if the total AFC width is smaller than the ground-state splitting of the rare-earth ion, in this case 200 MHz/T, this limits the available bandwidth per spectral channel, implying the need for suitably adapted sources of quantum light. However, the time-bandwidth product can remain high as many spectral channels can be created in parallel [7]. Furthermore, fibre coupling loss must be reduced through better mode matching. Second, to increase the storage time to a few hundred μsec, enough for an elementary link in a quantum repeater architecture of around 100 km [7], materials with improved coherence have to be employed. Possibilities include Tm:$Y_3Ga_5O_{12}$ for which optical coherence times of 490μsec have been reported [39], or materials featuring narrow ground-state transitions [25].

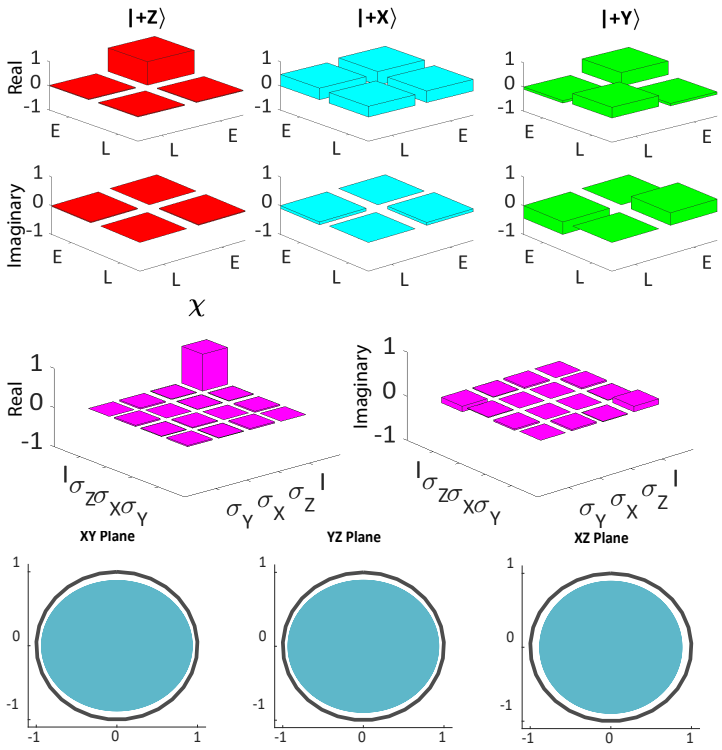

Figure 3.4: **a.** Density matrices of three non-orthogonal qubit states after re-emission form the memory. **b.** Quantum process matrix χ. **c.** Cross sections through the Bloch sphere depicting the average over all possible output states. Black circular lines denote the output expected from a perfect memory, and the filled ovals (blue) depict qubits after the non-ideal storage process [32].

3.6. SUPPLEMENTAL MATERIAL*

3.6.1. EFFICIENCY CALCULATION

The Efficiency of a Quantum Memory is a key figure of merit that helps to determine the merit of a particular device. This AFC quantum memory produced a peak efficiency of 27.5%. This number is measured as an average between a number of trials to account for fluctuations in the setup. Varying laser power and polarization fluctuations between light used to create the AFC structure and light used to create qubits causes the variation between points.

3.6.2. MEMORY BANDWIDTH

The bandwidth of a Quantum Memory is a key figure of merit that helps to determine the merit of a particular device. For AFC quantum memories the bandwidth is determined by the range of frequencies over which the periodic spectral feature is created. However, for a cavity implementation of an AFC quantum memory, the cavity resonance has a fixed bandwidth set by crystal length and the selected reflectivities. The results in a trade

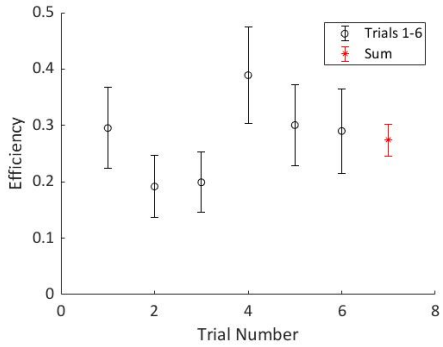

Figure 3.5: Memory Efficiency over a number of trials with the optimal polarization setting. Each trial is the summed results for memory efficiency from 30 seconds of data collection for attenuated classical light at the single photon level. The final point shown in red is the sum of all trials which yields the efficiency listed in the main text.

off with the AFC efficiency, as the memory bandwidth exceeds the impedance matched range of the cavity resonance.

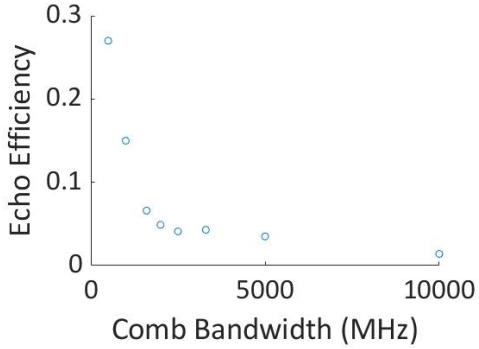

Figure 3.6: Scaling of Maximum AFC memory efficiency with bandwidth of the created comb feature. All combs were created centered on the cavity resonance -4 GHz from the absorption line center. Each point is the measured memory efficiency after 25ns of storage using attenuated light pulses with bandwidth matching the comb feature.

3.6.3. QUBIT STORAGE INTERFERENCE CURVES

Storing time bin qubits in the main text we measured the fidelity of storage. For the X basis states of $|+\rangle$ and $|-\rangle$, this is related to an interference visibility after sending the qubit pulses through a unbalanced Michelson interferometer. The visibility of interference curves produced by a number of different interferometer phases translates directly to the memory fidelity. In ths following figures 3.7 and 3.8 we show the measured interference curves for a pair of differently crafted qubits.

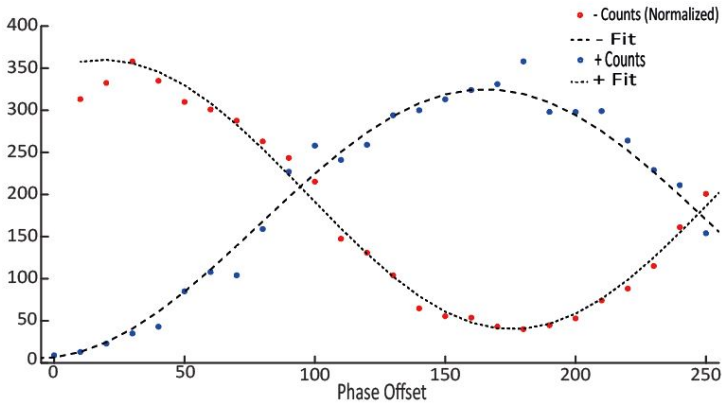

Figure 3.7: Interference curves generated by $|+\rangle$ and $|-\rangle$ time bin qubits created from weak coherent pulses after storage in the memory.

ACKNOWLEDGEMENTS*

The authors would like to thank Neil Sinclair for discussions, and Jay Mckisaac and Nik Hamilton for design assistance and manufacturing of cryogenic components. We acknowledge funding through Alberta Innovates Technology Futures (AITF), the National Science and Engineering Research Council of Canada (NSERC),the Netherlands Organization for Scientific Research (NWO), and the European Union's Horizon 2020 research and innovation program under grant agreement No 820445 and project name Quantum Internet Alliance. Furthermore, WT acknowledges funding as a Senior Fellow of the Canadian Institute for Advanced Research (CIFAR).

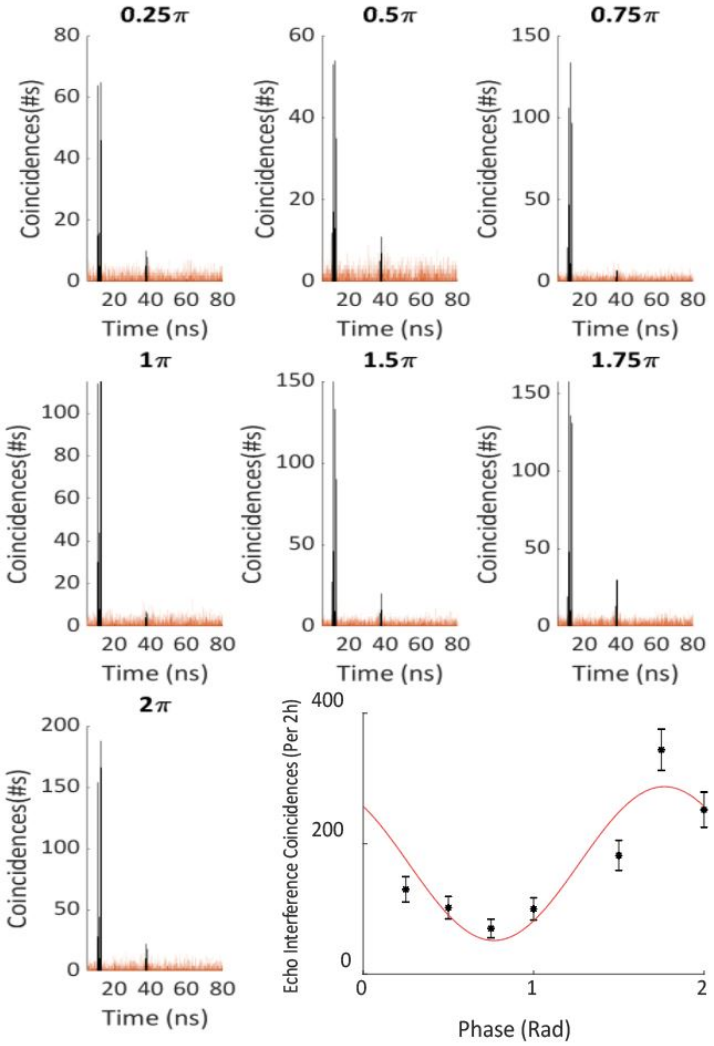

Figure 3.8: Each plot shows coincidences histograms generated by detection of time bin qubits in the $|+\rangle$ state from the SPDC source after storage for differently phased double combs. The central interference echo peak is highlighted in each plot. **(Inset)** Normalized Coincidence counts after projection of heralded single-photon qubits in state $|+X\rangle$ after re-emission onto $|\psi\rangle = (|e\rangle + exp\{i\varphi\}|l\rangle)/\sqrt{2}$ using differently phased double comb features.

BIBLIOGRAPHY

[1] J. H. Davidson, P. Lefebvre, J. Zhang, D. Oblak, and W. Tittel, "Improved light-matter interaction for storage of quantum states of light in a thulium-doped crystal cavity", Phys. Rev. A **101**, 042333 (2020).

[2] D. P. DiVincenzo, "The physical implementation of quantum computation", Fortschritte der Physik **48**, 771–783 (2000).

[3] S. Wehner, D. Elkouss, and R. Hanson, "Quantum internet: a vision for the road ahead", Science **362**, 10.1126/science.aam9288 (2018).

[4] A. I. Lvovsky, B. C. Sanders, and W. Tittel, "Optical quantum memory", Nature Photonics **3**, Review Article, 706 EP - (2009).

[5] M. R. Sprague et al., "Broadband single-photon-level memory in a hollow-core photonic crystal fibre", Nature Photonics **8**, 287 EP - (2014).

[6] J. Nunn, N. Langford, W. S Kolthammer, T. Champion, M. R Sprague, P. Michelberger, X.-M. Jin, D. England, and I. Walmsley, "Enhancing multiphoton rates with quantum memories", Physical review letters **110**, 133601 (2013).

[7] N. Sinclair et al., "Spectral multiplexing for scalable quantum photonics using an atomic frequency comb quantum memory and feed-forward control", Phys. Rev. Lett. **113**, 053603 (2014).

[8] C. Simon, H. de Riedmatten, M. Afzelius, N. Sangouard, H. Zbinden, and N. Gisin, "Quantum repeaters with photon pair sources and multimode memories", Phys. Rev. Lett. **98**, 190503 (2007).

[9] E. Saglamyurek et al., "A multiplexed light-matter interface for fibre-based quantum networks", Nature Communications **7**, Article, 11202 EP - (2016).

[10] J. Wolters, G. Buser, A. Horsley, L. Béguin, A. Jöckel, J.-P. Jahn, R. J. Warburton, and P. Treutlein, "Simple atomic quantum memory suitable for semiconductor quantum dot single photons", Phys. Rev. Lett. **119**, 060502 (2017).

[11] E. Saglamyurek et al., "Conditional detection of pure quantum states of light after storage in a tm-doped waveguide", Phys. Rev. Lett. **108**, 083602 (2012).

[12] C. Toninelli, K. Early, J. Bremi, A. Renn, S. Götzinger, and V. Sandoghdar, "Near-infrared single-photons from aligned molecules in ultrathin crystalline films at room temperature", Opt. Express **18**, 6577–6582 (2010).

[13] S. A. Moiseev, V. F. Tarasov, and B. S. Ham, "Quantum memory photon echo-like techniques in solids", Journal of Optics B: Quantum and Semiclassical Optics **5**, S497–S502 (2003).

[14]B. Kraus, W. Tittel, N. Gisin, M. Nilsson, S. Kröll, and J. I. Cirac, "Quantum memory for nonstationary light fields based on controlled reversible inhomogeneous broadening", Phys. Rev. A **73**, 020302 (2006).

[15]M. Afzelius, C. Simon, H. de Riedmatten, and N. Gisin, "Multimode quantum memory based on atomic frequency combs", Phys. Rev. A **79**, 052329 (2009).

[16]Y. L. Morgan P. Hedges Jevon J. Longdell and M. J. Sellars, "Efficient quantum memory for light", Nature **465**, 1052–1056 (2010).

[17]C. Clausen, I. Usmani, F. Bussières, N. Sangouard, M. Afzelius, H. de Riedmatten, and N. Gisin, "Quantum storage of photonic entanglement in a crystal", Nature **469**, 508–511 (2011).

[18]E. Saglamyurek et al., "Broadband waveguide quantum memory for entangled photons", Nature **469**, 512–515 (2011).

[19]N. Maring, P. Farrera, K. Kutluer, M. Mazzera, G. Heinze, and H. de Riedmatten, "Photonic quantum state transfer between a cold atomic gas and a crystal", Nature **551**, 485–488 (2017).

[20]Y.-L. Hua et al., "Storage of telecom-c-band heralded single photons with orbital-angular-momentum encoding in a crystal", Science Bulletin **64**, 1577–1583 (2019).

[21]M. Afzelius and C. Simon, "Impedance-matched cavity quantum memory", Phys. Rev. A **82**, 022310 (2010).

[22]M. Sabooni, Q. Li, S. Kröll, and L. Rippe, "Efficient quantum memory using a weakly absorbing sample", Phys. Rev. Lett. **110**, 133604 (2013).

[23]P. Jobez, I. Usmani, N. Timoney, C. Laplane, N. Gisin, and M. Afzelius, "Cavity-enhanced storage in an optical spin-wave memory", New Journal of Physics **16**, 083005 (2014).

[24]T. Zhong et al., "Nanophotonic rare-earth quantum memory with optically controlled retrieval", Science **357**, 1392–1395 (2017).

[25]R.-C. Tongning, T. Chanelière, J.-L. L. Gouët, and M. F. Pascual-Winter, "Optical clock transition in a rare-earth-ion-doped crystal: coherence lifetime extension for quantum storage applications", **605**, 012037 (2015).

[26]P. Zarkeshian et al., "Entanglement between more than two hundred macroscopic atomic ensembles in a solid", Nature Communications **8**, 906 (2017).

[27]T. Zhong et al., "Nanophotonic rare-earth quantum memory with optically controlled retrieval", Science **357**, 1392–1395 (2017).

[28]F. Marsili et al., "Detecting single infrared photons with 93% system efficiency", Nature Photonics (2013).

[29]L. Veissier, C. W. Thiel, T. Lutz, P. E. Barclay, W. Tittel, and R. L. Cone, "Quadratic zeeman effect and spin-lattice relaxation of Tm^{3+}:yag at high magnetic fields", Phys. Rev. B **94**, 205133 (2016).

[30]A. Kuzmich, W. P. Bowen, A. D. Boozer, A. Boca, C. W. Chou, L.-M. Duan, and H. J. Kimble, "Generation of nonclassical photon pairs for scalable quantum communication with atomic ensembles", Nature **423**, 731–734 (2003).

[31] S. Massar and S. Popescu, "Optimal extraction of information from finite quantum ensembles", Phys. Rev. Lett. **74**, 1259–1263 (1995).

[32] H. P. Specht, C. Nölleke, A. Reiserer, M. Uphoff, E. Figueroa, S. Ritter, and G. Rempe, "A single-atom quantum memory", Nature **473**, 190 EP - (2011).

[33] M. Gündo ğan, P. M. Ledingham, A. Almasi, M. Cristiani, and H. de Riedmatten, "Quantum storage of a photonic polarization qubit in a solid", Phys. Rev. Lett. **108**, 190504 (2012).

[34] V. Bu žek and M. Hillery, "Quantum copying: beyond the no-cloning theorem", Phys. Rev. A **54**, 1844–1852 (1996).

[35] H. de Riedmatten, M. Afzelius, M. U. Staudt, C. Simon, and N. Gisin, "A solid-state light-matter interface at the single-photon level", Nature **456**, 773 EP - (2008).

[36] I. Chuang, M. A. Nielsen, and E. L. Ginzton Laboratory, "Prescription for experimental determination of the dynamics of a quantum black box", J. Mod. Opt. **44**, 10 . 1080/09500349708231894 (2000).

[37] J. F. Poyatos, J. I. Cirac, and P. Zoller, "Complete characterization of a quantum process: the two-bit quantum gate", Phys. Rev. Lett. **78**, 390–393 (1997).

[38] A. Holzapfel, J. Etesse, K. T. Kaczmarek, A. Tiranov, N. Gisin, and M. Afzelius, "Optical storage on the timescale of a second in a solid-state frequency comb memory using dynamical decoupling", Arxiv (2019).

[39] C. Thiel, N. Sinclair, W. Tittel, and R. Cone, "Tm3+ : y3ga5o12 materials for spectrally multiplexed quantum memories", Physical review letters **113**, 160501 (2014).

4

A LONG-LIVED SOLID-STATE OPTICAL MEMORY FOR HIGH-RATE QUANTUM REPEATERS

Mohsen Falamarzi Askarani, Antariksha Das, Jacob H. Davidson, Gustavo C. Amaral, Neil Sinclair, Joshua A. Slater, Sara Marzban, Charles W. Thiel, Rufus L. Cone, Daniel Oblak, and Wolfgang Tittel

One of the keys to happiness is a bad memory.

Rita Mae Brown

We argue that long optical storage times are required to establish entanglement at high rates over large distances using memory-based quantum repeaters. Triggered by this conclusion, we investigate the $^3H_6 \longleftrightarrow H_4$ *transition at 795.325 nm of Tm:*$Y_3Ga_5O_{12}$ *(Tm:YGG). Most importantly, we show that the optical coherence time can reach 1.1 ms, and, using laser pulses, we demonstrate optical storage based on the atomic frequency comb protocol up to 100 µs as well as a memory decay time* T_M *of 13.1 µs. Possibilities of how to narrow the gap between the measured value of* T_M *and its maximum of 275 µs are discussed. In addition, we demonstrate quantum state storage using members of non-classical photon pairs. Our results show the potential of Tm:YGG for creating quantum memories with long optical storage times, and open the path to building extended quantum networks.*

Parts of this chapter, marked with a *, are published in Physical Review Letters **127**, 220502 [1]

4.1. PREAMBLE

The results of this paper are very promising for extending the storage time of Tm:YGG memories to a value which enables elementary quantum repeater links over many kilometers. To push further, we also demonstrate many of the principles that are required for building a frequency multiplexed quantum repeater. However, the storage efficiency is poor compared to that in the previous chapter. Tying together the improvements of these first two chapters is an ongoing theme that I look to build upon throughout this thesis.

4.2. INTRODUCTION*

THE future quantum internet [2, 3] will enable one to share entanglement and hence quantum information over large distances – ultimately between any two points on earth. To overcome attenuation in optical fibers, quantum repeaters are needed [4–8], many of which require quantum memories for light [9]. Such memories allow storing qubits, encoded into photons that have travelled over long distances, until feed-forward information becomes available. This information specifies which optical mode—including spectral, spatial and temporal modes—a qubit should occupy once it has been re-emitted from the memory. Note that the required mode assignment (or mode mapping operation) can happen in a memory-internal manner, e.g. by controlling when a photon is re-emitted (*aka* read-out on demand) [5, 10–12], or externally, e.g. by directing the emitted photon to a specific spatial mode [13] or by shifting its spectrum [7].

To maximize the entanglement distribution rate of a quantum repeater, qubits must be added continuously to the memory – not only once a previously stored qubit has been re-emitted but also while it is still being stored. Such multiplexed storage implies (a) the use of large ensembles of absorbers that enable bi-partite entanglement with many photonic qubits; and (b) that any memory-specific control operation, triggered by the absorption of a newly arriving qubit, must neither affect re-emission nor the possibility for mode mapping of a previously absorbed qubit. Stated differently, any control operation required after absorption of a qubit or a train of qubits must not introduce deadtime that prevents the memory from accepting additional qubits. This would cause a reduction of the memory's time-bandwidth product [14, 15] and, when used as an element of a quantum repeater, a reduction in the entanglement distribution rate (see the supplemental material for an example).

Unfortunately, the latter requirement of qubit independence (b) can be at odds with a high repetition rate. As we show below, one example is that of temporal multiplexing and read-out on demand in the so-called atomic frequency comb (AFC) quantum memory protocol, which requires one to temporarily map qubit states between optical and spin coherence [16]. This leads us to conclude that it is important to optimize the *optical storage time*, i.e. the time during which qubits are stored as optical coherence, which can be excited using visible or near infrared light. It is important to realize that this conclusion also holds in the case of purely optical storage (no spin mapping), and regardless of the degree of freedom used for multiplexing. Triggered by this finding, we investigate thulium-doped yttrium gallium garnet (Tm^{3+}:$Y_3Ga_5O_{12}$ or Tm:YGG) – a rare-earth-ion doped crystal (REIC) whose promising spectroscopic properties have

been demonstrated previously [17, 18], but whose potential for storing photonic qubits has not yet been established. Here we show that its optical coherence time T_2 can reach 1.1 ms, which is one of the longest times reported for any REIC [19, 20]. Motivated by this promising result, we investigate Tm:YGG for AFC-based memory, and demonstrate optical storage of laser pulses up to 100 μs. This is comparable with recent results obtained using Yb:Y_2SiO_5 [21] and Eu:Y_2SiO_5 [22], and exceeds all other reported results of storage of light in optical coherence with any REIC by at least a factor of 10. However, we also find that the memory decay time T_m of around 13 μs is 20 times smaller than the T_2-imposed maximum of 275 μs. Before addressing reasons for this large gap, we confirm the possibility for spectrally multiplexed storage and feed-forward-based spectral mode mapping [7], which allows using memory materials—including Tm-doped crystals—whose atomic level structure lacks the spin states required for memory-internal temporal mode mapping. Furthermore, we also show that quantum correlations between members of photon pairs persist throughout storage, i.e. that our memory can operate in the quantum regime. We conclude by mentioning reasons for the currently small memory efficiency, leaving more details to the supplemental material.

4.3. THE NEED FOR LONG OPTICAL STORAGE*

To support our claim that qubit independence can be at odds with a high repetition rate, let us discuss the example of temporal mode mapping using the AFC spin-wave memory in REICs [12]. As depicted in Fig. 4.1a, a pair of optical control pulses (π-pulses that resonantly couple the excited state $|e\rangle$ with a ground state $|s\rangle$) allows one to reversibly map optical coherence onto a spin transition. In this case, the timing of the second control pulse determines when the photons will be re-emitted from the memory, allowing for readout on demand.

Let us now assume that a first train, R1, of temporally multiplexed qubits has already been absorbed by the memory, that the first control pulse has been applied, and that a second train, R2, of qubits has just been added to the memory (Figs. 4.1b-d). At this point, R1 is stored in terms of spin coherence, and R2 in terms of optical coherence. Unfortunately, the subsequent control pulse, applied to the memory with the goal to map R2 onto spin coherence, simultaneously maps R1 back onto optical coherence. This causes re-emission of these qubits at a time that is determined by the need to transfer the second train, rather than by feed-forward information that specifies what to do with the first.

Fortunately, this problem can be avoided by storing only one train at a time. But in order to maximize the repetition rate of the repeater (or to minimize the memory's deadtime), this block, and hence the time during which qubits are stored in optical coherence, should be as long as possible – ideally as long as the total storage time. At the same time, long optical storage times allow maximizing the elementary link length in quantum repeater architectures that do not employ mapping between optical and spin coherence. In turn, this leads to higher entanglement distribution rates as it reduces the number of (currently inefficient) Bell-state measurements that are required to connect neighboring links [7].

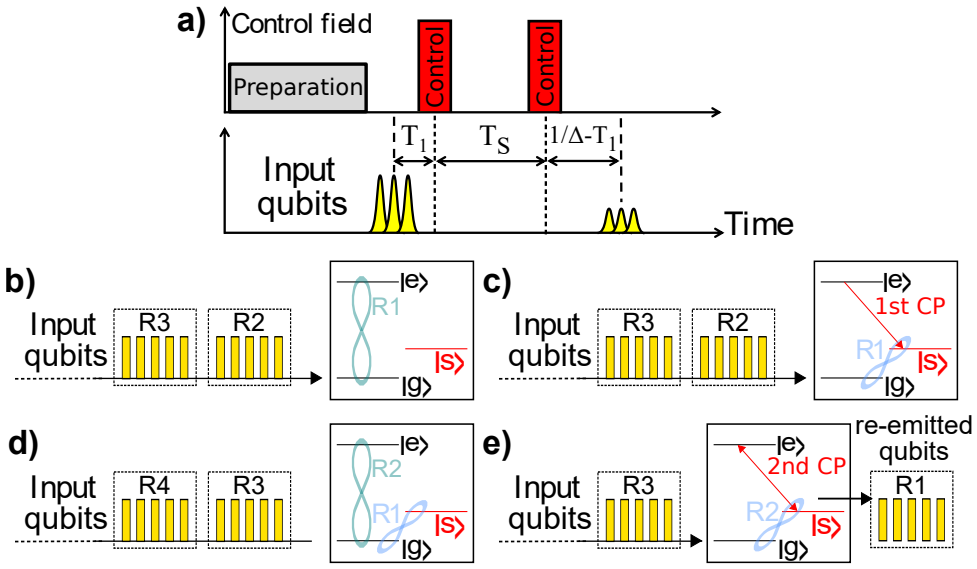

Figure 4.1: **Recall on demand using the AFC spin-wave storage protocol. a.** Pulse sequence. **b - e.** Memory input and output, as well as atomic coherence (indicated by light blue and green figures of eight) for different moments during storage (see text for details). Trains of qubits are labelled R1-R4; CP: Control Pulse. A three-level lambda system is formed by spin states $|g\rangle$ and $|s\rangle$, and by excited state $|e\rangle$.

4.4. TM:YGG AND EXPERIMENTAL SETUP*

Due to their unique spectroscopic properties [23], REICs have been broadly explored over the last two decades for quantum technology [24, 25], e.g. as ensemble-based quantum memory for light [9, 26, 27] or for quantum processing [28, 29]. But while significant effort has been spent to increase storage times in spin coherence [30–33]), much less work has been devoted to advancing and better understanding the limitations of storage in optical coherence. To address this shortcoming, we use a 25-mm long, 1% Tm:YGG crystal, mounted inside an adiabatic demagnetization refrigerator cooled to ~500 mK. YGG forms a cubic lattice in which Tm^{3+} replaces Y^{3+} in six crystallographically equivalent sites of local D_2 point group symmetry [34]. ideal Tm:YGG crystal is optically isotropic. Magnetic fields up to 2 T can be applied along the crystal < 111 > axis, splitting all electronic levels through the enhanced Zeeman interaction into two hyperfine sub-levels [18, 35]. Fig. 4.2 (Inset) depicts a simplified level structure.

We use a tunable continuous-wave diode laser at 795.325 nm wavelength to address the $^3H_6 \leftrightarrow {}^3H_4$ zero-phonon line. Due to the use of a non polarization-maintaining fiber, the polarization state at the input of the crystal is unknown. Furthermore, it evolves inside the crystal due to birefringence stemming from imperfect crystal growth [17]. The laser is frequency-locked to a high finesse cavity using the Pound-Drever-Hall method, resulting in an instability over ~100 μs below 20 kHz. To intensity- and frequency-modulate the light, we use a single-pass acousto-optic modulator (AOM) (driven by an RF signal generator) and a phase modulator (PM) (driven by an arbitrary waveform generator). After passing through the crystal's < 110 > direction, the light is directed to a photo-

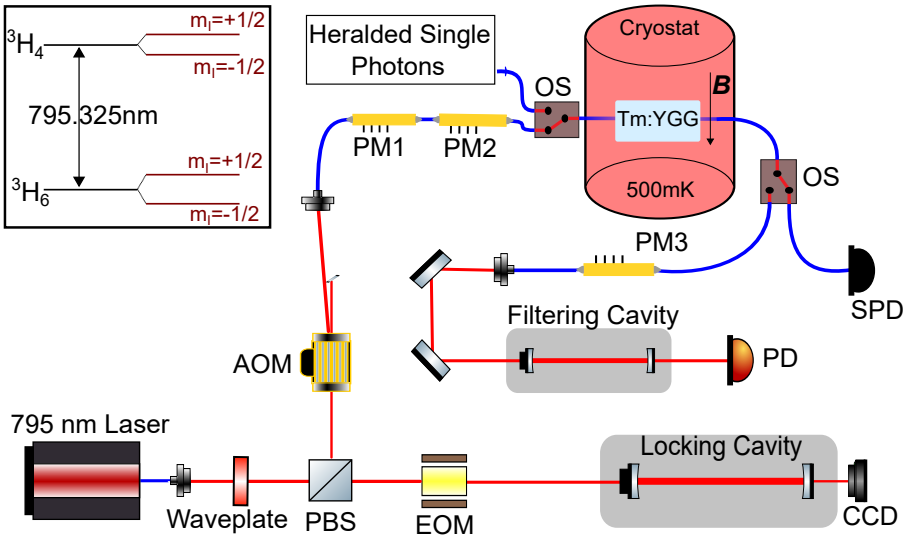

Figure 4.2: **Experimental setup**. AOM: acousto-optic modulator; PM: phase modulator; OS: optical switch; EOM: electro-optic modulator; PD: Classical photo detector; SPD: Single photon detector; CCD: charge-coupled device camera; ***B***: Magnetic field. Inset: Simplified energy level diagram of Tm:YGG showing the $^3H_6 \leftrightarrow ^3H_4$ zero-phonon line.

detector. This setup is used for AFC creation (see also [36]), initial memory characterization, and storage of optical pulses in a single spectral mode. For frequency-multiplexed storage and feed-forward recall, additional phase modulators are used to add frequency side-bands to the laser light, each of which creates a memory in a different spectral segment, and to frequency shift the light after re-emission so that only the desired spectral mode passes through an optical filter cavity [7]. In addition to laser pulse, we can also send heralded single photons into the memory, see Fig. 4.2.

4.5. MEASUREMENT AND RESULTS *

First, as a key property that determines the maximum optical storage time, we characterized the optical coherence time T_2 as a function of magnetic field using 2-pulse photon echoes [37]. As an important difference compared to our previous studies [17, 18], the temperature was lowered from 1.2 K to 500 mK. As shown in Figs. 4.3a,b and predicted earlier [17], this resulted in a very significant improvement of the coherence time from 490 μs to around 1.1 ms – one of the longest reported optical coherence times for any rare-earth crystal and approaching the limit of 2.6 ms imposed by the $^3H_4$ population lifetime [18]).

Next, we investigated the possibility for optical data storage, both using laser pulses as well as quantum states of light. Towards this end, we employed the two-level atomic frequency comb protocol [16]. An AFC is characterized by an absorption profile composed of evenly-spaced teeth in the frequency domain, which can be created using frequency-selective optical pumping of population from the troughs of the AFC to other atomic

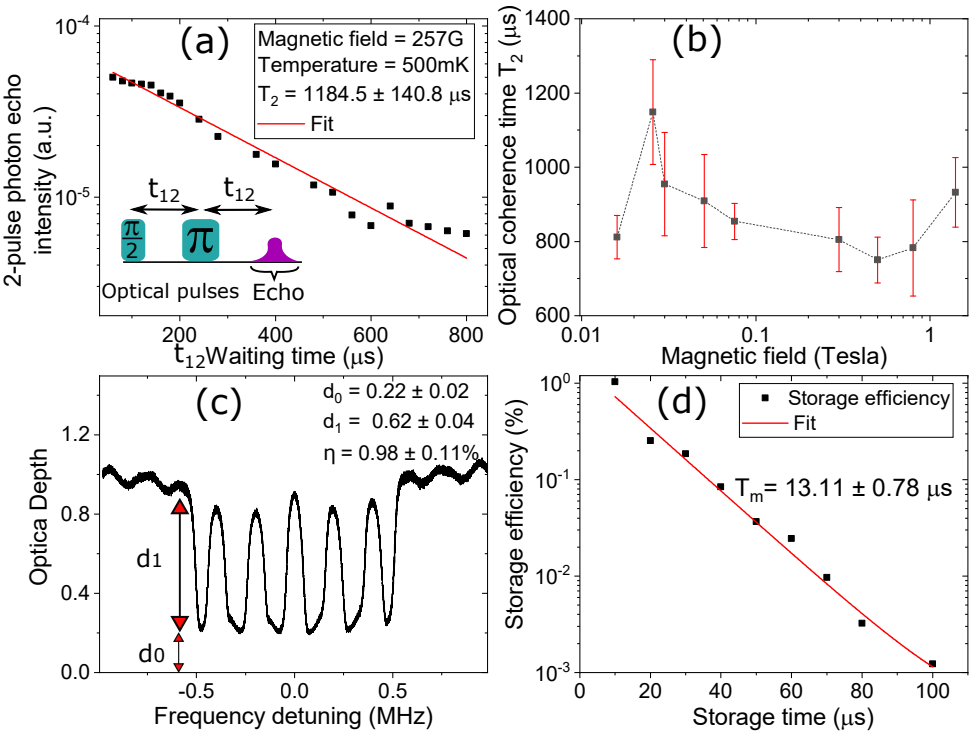

Figure 4.3: **Optical coherence, and optical data storage in a single spectral mode. a.** Exponential decay of the two-pulse photon echo signal as a function of the delay between the two optical pulses. **b.** Optical coherence time T_2 as a function of magnetic field. The dashed line guides the eye. **c.** AFC of 1 MHz bandwidth tailored for 5 μs storage time. The calculated efficiency, η, is approximately 1%. **d.** Measured memory efficiency as a function of storage time using AFCs with finesse 2. In all measurements T~500 mk. The error bars in (a) and (d) are smaller than the data points.

levels. Note that Tm:YGG is well suited for this task due to long-lived hyperfine levels within the electronic ground state manifold [18]. Absorption of a photon with wavenumber k by an AFC results in the creation of a collective atomic excitation described by $|\psi\rangle_A = N^{-1/2}\sum_{j=1}^{N} c_j e^{i2\pi\delta_j t} e^{-ikz_j}|e_j\rangle$. Here, N is the number of ions in the AFC, $|e_j\rangle$ a state in which only ion j is excited, δ_j the detuning of this ion's transition with respect to the input photon's carrier frequency, and z_j and c_j its position and excitation probability amplitude, respectively. After initial dephasing, the coherence rephases, resulting in re-emission of the photon after a time τ that is determined by the inverse AFC tooth spacing Δ, where $\tau = 1/\Delta$. See [16, 22] for more details. An example of an Tm:YGG AFC is depicted in Fig. 4.3c.

4.5.1. LONG-LIVED STORAGE OF LASER PULSES

Given the remarkable optical coherence time, it is important to assess how the memory efficiency evolves with storage time. To this end, we used 1 μs-long laser pulses (note that the use of true single photons would not change the results), and created AFCs with

finesse F—the ratio between AFC peak spacing Δ and peak width δ—of 2. See [7, 36] for more information. Tooth spacings varied between 100 kHz and 10 kHz, corresponding to storage times between 10 and 100 μs, respectively. The choice of F=2 maximizes the storage efficiency (see section 2B in the supplemental material), which was limited due to the crystal's small optical depth of around 1. The AFC bandwidth for all storage times was 0.5 MHz except for 100 μs, where it was reduced to 0.2 MHz. Due to the need for highly resolved AFCs with narrow-linewidth teeth, their preparation took 1 s. This time was followed by a waiting time of 20 ms—approximately 15 times the radiative lifetime of the $^3H_4$ level—to avoid detecting spurious photons caused by spontaneous decay of ions excited during the AFC preparation. The magnetic field in all measurements was around 100 G, which maximizes the optical coherence time.

We detected re-emitted pulses after up to 100 μs and found that the memory storage efficiency decreases exponentially as a function of storage time with a decay constant T_m =13.1±0.8 μs (see Fig. 4.3d). This value is much smaller than the ultimate limit T_m^{max} imposed by T_2 of around 275 μs. Possible reasons are listed in the outlook and detailed the supplemental material.

4.5.2. FREQUENCY-MULTIPLEXED STORAGE WITH FEED-FORWARD MODE MAPPING

To demonstrate spectral multiplexing, we prepared 11 AFCs with F=2, each of 1 MHz bandwidth and spaced by 10 MHz, over a total bandwidth of 100 MHz. Laser pulses of 1 μs duration were created in each spectral mode. They were stored and recalled after 5 μs (see Fig. 4.4a). Note that the individual modes were resolved by changing the resonance frequency of the filtering cavity (see Fig. 4.2). Assuming that five subsequent pulses—each of 1 μs duration—fit into the storage time, this results in a multimode capacity over spectral and temporal degrees of freedom of 55. Note that the storage time—significantly less than our maximum of 100 μs in this and all subsequent measurements—was limited by a trade-off between a more complex AFC tailoring procedure and memory efficiency. Otherwise, all parameters used to create the AFCs remained unchanged.

To implement feed-forward mode mapping, imposed by the use of a multiplexed memory in a quantum repeater, we furthermore demonstrated spectral shifting of the recalled laser pulses such that only the desired spectral mode was subsequently transmitted through a filter cavity with a fixed resonance frequency. Our approach, which is further explained in the supplemental material and in [7], is equivalent to the more well-known case of temporal multiplexing, in which one has to retrieve photons in specific temporal modes. Since the mode mapping in our case is performed in the frequency domain, the storage time of the memory is fixed; it corresponds to the round-trip time from the end of an elementary link to its center and back. The results of our proof-of-principle demonstration are depicted in Fig. 4.4b.

For these measurements, the internal storage efficiency (calculated by comparing the energies of input and re-emitted pulses and after considering coupling loss) was around 1.3%. Note that number of spectral channels can easily be increased with more laser power, allowing for paralleled AFC generation. Given the inhomogeneous broadening of the $^3H_6 \leftrightarrow {}^3H_4$ transition of 56 GHz, this could in principle yield thousands of

spectral modes. Furthermore, increasing the storage time by an order of magnitude—still much less then T_m^{max}—would improve the multi-mode capacity by another factor of ten.

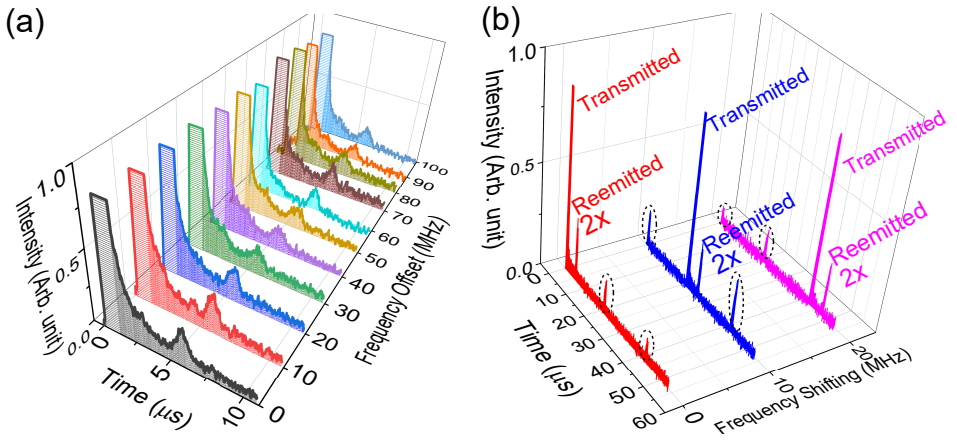

Figure 4.4: **Storage of data in multiple spectral modes. a.** Spectrally-multiplexed AFC quantum memory used to simultaneously store optical pulses in 11 spectral modes for 5 μs. **b.** Feed-forward mapping of spectral modes onto one with zero detuning. Laser pulses in three spectral modes were stored and re-emitted after 5 μs. Frequency shifting using phase modulator PM3 allowed mapping any desired mode onto one with zero detuning. Only this mode was transmitted through the filter cavity. The re-emitted pulses are magnified by a factor of 2, and crosstalk is indicated using dotted circles.

4.5.3. STORAGE OF HERALDED SINGLE PHOTONS

Finally, we verified that Tm:YGG, together with the two-level AFC protocol, is suitable for quantum state storage. As described in detail in [38], we created pairs of quantum-correlated photons at 795 and 1532 nm wavelength by means of spontaneous parametric down-conversion of strong laser pulses in a periodically-poled $LiNbO_3$ crystal. The detection of a 1532 nm photon using a superconducting nanowire single-photon detector heralded the presence of a 795 nm photon, which was directed into, stored in, and released after 43 ns from the Tm:YGG memory. Note that the memory creation procedure remained unchanged except that the AFC bandwidth was increased to 4 GHz to better match the photon bandwidth, and that the magnetic field was increased to 3 kG to match the difference in ground and excited state level splitting with the spacing between a trough and the neighboring tooth in the AFC [39]. The latter also increased the persistence of the AFC, allowing us to repeat the preparation sequence only every 10 s. Together with the preparation time of 1 s, this resulted in a memory availability of around 90%. The photons were then detected using a single-photon detector based on a silicon avalanche photodiode. The system efficiency, assessed by comparing photon detection rates with and without memory was 0.05%. Taking 15% fiber coupling into account, this yields an internal storage efficiency of 0.35%.

To verify that the non-classical correlations with the 1532 nm photons persist throughout the storage process, we measured the 2nd order cross-correlation coefficient $g_{12}^{(2)}(t)$

between the two photons of a pair using time-resolved coincidence detection [36]. Before storage, we found $g^{(2)}_{12}(0\,ns) = 18 \pm 0.02$ and, importantly, after 43 ns storage $g^{(2)}_{12}(43\,ns) = 4.58 \pm 0.46$ (this value is reduced due to excess loss combined with detector dark counts). See the supplemental material. Both values surpass the classical upper bound of 2, confirming the quantum nature of the photon source as well as the memory.

4.6. DISCUSSION AND CONCLUSION *

Our investigations have resulted in an optical coherence time T_2 up to 1.1 ms and optical storage times up to 100 μs. However, they also revealed a memory decay time of 13.1 μs – significantly smaller than the limit imposed by T_2, and in general a small recall efficiency. To increase the memory performance to a level that allows its use in a quantum network, several improvements, most, if not all of which are of technical nature, are required. As we describe in more detail in the supplemental material, this includes using a frequency-stabilized laser with narrower linewidth, a cryostat with reduced vibrations, a more stable magnetic field as well as finding parameters (propagation direction and polarization of the light, and external magnetic field) under which spectral diffusion due to ion-ion interactions is reduced and the $^3H_6 \leftrightarrow {}^3H_4$ transition becomes a so-called clock transition [35]. Furthermore, to counter the effects of limited optical depth, the light-atom interaction has to be enhanced using an impedance-matched cavity [31, 40–43]. This also removes the problem of re-absorption of photons that are emitted in forward direction. Furthermore, we can improve the optical pumping by changing the currently sequential excitation of narrow spectral intervals within the inhomogeneously broadened Tm transition by complex hyperbolic secant pulses [22, 44]. This will lead to better confined teeth with a more squarish spectral profile, and hence to a reduced background within the troughs in between these teeth. At the same time, it will also allow creating AFCs with higher finesse, resulting in reduced decoherence during photon storage [22, 45, 46].

Finally, note that despite the currently small multiplexing capability—in particular compared to the 1060 temporal modes in [47]—our demonstration shows the advantage of using atomic ensembles over single absorbers where it is limited to one. Note as well that coupling of a single spin, e.g. a diamond nitrogen-vacancy center, to neighboring nuclear spins does not solve this issue due to the limited number of interacting neighbors—e.g. 27 in [48]—and the small coupling strength.

We anticipate that further improvements of our work will lead to long-lived, efficient, and multi-mode optical quantum memories that enable the efficient distribution of entanglement across extended quantum networks.

4.7. SUPPLEMENTARY MATERIAL *

4.7.1. MEMORY DEADTIME AND REPEATER-BASED ENTANGLEMENT DISTRIBUTION RATE

To show the impact of a memory with dead-time on repeater performance, more precisely the impact on the entanglement distribution rate, we focus on the quantum repeater protocol described and analyzed in [7, 49, 50]. See Fig.S 4.5 for an illustration.

In this approach, a fixed number of qubits in n different spectral modes is created

at each node and sent towards the central location of the elementary link that connects to the neighboring node. Each qubit is entangled with a second qubit, also in one of n different spectral modes, whose states are mapped into a quantum memory where they are stored as *optical coherence* (not spin coherence). At the central location, a Bell-state measurement projects the transmitted qubits pairwise in a spectrally-resolved manner onto a maximally entangled state. This entangles qubits in the two memories–one on either end of the elementary link. After sending information about the channel(s) in which entanglement has been generated back to the two nodes, each node recalls all qubits from its memory and selects, out of the block of n, one (now entangled) qubit whose mode is subsequently shifted to allow for a Bell-state measurement with a qubit from the neighboring elementary link. Given the multi-mode capacity of the assumed memory as well as no dead-time, the next set of qubits can be created by the source and stored in the memory as soon as the creation of the previous set has been terminated.

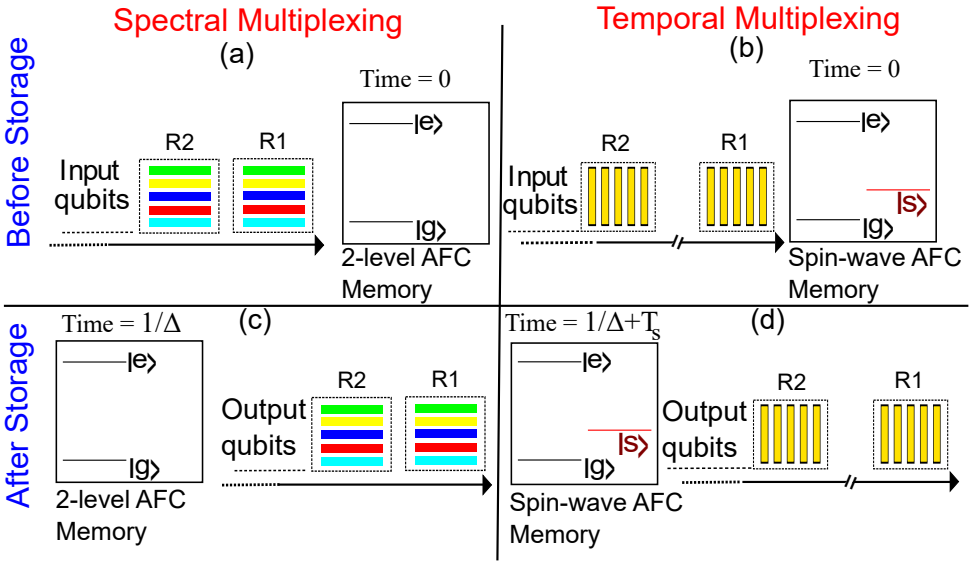

Figure 4.5: Illustration of storage sequence for spectral multiplexing (left-hand column) and temporal multiplexing (right-hand column). (a) and (b) represent the moment before storage, and (c) and (d) after storage. Two subsequent trains (or blocks) of qubits are labelled R1, R2. In (a) and (c), different colours represent different spectral modes. The three-level lambda system needed for read-out on demand is formed by spin states $|g\rangle$ and $|s\rangle$, and by excited state $|e\rangle$. Note how the dead-time of the spin-wave memory imposes a delay time between qubit trains R1 and R2 (in b and d).

Generalizing this approach to temporal modes, we arrive at the following: First, n qubits belonging to n entangled pairs in n subsequent temporal modes are created and sent to the central node of the elementary link. The other qubits of the n pairs are stored one after the other in optical coherence, and once the whole train of qubits has been mapped into the memory, it is transferred “en bloc" onto spin coherence. The outcome of a temporally-resolved Bell-state measurement at the central node then affects when the train of stored qubits is read out in each memory, ensuring that qubits from neighboring elementary links become indistinguishable in the temporal domain and can be

subjected to another Bell-state measurement. Unfortunately, the use of spin-states for photon storage implies that the memory is dead after absorption (and spin transfer) of the n qubits. And hence, we face the problem that the entanglement distribution rate is reduced by the ratio between optical storage time and total storage time.

4.7.2. AFC EFFICIENCY, GENERATION, LIMITATIONS AND FUTURE IMPROVEMENT

We found a very promising optical coherence time and demonstrated storage times of up to 100 μs. However, both the storage efficiency at zero storage time as well as its scaling with storage time have to be improved to make Tm:YGG suitable for use in a future quantum repeater. This sections deals with issues pertaining to this task.

AFC EFFICIENCY

As derived in detail in [16], the efficiency of an AFC-based memory depends on the optical depth of the teeth after pumping, d, the remaining optical depth within the troughs (which we refer to as the background), d_0, and the finesse, F. Furthermore, the tooth width, δ, affects how the efficiency scales with storage time. Assuming that δ is limited only by the homogeneous linewidth, γ_h, i.e. $\delta = 2\gamma_h$, and using $\gamma_h = 2/T_2$ [22], we find

$$\eta(\tau) = \left(\frac{d}{F}\right)^2 e^{-\frac{d}{F}} e^{-d_0} e^{-4\tau/T_2}. \tag{4.1}$$

For instance, for a finesse of 2, optical depths $d \approx 1$ and $d_0 \approx 0.4$, and T_2=1.1 ms, as in the storage of single photons, we calculate

$$\eta(\tau = 43ns) \approx 10.2\%. \tag{4.2}$$

AFC GENERATION – LEVEL SPLITTING AND TOOTH SEPARATION

Depending on the particular demonstration, we have created our atomic frequency combs using two different regimes: AFC *intrinsic pumping*, and AFC *extrinsic pumping*.

Intrinsic pumping – In the first case, optical pumping results in reduced optical depth in the troughs of the AFC, and an enhancement of the optical depth within the AFC teeth. This happens if the spacing between a trough and the neighboring tooth, Δ_{TT}, equals the splitting between a created hole and the neighboring anti-hole, which itself depends on the difference between the Zeeman splittings of the ground and excited level:

$$\Delta_{TT} = \Delta_{ge} = \Delta_g - \Delta_e = 1/(2\tau)$$

For the $^3H_6 \leftrightarrow ^3H_4$ transition in Tm:YGG, $\Delta_g \approx 106$ MHz/T and $\Delta_e \approx 63$ MHz/T. Note the last equation sign, which expresses that the inverse storage time $1/\tau$ equals twice the splitting between a trough and the next tooth. Note as well that this case implies that $\Delta_{TT} \ll \Gamma_{AFC}$, where Γ_{AFC} is the AFC width.

The advantages of working in this regime are that the AFC bandwidth is only limited by the inhomogeneous broadening of the transition, e.g. 56 MHz in Tm:YGG; and that the optical depth of the teeth is increased through the pumping procedure. On the flip-side, the maximum finesse is F=2 [39], which limits the efficiency (see Eq. 4.1).

Given the possibility for GHz-wide AFCs, we have used the intrinsic pumping regime in our demonstration of single photon storage. In the case of Tm:YGG, the (enhanced) Zeeman interaction results in $\Delta_{ge} \approx 43$ MHz/T, and the level splitting can easily be matched with the AFC periodicity for storage times in excess of a few tens' of nanoseconds. However, as the storage time approaches microseconds, the requirement for a reduced level splittings and hence a smaller magnetic field comes at the expense of lower Zeeman-level lifetime and less persistence [51], leaving less time to create and use the AFC.

Extrinsic pumping – As a second option, it is also possible to chose $\Delta_{ge} > \Gamma_{AFC} \gg \Delta_{TT}$ and to pump population outside the AFC.

This regime allows creating AFCs with higher finesse and hence reduced dephasing, albeit with generally small bandwidth. Also, the reduction of the optical depth within the troughs does not result in an increased depth of the teeth, which impacts the storage efficiency. But note that the use of an impedance-matched cavity allows reaching 100% efficiency despite the use of a storage material with limited optical depth (see below).

All AFCs used to store laser pulses were created using magnetic fields between 100 and 250 G. Even though this implies that we operated in the extrinsic pumping regime—the AFC width was at most 0.5 MHz—, we did not take advantage of the possibility to create AFCs with F>2 since this would have decreased the storage efficiency. Indeed, as described by Eq. 4.1, a larger finesse benefits the efficiency only in the case of sufficient optical depth d.

AFC LIMITATIONS AND FUTURE IMPROVEMENT

The measured efficiency for 43 ns-long single photon storage, 0.35%, is much smaller than the calculated value of 10.16 % in Eq. 4.2. This discrepancy is due to the existence of sources that cause tooth broadening beyond the value given by T_2. We come to the the same conclusion when comparing the decay constant T_m=13.1 μs, extracted from re-emission of stored laser pulses (see Fig. 3d in the main text), with the T_2-limited value of 275 μs.

1. **Laser instability –** Even though our laser is frequency stabilized, its remaining linewidth of around 20 kHz starts impacting the storage efficiency at a few microseconds storage time. To demonstrate efficient storage during 100 μs, a laser linewidth of around 1 kHz is required – a challenge that have been mastered using existing technology [52, 53].

2. **Magnetic field instability –** We also found that magnetic field noise, caused by an unstable current supply, led to spectral diffusion and hence a further degradation of the AFC quality. For a magnetic field of around 200 G and 1 sec AFC creation time, this effect was visible for storage times above 40 μs. Interestingly, the use of larger magnetic fields—desired to improve the AFC persistence—made this problem worse, which we attribute to the quadratic Zeeman effect. The quadratic Zeeman effect was also observed in [54]. The solution to this problem is to use a more stable power supply or a permanent magnet.

3. **Cryostat vibrations –** Even though the 500 mK plate inside the cryostat on which the Tm:YGG crystal was mounted is mechanically isolated from the pulse-tube

cooler, vibrations are expected to add additional decoherence. While its magnitude is currently unknown, similar observations have been reported in [21]. Future improvements include the use of a better cryostat, or better vibration isolation of the crystal inside [55].

4. **Spectral diffusion due to ion-ion coupling –** Spectral diffusion due to atom-atom interaction is also likely to play a role in the observed memory decay. For instance, a long-range quadrupole-quadrupole interaction between Tm ions may cause cross relaxation. The presence of this mechanism has been conjectured in the case of Tm:YAG, which features the same site symmetry as Tm:YGG [56]. Decreasing the Tm doping concentration may help reducing the impact of this interaction.

   An additional cause for perturbation of Tm ions is spin flips in neighboring gallium ions or by two-level systems [17]. To reduce spectral diffusion caused by varying magnetic fields at the Tm sites, we have started investigating the possibility of choosing a magnetic field direction for which the 795 nm Tm transition becomes insensitive to first order to magnetic field fluctuations [35, 57–60].

5. **Imperfect spectral hole burning –** Our spectral tailoring sequence, which relied on sequential optical pumping in one narrow frequency interval after the other, has furthermore resulted in non-ideal tooth shapes, i.e. teeth with significant "wings" that cause rapid dephasing. It has been shown that the use of complex hyperbolic secant pulses allows creating teeth with a more squarish shape, improving the storage efficiency [22, 44].

6. **Insufficient optical depth –** A general issue is that the optical depth of our crystal is insufficient to absorb all photons – a necessary condition for high-efficiency storage. As the tooth width is reduced and the finesse increased, this problem becomes more and more important (see Eq. 4.1).

   First, we note that our AFCs are currently created using uncontrolled, optically and magnetically inequivalent subsets of Tm ions. Using a better—non-birefringent—crystal and selecting a specific polarization state at its input will allow optimizing photon-ion interaction [61], resulting in improved optical depth and memory efficiency.

   Second, and being a more important improvement, the problem of insufficient optical depth can be removed by embedding the rare-earth crystal inside an impedance matched cavity. This has been shown theoretically and in experiment [31, 40–43]. As a first step towards this goal, we have tailored an AFC for 30 μs storage time with F = 4, see Fig.S 4.6. Using the measured values $d_0 \approx 0.005$ and $d \approx 0.03$, we predict an internal efficiency of 18%. This would enable a proof-of-principle demonstration of an elementary quantum repeater link. Naturally, the creation of AFCs with less background will result in a further increase of the efficiency. See [41] for an example reaching 56%.

7. **AFC background –** Remaining optical depth in the troughs of our AFCs resulted in irreversible absorption and hence photon loss. This was due to insufficient

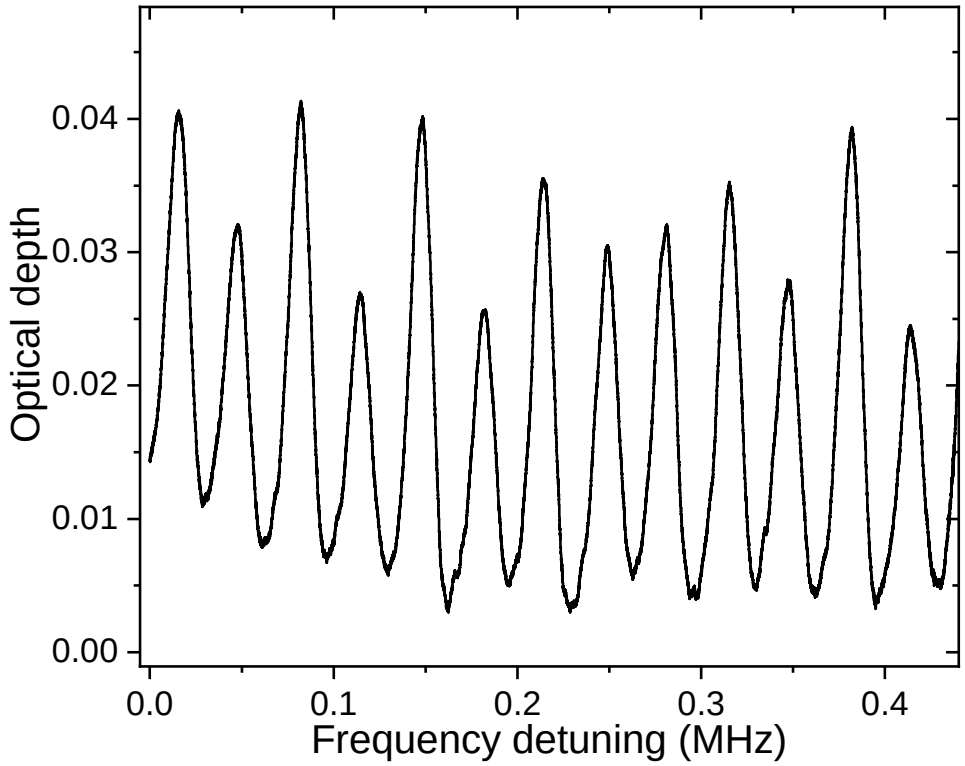

Figure 4.6: A 0.5 MHz AFC for 30 μs storage time with finesse 4

long optical pumping, insufficient laser power during pumping, or a combination thereof. To remove this problem, several options exist. First, assuming that we can reduce the magnetic field fluctuations mentioned above, we can operate at a larger magnetic field, thereby increasing the persistence of the AFCs and in turn the time for optical pumping. Second, as has been shown in [46, 62], it is possible to rapidly remove atomic population over a large spectral window using intense laser pulses, and then pump population in narrow spectral intervals back.

4.7.3. FEED-FORWARD MODE MAPPING

PROOF-OF-PRINCIPLE DEMONSTRATION

To demonstrate the possibility for feed-forward mapping between different spectral modes, we tailored, with the help of PM2, three AFCs spaced by 10 MHz in which spectrally matched optical pulses were stored. Pulses in different spectral modes were separated by 20 μs in order to make them distinguishable in time – a necessary feature for analysis since the filter cavity after the memory erased all spectral distinguishability.

First, we set the resonance frequency of the filtering cavity such that it allowed transmission of the spectral mode at zero frequency detuning– both for the light that was directly transmitted through the AFC as well as the stored and re-emitted pulse. The

measured signal is depicted in Fig. 4b in the main text in red. At the same time, the cavity largely suppressed the pulses at 10 and 20 MHz detuning. However, because the cavity linewidth of 7.5 MHz is comparable with the spectral mode spacing of 10 MHz, small fractions of the neighboring modes leaked through. This crosstalk is visible in the peaks in the red-colored signal trace centered at 20 and 40 μs.

Next, we drove PM3, positioned in-between the memory and the filter cavity, using a 10 MHz serrodyne signal that shifted all pulses emitted by the memory by -10 MHz. Consequently, the signal encoded originally at +10 MHz detuning, depicted in Fig. 4b (main text) in blue, became resonant with the cavity, resulting in its transmission through the cavity and the detection of a large peak at 20 μs followed by a smaller peak—the recalled pulse—5 μs later. As before, some leakage of signals in neighboring modes lead to peaks at 0 and 40 μs.

Finally, the same experiment was repeated with a serrodyne shift of -20 MHz. The result is depicted by the magenta-colored signal trace in Fig. 4b in the main text.

EFFICIENCY CONSIDERATIONS

As described above, feed-forward spectral mode mapping requires frequency shifting and spectral filtering. Below we describe several ways to realize shifting. Note that none is fundamentally limited in its efficiency. The same holds for the transmission through a filter cavity for which values of around 97%–only limited by spatial mode-matching—have been reported (see, e.g.,[63]).

To shift the spectra of the photons emitted from a quantum memory, first, it is possible to use an electro-optic modulator (e.g. a $LiNbO_3$ phase modulator) driven by a linearly rising voltage or a sawtooth function (then referred-to as serrodyne modulation [64, 65]). These methods are employed in the present work and in [7]. Frequency shifts of tens' of GHz can be achieved using commercially available devices, and we have demonstrated internal shifting efficiencies in excess of 90% over such bandwidth (e.g. in [66]). The device efficiency is furthermore affected by lossy coupling into and out of the modulator. In the present demonstration with commercial devices, we have achieved a total shifting efficiency of 0.45 (internal efficiency of 0.9, coupling efficiency 0.5). However, better mode matching between input/output fiber and waveguide of the modulator may make it possible to increase this value by a factor of two.

Another approach takes advantage of sum- or difference-frequency conversion in a nonlinear crystal [67]. It allows frequency shifts beyond 100 GHz, and system efficiencies in excess of 57% have already been demonstrated [68].

Lastly, arrays of coupled electro-optic micro-resonators can be used, see [69]. Frequency shift efficiencies of 99% have been reported for shifts of 28 GHz, and values up to 100 GHz seem feasible. Efficiencies are again limited by input and output coupling loss, with combined values up to 34% having been reported for similar devices [70, 71].

4.7.4. MEASUREMENTS OF THE CROSS-CORRELATION COEFFICIENT $g_{12}^{(2)}(0)$

To store classical optical pulses, we created AFCs with a bandwidth of around 1 MHz. But since the spectrum of the 795 nm photons, created by means of spontaneous parametric downconversion (SPDC), extends after filtering over 10 GHz, we increased the AFC

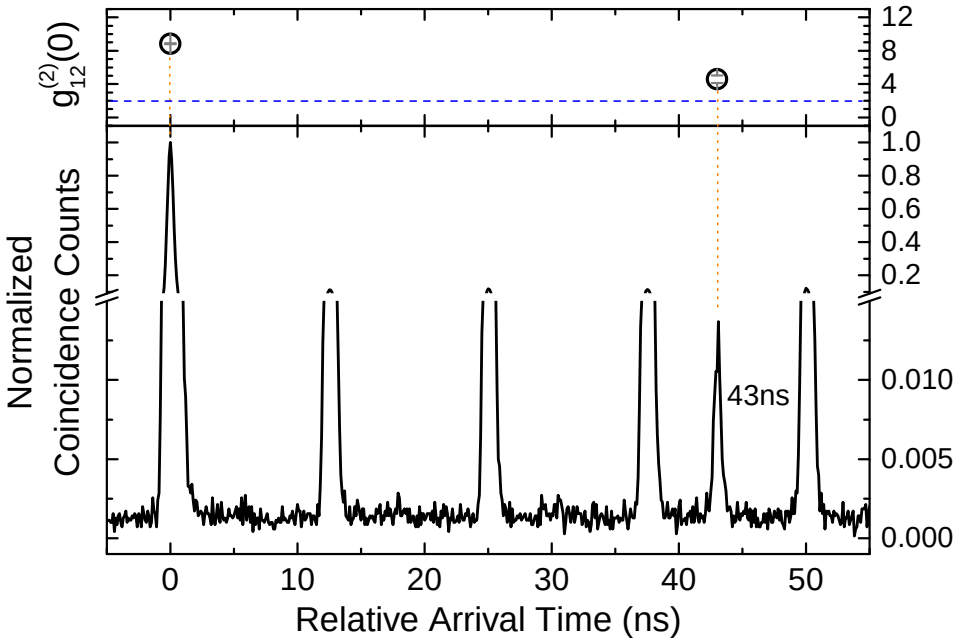

Figure 4.7: The lower and upper panels show, respectively, the coincidence-detection histogram and the 2nd order cross correlation coefficients $g^2_{12}(t)$ for transmitted as well as stored and subsequently re-emitted photons (the storage time was 43 ns). All arrival times are measured with respect to the detection time of the second member of each photon pair (the herald). The blue dashed line indicates the upper bound for classical fields of 2.

bandwidth to 4 GHz. This resulted in a reduced recall efficiency, even for a storage time of only 43 ns.

The second-order cross correlation function is defined as $g^{(2)}_{12}(t) = P_{12}(t)/P_1P_2$, where P_1 and P_2 denote the individual detection probabilities for the two photons per photon pair, and $P_{12}(t)$ is the probability for a joint (coincidence) detection occurring with time difference t. We note that the repetition period T of our pump laser is 12.5 ns, giving rise to “accidental" coincidences at integer multiples of T (see Fig. S4.7). Since these coincidences are proportional to P_1P_2 in the case of spontaneous parametric downconversion, the cross correlation coefficient can be calculated by taking the ratio of “desired" coincidence detections—in our case for t=0 ns and t=43 ns—and accidental detections: $g^{(2)}_{12}(t) = \mathrm{R}(t)/\langle \mathrm{R}(t+12.5\mathrm{ns})\rangle_\mathrm{n}$ where “$\langle..\rangle_\mathrm{n}$" denotes averaging over several repetition periods n. Analysing the coincidence histogram, we find $g^2_{12}(43ns) = 4.58 \pm 0.46$, which surpasses the classical upper bound of 2 by 5.6 standard deviations. This result demonstrates the quantum nature of our memory.

ACKNOWLEDGMENTS

The authors thank M. Grimau Puigibert, T. Chakraborty and O. P. Casas for experimental help and M. Afzelius for discussions. We acknowledge funding through the Netherlands

Organization for Scientific Research, the European Union's Horizon 2020 Research and Innovation Program under Grant Agreement No. 820445 and Project Name Quantum Internet Alliance, Alberta Innovates Technology Futures, the National Sciences and Engineering Research Council of Canada, the Alberta Ministry of Jobs, Economy and Innovation's Major Innovation Fund Project on Quantum Technologies. Furthermore, W.T. acknowledges funding as a Senior Fellow of the Canadian Institute for Advanced Research (CIFAR). This material is based in part on research at Montana State University sponsored by Air Force Research Laboratory under agreement number FA8750-20-1-1004.

BIBLIOGRAPHY

[1] M. F. Askarani et al., "Long-lived solid-state optical memory for high-rate quantum repeaters", Phys. Rev. Lett. **127**, 220502 (2021).

[2] H. J. Kimble, "The quantum internet", Nature **453**, 1023–1030 (2008).

[3] S. Wehner, D. Elkouss, and R. Hanson, "Quantum internet: a vision for the road ahead", Science **362**, 10.1126/science.aam9288 (2018).

[4] H.-J. Briegel, W. Dür, J. I. Cirac, and P. Zoller, "Quantum repeaters: the role of imperfect local operations in quantum communication", Phys. Rev. Lett. **81**, 5932–5935 (1998).

[5] L.-M. Duan, M. D. Lukin, J. I. Cirac, and P. Zoller, "Long-distance quantum communication with atomic ensembles and linear optics", Nature **414**, 413–418 (2001).

[6] N. Sangouard, C. Simon, H. De Riedmatten, and N. Gisin, "Quantum repeaters based on atomic ensembles and linear optics", Reviews of Modern Physics **83**, 33 (2011).

[7] N. Sinclair et al., "Spectral multiplexing for scalable quantum photonics using an atomic frequency comb quantum memory and feed-forward control", Phys. Rev. Lett. **113**, 053603 (2014).

[8] L. Jiang, J. M. Taylor, K. Nemoto, W. J. Munro, R. Van Meter, and M. D. Lukin, "Quantum repeater with encoding", Phys. Rev. A **79**, 032325 (2009).

[9] A. I. Lvovsky, B. C. Sanders, and W. Tittel, "Optical quantum memory", Nature photonics **3**, 706–714 (2009).

[10] M. Fleischhauer and M. D. Lukin, "Dark-state polaritons in electromagnetically induced transparency", Phys. Rev. Lett. **84**, 5094–5097 (2000).

[11] B. Kraus, W. Tittel, N. Gisin, M. Nilsson, S. Kröll, and J. I. Cirac, "Quantum memory for nonstationary light fields based on controlled reversible inhomogeneous broadening", PhysRevA.73.020302 **73**, 020302 (2006).

[12] M. Afzelius et al., "Demonstration of atomic frequency comb memory for light with spin-wave storage", Phys. Rev. Lett. **104**, 040503 (2010).

[13] Z.-Q. Zhou, Y.-L. Hua, X. Liu, G. Chen, J.-S. Xu, Y.-J. Han, C.-F. Li, and G.-C. Guo, "Quantum storage of three-dimensional orbital-angular-momentum entanglement in a crystal", Phys. Rev. Lett. **115**, 070502 (2015).

[14] K. F. Reim, J. Nunn, V. O. Lorenz, B. J. Sussman, K. C. Lee, N. K. Langford, D. Jaksch, and I. A. Walmsley, "Towards high-speed optical quantum memories", Nature Photonics **4**, 218–221 (2010).

[15] J.-P. Dou et al., "A broadband dlcz quantum memory in room-temperature atoms", Communications Physics **1**, 55 (2018).

[16] M. Afzelius, C. Simon, H. de Riedmatten, and N. Gisin, "Multimode quantum memory based on atomic frequency combs", Phys. Rev. A **79**, 052329 (2009).

[17] C. W. Thiel, N. Sinclair, W. Tittel, and R. L. Cone, "Optical decoherence studies of $Tm^{3+}:Y_3Ga_5O_{12}$", Phys. Rev. B **90**, 214301 (2014).

[18] C. W. Thiel, N. Sinclair, W. Tittel, and R. L. Cone, "$Tm^{3+}:Y_3Ga_5O_{12}$ Materials for spectrally multiplexed quantum memories", Phys. Rev. Lett. **113**, 160501 (2014).

[19] T. Böttger, C. W. Thiel, R. L. Cone, and Y. Sun, "Effects of magnetic field orientation on optical decoherence in $Er^{3+}:Y_2SiO_5$", Phys. Rev. B **79**, 115104 (2009).

[20] R. W. Equall, Y. Sun, R. L. Cone, and R. M. Macfarlane, "Ultraslow optical dephasing in Eu^{3+}:Y_2SiO_5", Phys. Rev. Lett. **72**, 2179–2182 (1994).

[21] M. Businger, A. Tiranov, K. T. Kaczmarek, S. Welinski, Z. Zhang, A. Ferrier, P. Goldner, and M. Afzelius, "Optical spin-wave storage in a solid-state hybridized electron-nuclear spin ensemble", Phys. Rev. Lett. **124**, 053606 (2020).

[22] P. Jobez, N. Timoney, C. Laplane, J. Etesse, A. Ferrier, P. Goldner, N. Gisin, and M. Afzelius, "Towards highly multimode optical quantum memory for quantum repeaters", Phys. Rev. A **93**, 032327 (2016).

[23] G. Liu and B. Jacquier, *Spectroscopic properties of rare earths in optical materials*, Vol. 83 (Springer Science & Business Media, 2006).

[24] C. Thiel, T. Böttger, and R. Cone, "Rare-earth-doped materials for applications in quantum information storage and signal processing", Journal of luminescence **131**, 353–361 (2011).

[25] T. Zhong and P. Goldner, "Emerging rare-earth doped material platforms for quantum nanophotonics", Nanophotonics **8**, 2003–2015 (2019).

[26] F. Bussieres, N. Sangouard, M. Afzelius, H. de Riedmatten, C. Simon, and W. Tittel, "Prospective applications of optical quantum memories", Journal of Modern Optics **60**, 1519–1537 (2013).

[27] K. Heshami, D. G. England, P. C. Humphreys, P. J. Bustard, V. M. Acosta, J. Nunn, and B. J. Sussman, "Quantum memories: emerging applications and recent advances", Journal of Modern Optics **63**, PMID: 27695198, 2005–2028 (2016).

[28] E. Saglamyurek, N. Sinclair, J. A. Slater, K. Heshami, D. Oblak, and W. Tittel, "An integrated processor for photonic quantum states using a broadband light–matter interface", New Journal of Physics **16**, 065019 (2014).

[29] A. Kinos et al., *Roadmap for rare-earth quantum computing*, 2021.

[30] Y. Ma, Y.-Z. Ma, Z.-Q. Zhou, C.-F. Li, and G.-C. Guo, "One-hour coherent optical storage in an atomic frequency comb memory", Nature Communications **12**, 2381 (2021).

[31] P. Jobez, I. Usmani, N. Timoney, C. Laplane, N. Gisin, and M. Afzelius, "Cavity-enhanced storage in an optical spin-wave memory", New Journal of Physics **16**, 083005 (2014).

[32] A. Seri, A. Lenhard, D. Rieländer, M. Gündo ğan, P. M. Ledingham, M. Mazzera, and H. de Riedmatten, "Quantum correlations between single telecom photons and a multimode on-demand solid-state quantum memory", Phys. Rev. X **7**, 021028 (2017).

[33]A. Seri, D. Lago-Rivera, A. Lenhard, G. Corrielli, R. Osellame, M. Mazzera, and H. de Riedmatten, "Quantum storage of frequency-multiplexed heralded single photons", Phys. Rev. Lett. **123**, 080502 (2019).

[34]J. F. Dillon and L. R. Walker, "Ferrimagnetic resonance in rare-earth doped yttrium iron garnet. ii. terbium substitution", Phys. Rev. **124**, 1401–1413 (1961).

[35]J. H. Davidson et al., "Measurement of the thulium ion spin hamiltonian in an yttrium gallium garnet host crystal", Phys. Rev. B **104**, 134103 (2021).

[36]M. l. G. Puigibert et al., "Entanglement and nonlocality between disparate solid-state quantum memories mediated by photons", Phys. Rev. Research **2**, 013039 (2020).

[37]Y. Sun, C. W. Thiel, and R. L. Cone, "Optical decoherence and energy level structure of 0.1%tm^{3+}:$linbo_3$", Phys. Rev. B **85**, 165106 (2012).

[38]M. Grimau Puigibert, G. H. Aguilar, Q. Zhou, F. Marsili, M. D. Shaw, V. B. Verma, S. W. Nam, D. Oblak, and W. Tittel, "Heralded single photons based on spectral multiplexing and feed-forward control", Phys. Rev. Lett. **119**, 083601 (2017).

[39]E. Saglamyurek et al., "Broadband waveguide quantum memory for entangled photons", Nature **469**, 512–515 (2011).

[40]M. Afzelius and C. Simon, "Impedance-matched cavity quantum memory", Phys. Rev. A **82**, 022310 (2010).

[41]M. Sabooni, Q. Li, S. Kröll, and L. Rippe, "Efficient quantum memory using a weakly absorbing sample", Phys. Rev. Lett. **110**, 133604 (2013).

[42]J. H. Davidson, P. Lefebvre, J. Zhang, D. Oblak, and W. Tittel, "Improved light-matter interaction for storage of quantum states of light in a thulium-doped crystal cavity", Phys. Rev. A **101**, 042333 (2020).

[43]M. Sabooni, S. T. Kometa, A. 6. e. w. Thuresson, S. Kröll, and L. Rippe, "Cavity-enhanced storage–preparing for high-efficiency quantum memories", New Journal of Physics **15**, 035025 (2013).

[44]M. Bonarota, J. Ruggiero, J. .-. L. Gouët, and T. Chanelière, "Efficiency optimization for atomic frequency comb storage", Phys. Rev. A **81**, 033803 (2010).

[45]L. Rippe, M. Nilsson, S. Kröll, R. Klieber, and D. Suter, "Experimental demonstration of efficient and selective population transfer and qubit distillation in a rare-earth-metal-ion-doped crystal", Phys. Rev. A **71**, 062328 (2005).

[46]B. Lauritzen, N. Timoney, N. Gisin, M. Afzelius, H. de Riedmatten, Y. Sun, R. M. Macfarlane, and R. L. Cone, "Spectroscopic investigations of eu^{3+}:y_2sio_5 for quantum memory applications", Phys. Rev. B **85**, 115111 (2012).

[47]M. Bonarota, J.-L. L. Gouët, and T. Chanelière, "Highly multimode storage in a crystal", New Journal of Physics **13**, 013013 (2011).

[48]M. H. Abobeih, J. Randall, C. E. Bradley, H. P. Bartling, M. A. Bakker, M. J. Degen, M. Markham, D. J. Twitchen, and T. H. Taminiau, "Atomic-scale imaging of a 27-nuclear-spin cluster using a quantum sensor", Nature **576**, 411–415 (2019).

[49]S. Guha, H. Krovi, C. A. Fuchs, Z. Dutton, J. A. Slater, C. Simon, and W. Tittel, "Rate-loss analysis of an efficient quantum repeater architecture", Phys. Rev. A **92**, 022357 (2015).

[50] H. Krovi, S. Guha, Z. Dutton, J. A. Slater, C. Simon, and W. Tittel, "Practical quantum repeaters with parametric down-conversion sources", Applied Physics B **122**, 52 (2016).

[51] E. Saglamyurek, T. Lutz, L. Veissier, M. P. Hedges, C. W. Thiel, R. L. Cone, and W. Tittel, "Efficient and long-lived zeeman-sublevel atomic population storage in an erbium-doped glass fiber", Phys. Rev. B **92**, 241111 (2015).

[52] Y. Zhao, J. Zhang, J. Stuhler, G. Schuricht, F. Lison, Z. Lu, and L. Wang, "Sub-hertz frequency stabilization of a commercial diode laser", Optics Communications **283**, 4696–4700 (2010).

[53] J. Liu, T. Liu, L. Chen, L. Zhang, G. Xu, D. Jiao, and S. Zhang, "A compact sub-hertz linewidth fabry perot cavity frequency stabilized laser for space application", Optics & Laser Technology **136**, 106777 (2021).

[54] L. Veissier, C. W. Thiel, T. Lutz, P. E. Barclay, W. Tittel, and R. L. Cone, "Quadratic zeeman effect and spin-lattice relaxation of Tm^{3+}:yag at high magnetic fields", Phys. Rev. B **94**, 205133 (2016).

[55] A. Louchet-Chauvet, R. Ahlefeldt, and T. Chanelière, "Piezospectroscopic measurement of high-frequency vibrations in a pulse-tube cryostat", Review of Scientific Instruments **90**, 034901 (2019).

[56] C. W. Thiel, R. M. Macfarlane, Y. Sun, T. Böttger, N. Sinclair, W. Tittel, and R. L. Cone, "Measuring and analyzing excitation-induced decoherence in rare-earth-doped optical materials", Laser Physics **24**, 106002 (2014).

[57] R.-C. Tongning, T. Chanelière, J.-L. Le Gouët, and M. F. Pascual-Winter, "Optical clock transition in a rare-earth-ion-doped crystal: coherence lifetime extension for quantum storage applications", in Journal of physics: conference series, Vol. 605, 1 (IOP Publishing, 2015), p. 012037.

[58] D. L. McAuslan, J. G. Bartholomew, M. J. Sellars, and J. J. Longdell, "Reducing decoherence in optical and spin transitions in rare-earth-metal-ion–doped materials", Phys. Rev. A **85**, 032339 (2012).

[59] A. Ruskuc, J. M. Kindem, J. G. Bartholomew, J. Rochman, Y. Q. Huan, and A. Faraon, "Coherent optical and spin dynamics of single 171yb ions embedded in a nanophotonic cavity", in Osa quantum 2.0 conference (2020), QTh6A.7.

[60] A. Ortu, A. Tiranov, S. Welinski, F. Fröwis, N. Gisin, A. Ferrier, P. Goldner, and M. Afzelius, "Simultaneous coherence enhancement of optical and microwave transitions in solid-state electronic spins", Nature Materials **17**, 671–675 (2018).

[61] Y. Sun, G. M. Wang, R. L. Cone, R. W. Equall, and M. J. M. Leask, "Symmetry considerations regarding light propagation and light polarization for coherent interactions with ions in crystals", Phys. Rev. B **62**, 15443–15451 (2000).

[62] M. P. Hedges, J. J. Longdell, Y. Li, and M. J. Sellars, "Efficient quantum memory for light", Nature **465**, 1052–1056 (2010).

[63] G. Kowzan, D. Charczun, A. Cygan, R. S. Trawiński, D. Lisak, and P. Masłowski, "Broadband optical cavity mode measurements at hz-level precision with a comb-based vipa spectrometer", Scientific Reports **9**, 8206 (2019).

[64]D. M. S. Johnson, J. M. Hogan, S.-w. Chiow, and M. A. Kasevich, "Broadband optical serrodyne frequency shifting", Opt. Lett. **35**, 745–747 (2010).

[65]R. Houtz, C. Chan, and H. Müller, "Wideband, efficient optical serrodyne frequency shifting with a phase modulator and a nonlinear transmission line", Opt. Express **17**, 19235–19240 (2009).

[66]M. Grimau Puigibert, G. H. Aguilar, Q. Zhou, F. Marsili, M. D. Shaw, V. B. Verma, S. W. Nam, D. Oblak, and W. Tittel, "Heralded single photons based on spectral multiplexing and feed-forward control", Phys. Rev. Lett. **119**, 083601 (2017).

[67]P.-C. Wang, O. Pietx-Casas, M. F. Askarani, and G. C. do Amaral, "Proposal and proof-of-principle demonstration of fast-switching broadband frequency shifting for a frequency-multiplexed quantum repeater", J. Opt. Soc. Am. B **38**, 1140–1146 (2021).

[68]T. van Leent, M. Bock, R. Garthoff, K. Redeker, W. Zhang, T. Bauer, W. Rosenfeld, C. Becher, and H. Weinfurter, "Long-distance distribution of atom-photon entanglement at telecom wavelength", Phys. Rev. Lett. **124**, 010510 (2020).

[69]Y. Hu, M. Yu, D. Zhu, N. Sinclair, A. Shams-Ansari, L. Shao, J. Holzgrafe, M. Zhang, and M. Loncar, "Electro-optic frequency shifting using coupled lithium-niobate microring resonators", in Conference on lasers and electro-optics (2020), STu4J.4.

[70]S. F. Preble, Q. Xu, and M. Lipson, "Changing the colour of light in a silicon resonator", Nature Photonics **1**, 293–296 (2007).

[71]M. Lauermann et al., "Integrated optical frequency shifter in silicon-organic hybrid (soh) technology", Opt. Express **24**, 11694–11707 (2016).

5

Optical Properties of Thulium Doped Yttrium Gallium Garnet

Jacob H. Davidson, Dorian Oser, and Wolfgang Tittel

Mankind is not a circle with a single center but an ellipse with two focal points of which facts are one and ideas the other.

Victor Hugo

We report measurements of the frequency dependence of the complex index of refraction for 2% doped Thulium Yttrium Gallium Garnet (Tm:YGG) where the Tm resonances are easily identified and separated from the behavior of the host material. This crystal was examined using variable-angle spectroscopic ellipsometry to measure and fit the desired properties over a range spanning 210-1680nm (0.73-5.9 eV). Transmission and reflection data from this sample allow the determination of the complex index of refraction which was previously unknown. Precise knowledge of optical material properties are critical for many applications of YGG including constructing precise optical cavities, laser based applications, and quantum information devices. A complete database of obtained optical parameters (real and imaginary parts of complex refractive index) over this whole spectral range is included in the supplementary information.

Building on this investigation, this chapter also describes how to design and deposit Bragg mirrors directly onto the garnet substrate to create monolithic optical cavity devices. This is relevant for creating high efficiency quantum memories for light.

Large portions of this chapter, marked with a star *, will be submitted to Optical Materials Express.

5.1. PREAMBLE

Modern photonic communication hardware is often fiber coupled for easy integration. This is the archetype that we seek to create with the monolithic quantum memories that were the subject of chapter 3. The information in this chapter about the optical material properties of YGG is essential to reach this goal. Let this chapter serve as foreshadowing for the creation of monolithic cavity devices from Tm:YGG to combine all improvements in this thesis.

Additionally, although impedance matched cavities are known to provide a potential path to create efficient AFC memories, there have been only 5 experiments to date which show results of increased efficiency [1–5] all of which remain below 90 %. These studies represent five valuable yet still limited resources for achieving full understanding the technical limitations that become important when employing these cavity based memories in quantum repeater schemes.

This chapter is a step towards the capability to mass produce these monolithic cavity devices. Work in this direction will result in the capability to tune and measure many different regimes of intra-cavity loss and mirror reflectivity to gain a better understanding of the experimental limitations to this scheme. The goal is to enable creation of memories with truly high efficiency approaching unity.

5.2. INTRODUCTION*

KEY among modern photonic materials are garnet crystals which are used in many optical devices, most commonly for laser crystals such as Nd:YAG [6–8]. Detailed studies of the complex index of refraction for YAG and LuAG materials have enabled these applications in these better known aluminum garnets. As a key building block of photonic technologies additional materials with similar properties (hardness, optical isotropy, chemical stablity, etc.), yet different optical properties are essential for expanding upon these applications. In this regard, gallium based garnets provide many of the material benefits seen from the aluminum garnets, but with a higher index of refraction, as in the case of gadolinium scandium gallium garnet (GSGG) [9]. Precise studies of the optical properties for gallium garnet materials seek to enable the use of these materials across many optical technologies.

Thus, yttrium gallium garnet ($Y_3Ga_5O_{12}$, YGG) possesses great potential use in optical applications, but has not been been characterized to the same degree as its aluminum garnet counterparts. Previously, YGG, with various rare earth dopants, has been used to create lasers or waveguides across many frequencies [10, 11]. Additionally, YGG has shown potential in applications such as lenses for high energy lithography [6], LIDAR [12], and quantum information [13, 14]. With such a broad base of applications, an equally broad understanding of the material optical properties is essential but to the best of our knowledge, the refractive index of YGG has been measured only at certain specific frequencies [15–18]. The spectral dependence of the complex index of refraction for YGG remains unknown with only a single study of the real portion conducted [19] over a broad frequency range.

With these measurements, we fill this gap by determining the real and imaginary portions of the index of refraction for a single crystal of 2% Tm^{3+}:YGG over a broad range

of frequencies. The properties due to the host and the dopant ions are easily separated. Experimental data is gathered using variable angle spectroscopic ellipsometry (VASE) to determine this material's optical properties over the range from 210-1680 nm (0.73-5.9 eV). The presented data will serve as a key resource for the use of YGG in many applications going forwards in photonics and laser physics.

5.3. EXPERIMENTAL SETUP*

The measurements were conducted using a piece of single YGG crystal grown at Scientific Materials Corp. using their ultra high precision Czochralski growth method. In this case, the sample was doped with an additional 2% thulium atoms which substitute for the yttrium sites in the crystal lattice. The sample was cut into a 5 by 8 by 10 mm rectangular prism selected from a low strain portion of the boule. Due to the isotropic nature of this crystal, the results for any orientation can be expected to extend across all crystalline directions [20, 21]. All surfaces for the transmission and VASE measurements were polished to optical quality.

The ellipsometry measurements were conducted on the polished 5x8 mm faces with a variable-angle J.A. Woolam M 2000 Ellipsometer. Reflection measurements were taken for a series of incidence angles between 50° and 70° in steps of 5°. To measure transmission we chose an incidence angle of 0 degrees, normal to the 5 by 8mm face such that the beam propagated along the $< 1\bar{1}0 >$ crystalline axis. Spectroscopic data spanning the range of 210-1680 nm (0.73-5.9 eV) was measured for all measured angles.

5.4. RESULTS*

Variable-angle spectroscopic ellipsometry measurements begin with a known polarization, frequency, and reflection angle. For each of these points, data, ρ is collected and used to plot a pair of quantities Ψ and Δ given by.

$$\rho = \frac{R_p}{R_s} = \tan(\Psi) e^{i\Delta} \tag{5.1}$$

Here, ρ is the ratio between complex reflection coefficients R_p, R_s for p and s polarization components of the reflected light [22, 23]. Linearly polarized light incident on the sample is reflected in an elliptically polarized state which is analyzed by a rotating polarizer to produce values of Ψ and Δ for each particular input of polarization, frequency, and angle [22, 23]. With λ the wavelength of each particular measurement, $\Psi(\lambda)$ and $\Delta(\lambda)$ curves for the measured YGG material are shown in Figure 5.1 with a matching model for an infinite substrate simulated in Woolam's CompleteEase software.

The $\Psi(\lambda)$ and $\Delta(\lambda)$ values for each input allow estimating the index of refraction at each frequency. Using the integrated modeling software, a B-Spline function [24–27] is fit to the data as a function of wavelength to produce curves for the real part of the index of refraction, n, across the entire measured range with the lowest possible mean standard error (MSE). The MSE of the curves pictured in Fig. 5.1 is 5.06 which shows good agreement with the model of the experimental data, comparable to that of other materials [28, 29]. This fitting procedure yields the wavelength dependence for the index of refraction in this material shown in Figure 5.2. Furthermore, for comparison and to

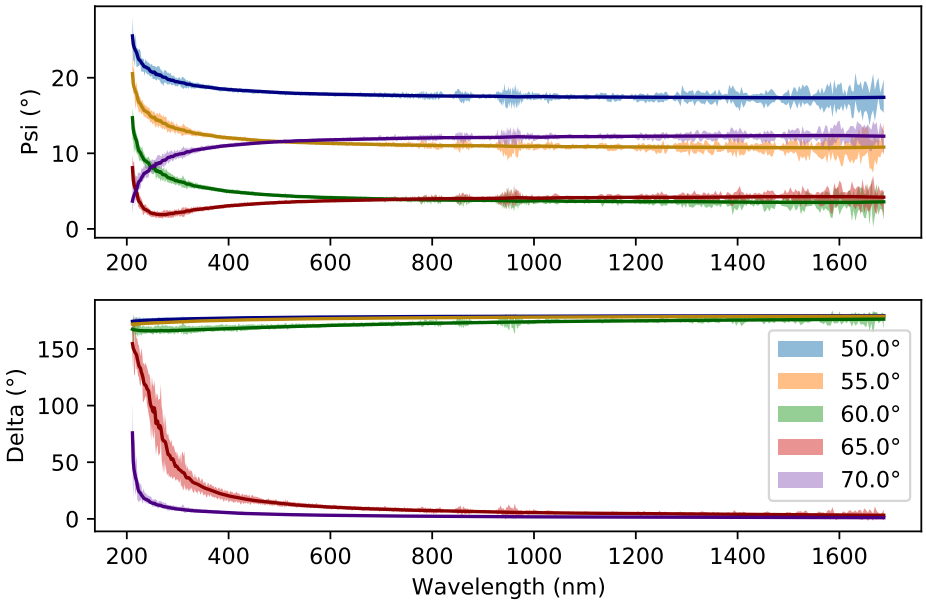

Figure 5.1: Psi and Delta Curves for measurements at various angles of incidence. Curves shown in different colors indicate measured data for different angles of incidence. The model generated to fit is shown by the solid lines and shows good agreement with the measured data.

validate our measurement and fitting methods are literature and measured data for a 0.1% Tm:YAG crystal [28] which show good agreement. For VASE measurements there is very little interaction with the material from a single surface reflection leaving sets of measured data unaltered by the presence of a small percentage of dopant ions. The index of this material is clearly higher than that of YAG, showing the presence of the gallium in the chemical composition of this crystal.

To determine the absorption coefficient, k, of the YGG material itself, we measure the transmission spectrum of the crystal sample, shown in Figure 5.3. From this transmission measurement it immediately becomes clear that Tm ions are present in this crystal sample by examining the spectral regions they dominate (460, 680, 790, 1210, and 1600nm) [30, 31]. Using Python's 1-D interpolation function, seen in 5.3, we separate the portions of absorption which belong to the dopant Tm ions. After removing these regions we consider the the global shape of the measured transmission to be a property of YGG. Using this remaining transmission data in conjunction with the VASE reflection data, we calculate the extinction coefficient of the material also shown in figure 5.3. Values for k in this material are extremely small, showing the high optical quality of the crystal.

5.5. CONCLUSION*

We have measured the frequency dependence of the real and imaginary parts of the index of refraction for yttrium gallium garnet over a broad spectral range between 210-

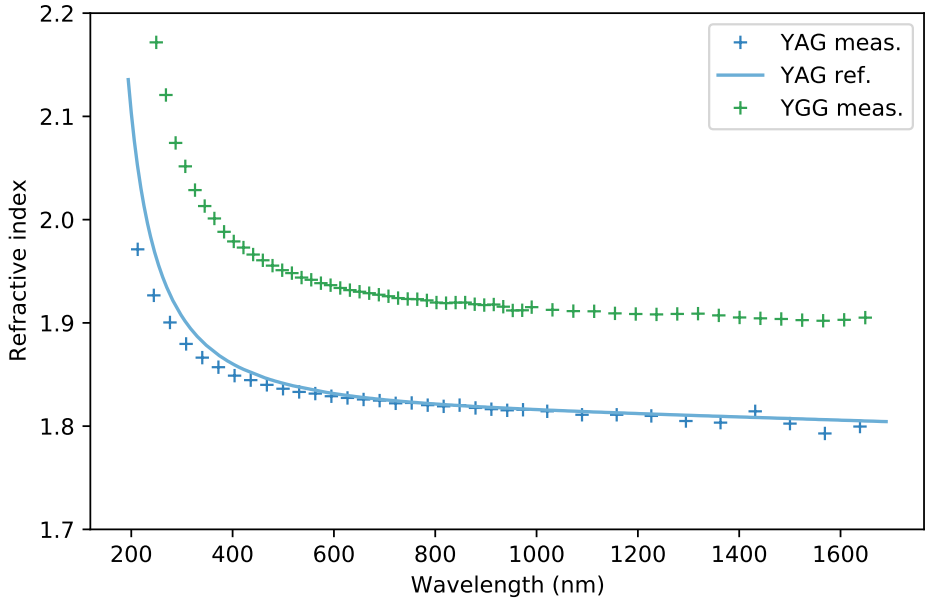

Figure 5.2: Spectral dependence of the real index of refraction for the YGG material shown in black. The index of refraction curve is derived from the fitted data in figure 5.1. To validate our fitting method, pictured in orange is a measurement of a 0.1% Tm:YAG crystal by the same method as well the same curve in blue from literature [28].

1680 nm (0.73-5.9 eV). This study provides an important resources for those looking to create optical devices from YGG for a number of different applications.

ACKNOWLEDGMENTS

The authors thank L.Shreik for discussions and training on the ellipsometer. We acknowledge funding through the Netherlands Organization for Scientific Research, and the European Union's Horizon 2020 Research and Innovation Program under Grant Agreement No. 820445 and Project Name Quantum Internet Alliance.

5.6. MIRROR FABRICATION ON A YGG SUBSTRATE

5.6.1. BRAGG MIRROR DESIGN

As seen in chapter 3, cavity enhancement of poor absorption can create unparalleled gains in the efficiency of a rare earth based AFC quantum memory. In addition to characterizing the optical material properties, we sought to design the front and rear mirrors in house and deposit them directly onto the garnet material.

Bragg mirrors are the 1-D version of sub-wavelength structures that create a photonic band gap, preventing the propagation of light through a material [33–35]. As an optical component, they are commercially available in many different forms [36]. As

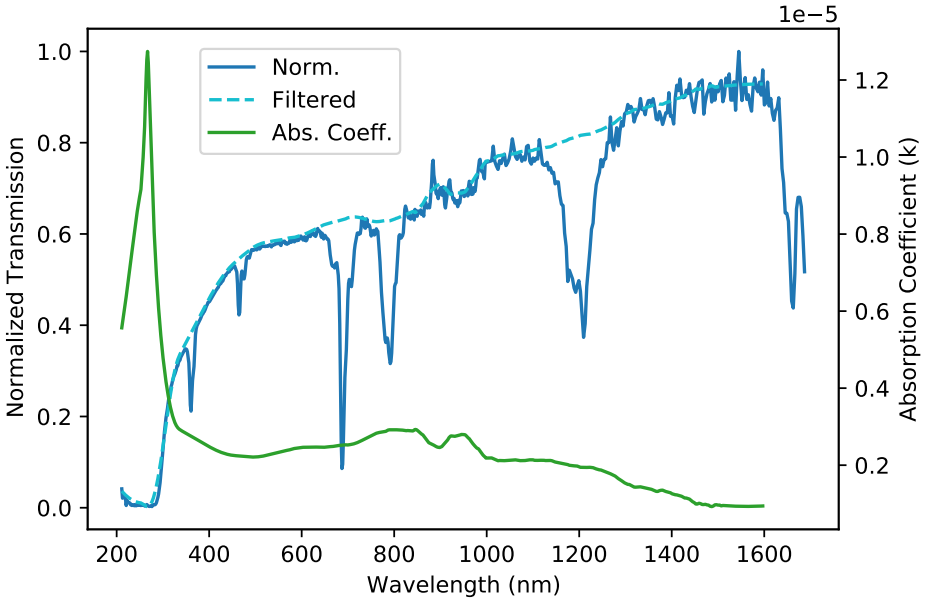

Figure 5.3: Transmission spectrum of a 2% Tm:YGG sample. The transmission data, black, clearly shows the signature of the Tm^{3+} ions. All sharp dips in this absorption spectrum can be associated with a particular atomic resonance of Tm at room temperature [30–32]. The orange curve shows the result of our interpolation function that removes the affected spectral portions. Blue points show the extinction coefficient.

a cavity mirror, they make an attractive and common option because they can be constructed from lossless dielectric materials for a particular wavelength while creating high reflectivity.

To design a Bragg mirror, one begins with the wavelength to be reflected, the angle of incidence, the polarization of the input light, and the desired reflectivity. From these initial parameters a recipe, which results in a sub-wavelength spatial modulation of the index of refraction, can be designed that will yield a mirror with the required spectrum. For normal incidence of arbitrary polarization, making a quarter wave stack is a simple recipe for high reflectivity. It consists of alternating layers of high and low index, each $\lambda/(4n_{mat})$ nm thick, which creates destructive interference in the forward direction, leaving reflection that depends on the number of repeated periods of this spatial grating [37]. Carrying out this, or any other, recipe requires nano-fabrication which is discussed in the following sub-section.

Considering the wavelength of our needed mirror, the 795 nm transition of Tm ions in garnet hosts, we identified some easily depositable, lossless materials with a significant difference in index of refraction at this wavelength. Silicon dioxide, SiO_2 with $n_1(795\text{ nm}) \approx 1.47$ [38], and Silicon Nitride, Si_3N_4 with $n_2(795\text{ nm}) \approx 1.88$ [39] make a very accessible pairing. Shown in figure 5.4 is the simulated spectrum of the reflectivity of a coating consisting of 21 alternating layers that form a quarter-wave stack.

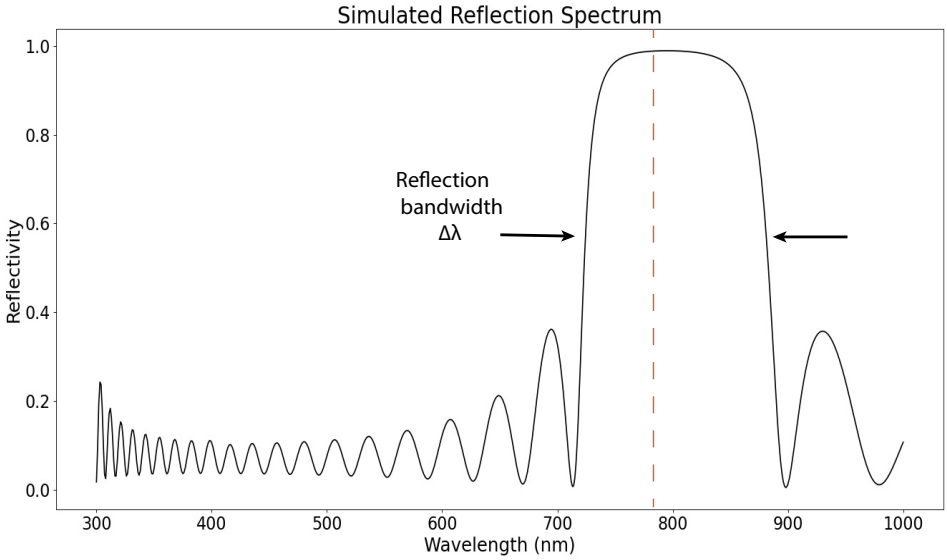

Figure 5.4: Simulated spectrum of 21 layers of SiO_2 and Si_3N_4 forming a quarter wave stack for light around 795nm. Reflectivity at 795 nm (indicated by the dashed line) is above 99%. The reflection spectrum is created using the OpenFilters Software package for thin film design [40].

The high refractive index difference of SiO_2 and Si_3N_4 yields a high reflectivity of around 99% after only 21 layers. This difference is also responsible for the large bandwidth of the reflective region, making this design robust to uncertainty of 5-10 nm in layer thickness for creating high reflectivity at 795 nm. With the materials selected and the quarter wave stack designed, we turn to how to deposit thin films of these materials.

5.6.2. RF SPUTTERING OF DIELECTRIC MATERIALS

Both SiO_2 and Si_3N_4 can be deposited on various substrates via dielectric RF sputtering [41], although with different deposition parameters [42, 43]. The deposition rate of each material is a function of vacuum pressure, argon gas flow, RF power to heat the target, and bias voltage on the substrate. Once a set of parameters is chosen this process is fairly repeatable, and small changes to deposition parameters lead mainly to small changes in the resulting deposition, making it feasible to make adjustments towards the correct recipe. For an easy handle to change the thickness of the deposited layer, deposition time is the easiest to control once the other deposition parameters create nicely sputtered layers.

Shown in figure 5.5 is a deposited set of 21 layers on a silicon wafer. The alternating structure of the two materials is clear and consistent with successive repetitions of the same layer recipe. This particular structure produced a reflectivity of 95% at 795 nm, in good agreement with the previous modeling once the correct layer thicknesses were determined. The poly-crystalline nature of the deposited layer is visible in these images, and is likely not ideal for low-loss optical applications.

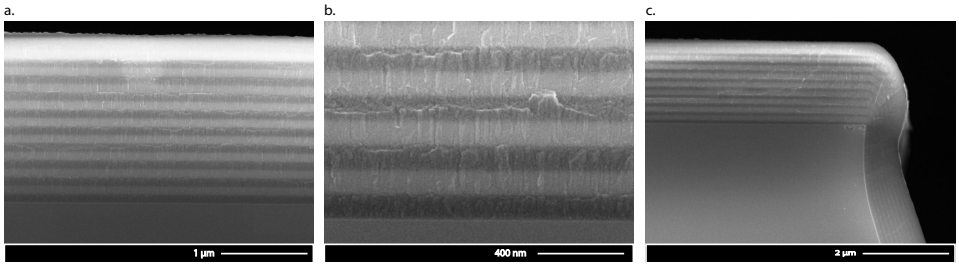

Figure 5.5: SEM images of the deposited layer stack on a silicon substrate. **a.** A stack of 21 layers of alternating SiO_2 and Si_3N_4. The top most 3 layers are difficult to differentiate. **b.** Close-up view. The poly-crystalline nature of the films is apparent at such a scale. **c.** Corner image shows that the sputtering process is omnidirectionally coating the sample.

Next, we change the substrate from silicon to Tm:YGG. Due to the dielectric nature of garnets, the deposition rates of both materials slowed compared to deposition on silicon shown above. After tuning, by adjusting the sputtering time, the deposition parameters shown in Table 5.1 create a recipe for a structure matching the periodicity on silicon.

Material	SiO_2	Si_3N_4
Deposition Time	940 Sec	1140 Sec
Chamber Pressure	4.0×10^{-7} mbar	4.0×10^{-7} mbar
Process Pressure	8 μBar	8 μBar
Ar Gas Flow	20 sccm	20 sccm
RF Power	150 W	150 W
Bias Voltage	65 V	215 V
Expected Thickness	135 nm	105 nm

Table 5.1: Deposition parameters for SiO_2 and Si_3N_4 on YGG. Changes of roughly 1% to the deposition parameters are made actively during deposition to maintain the correct layer thicknesses for slight changes to the sputtering machine voltages. The sample is held upright in a metal mount to get a homogeneous deposition rate on the desired surface. Poorly constructed or lossy films were removed with hydro-fluoric (HF) acid.

5.6.3. MIRROR SPECTRUM

Using the ellipsometer as earlier in this chapter, we measure the transmission spectrum of the layer stack on Tm:YGG at different steps of the mirror deposition process. Deposition parameters, Table 5.1, were chosen to create reflection matching the Tm ion absorption line visible in the top most curve. As more periods of the Bragg grating are added the transmission over the indicated region decreases towards zero as reflection increases. By adjusting the number of layers, we create mirrors of differing reflectivity to meet the desired impedance matching condition for our AFC quantum memory. In this way, we create monolithic devices that possess potential for improved storage efficiency in Tm:YGG.

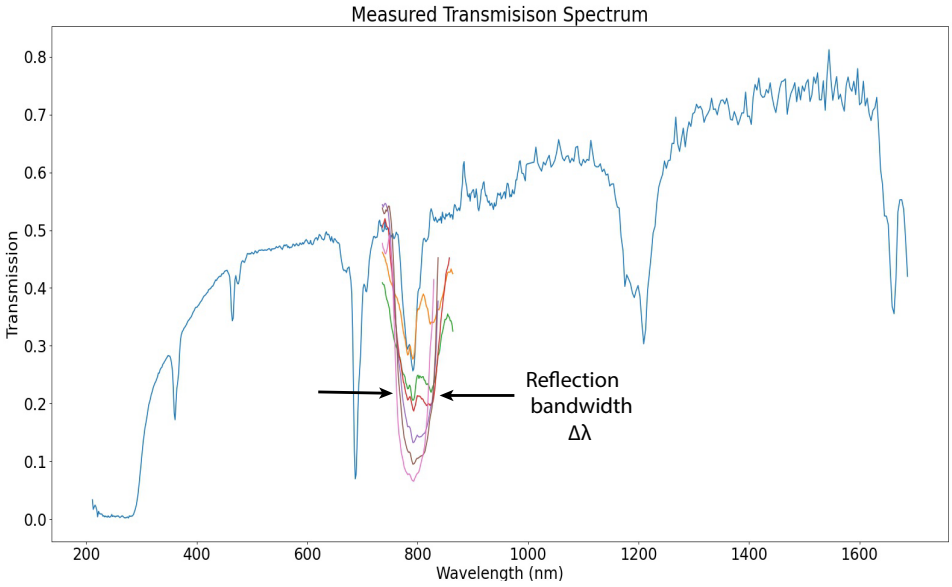

Figure 5.6: The topmost curve in blue shows the transmission through a bare YGG crystal. The absorption lines uniquely identify the dopant ions as Tm, as earlier in the chapter. Each of the following segments shows the change to the transmission profile after adding a single period of quarter wave stack to the front face of the crystal. Orange(2 periods, 4 layers), Green (3 periods, 6 layers), Red (4 periods 8 layers), Purple (5 periods 10 layers), Brown (6 periods 12 layers), Pink (7 periods 14 layers). As more periods are added, the reflection over the indicated bandwidth increases bringing transmission towards zero.

BIBLIOGRAPHY

[1] M. Sabooni, Q. Li, S. Kröll, and L. Rippe, "Efficient quantum memory using a weakly absorbing sample", Phys. Rev. Lett. **110**, 133604 (2013).

[2] P. Jobez, I. Usmani, N. Timoney, C. Laplane, N. Gisin, and M. Afzelius, "Cavity-enhanced storage in an optical spin-wave memory", **16**, 083005 (2014).

[3] J. H. Davidson, P. Lefebvre, J. Zhang, D. Oblak, and W. Tittel, "Improved light-matter interaction for storage of quantum states of light in a thulium-doped crystal cavity", Phys. Rev. A **101**, 042333 (2020).

[4] S. Duranti, S. Wengerowski, A. Seri, B. Casabone, and H. de Riedmatten, "Cavity assisted highly efficient afc optical memory in pr^{3+}:y_2sio_5", in Qia consortium meering (2021).

[5] R. A. Akhmedzhanov, L. A. Gushchin, A. A. Kalachev, N. A. Nizov, V. A. Nizov, D. A. Sobgayda, and I. V. Zelensky, "Cavity-assisted atomic frequency comb memory in an isotopically pure $^{143}nd^{3+}$:ylif4 crystal", **13**, 115203 (2016).

[6] J. H. Burnett, S. G. Kaplan, E. L. Shirley, D. Horowitz, W. Clauss, A. Grenville, and C. V. Peski, "High-index optical materials for 193nm immersion lithography", in Optical microlithography xix, Vol. 6154, edited by D. G. Flagello (International Society for Optics and Photonics, 2006), pp. 445–456.

[7] T. Fan, G. Huber, R. Byer, and P. Mitzscherlich, "Spectroscopy and diode laser-pumped operation of tm,ho:yag", IEEE Journal of Quantum Electronics **24**, 924–933 (1988).

[8] M. Ross, P. Freedman, J. Abernathy, G. Matassov, J. Wolf, and J. Barry, "Space optical communications with the nd: yag laser", Proceedings of the IEEE **66**, 319–344 (1978).

[9] R. Powell, *Physics of solid-state laser materials*, Atomic, Molecular and Optical Physics Series (Springer New York, 1998).

[10] Y. Zhang et al., "Diode pumped efficient continuous-wave yb:ygg laser", in Cleo: 2011 - laser science to photonic applications (2011), pp. 1–2.

[11] H. Yu, K. Wu, B. Yao, H. Zhang, Z. Wang, J. Wang, X. Zhang, and M. Jiang, "Efficient triwavelength laser with a nd:ygg garnet crystal", Opt. Lett. **35**, 1801–1803 (2010).

[12] S. J. Beecher, J. A. Grant-Jacob, P. Hua, D. P. Shepherd, R. W. Eason, and J. I. Mackenzie, "Er:ygg planar waveguide amplifiers for lidar applications", in Lasers congress 2016 (assl, lsc, lac) (2016), JTh2A.9.

[13] C. W. Thiel, N. Sinclair, W. Tittel, and R. L. Cone, "$Tm^{3+}:Y_3Ga_5O_{12}$ Materials for spectrally multiplexed quantum memories", Phys. Rev. Lett. **113**, 160501 (2014).

[14] C. W. Thiel, N. Sinclair, W. Tittel, and R. L. Cone, "Optical decoherence studies of $Tm^{3+}:Y_3Ga_5O_{12}$", Phys. Rev. B **90**, 214301 (2014).

[15]J. Zhao, L. Ye, Y. Liu, S. Li, G. Fu, and Q. Yue, "Optical properties and surface blistering visualization on multiple-energy he-implanted yb:ygg crystal by annealing treatment", Results in Physics **15**, 102621 (2019).

[16]Y. Lili, L. Yong, L. Shuang, F. Gang, Y. Qingyang, and Z. Jinhua, "Refractive index enhanced well-type waveguide in nd:ygg crystal fabricated by swift kr8+-ion irradiation", Opt. Mater. Express **9**, 1907–1914 (2019).

[17]S. Kurosawa, V. V. Kochurikhin, A. Yamaji, Y. Yokota, H. Kubo, T. Tanimori, and A. Yoshikawa, "Development of a single crystal with a high index of refraction", Nuclear Instruments and Methods in Physics Research Section A: Accelerators, Spectrometers, Detectors and Associated Equipment **732**, Vienna Conference on Instrumentation 2013, 599–602 (2013).

[18]J. A. Grant-Jacob, S. J. Beecher, H. Riris, A. W. Yu, D. P. Shepherd, R. W. Eason, and J. I. Mackenzie, "Dynamic control of refractive index during pulsed-laser-deposited waveguide growth", Opt. Mater. Express **7**, 4073–4081 (2017).

[19]K. Enke and W. Tolksdorf, "Continuously recording refractive index spectrograph for transparent and opaque insulators and semiconductors", Review of Scientific Instruments **49**, 1625–1628 (1978).

[20]F. A. van Melle and H. B. J. Schurink, "I. über die kristallstruktur von pentaerythrit, pentaerythrit-tetraacetat und dibenzalpentaerythrit", Zeitschrift für Kristallographie - Crystalline Materials **69**, 1–16 (1929).

[21]M. Weber, *Handbook of optical materials*, Laser & Optical Science & Technology (CRC Press, 2018).

[22]J. A. Woollam, B. D. Johs, C. M. Herzinger, J. N. Hilfiker, R. A. Synowicki, and C. L. Bungay, "Overview of variable-angle spectroscopic ellipsometry (VASE): I. Basic theory and typical applications", in Optical metrology: a critical review, Vol. 10294, edited by G. A. Al-Jumaily (International Society for Optics and Photonics, 1999), pp. 3–28.

[23]B. Johs, J. A. Woollam, C. M. Herzinger, J. N. Hilfiker, R. A. Synowicki, and C. L. Bungay, "Overview of variable-angle spectroscopic ellipsometry (VASE): II. Advanced applications", in Optical metrology: a critical review, Vol. 10294, edited by G. A. Al-Jumaily (International Society for Optics and Photonics, 1999), pp. 58–87.

[24]A. R. Forouhi and I. Bloomer, "Optical dispersion relations for amorphous semiconductors and amorphous dielectrics", Phys. Rev. B **34**, 7018–7026 (1986).

[25]G. E. Jellison and F. A. Modine, "Parameterization of the optical functions of amorphous materials in the interband region", Applied Physics Letters **69**, 371–373 (1996).

[26]J. W. Weber, T. A. R. Hansen, M. C. M. van de Sanden, and R. Engeln, "B-spline parametrization of the dielectric function applied to spectroscopic ellipsometry on amorphous carbon", Journal of Applied Physics **106**, 123503 (2009).

[27]J. Mohrmann, T. E. Tiwald, J. S. Hale, J. N. Hilfiker, and A. C. Martin, "Application of a b-spline model dielectric function to infrared spectroscopic ellipsometry data analysis", Journal of Vacuum Science & Technology B **38**, 014001 (2020).

[28]J. Hrabovský, M. Kučera, L. Paloušová, L. Bi, and M. Veis, "Optical characterization of y3al5o12 and lu3al5o12 single crystals", Opt. Mater. Express **11**, 1218–1223 (2021).

[29]C. M. Herzinger, B. Johs, W. A. McGahan, J. A. Woollam, and W. Paulson, "Ellipsometric determination of optical constants for silicon and thermally grown silicon dioxide via a multi-sample, multi-wavelength, multi-angle investigation", Journal of Applied Physics **83**, 3323–3336 (1998).

[30]P. Peterka, I. Kasik, A. Dhar, B. Dussardier, and W. Blanc, "Theoretical modeling of fiber laser at 810 nm based on thulium-doped silica fibers with enhanced 3h4 level lifetime", Opt. Express **19**, 2773–2781 (2011).

[31]S. Agger, J. H. Povlsen, and P. Varming, "Single-frequency thulium-doped distributed-feedback fiber laser", Opt. Lett. **29**, 1503–1505 (2004).

[32]V. A. Volkovich, A. B. Ivanov, S. M. Yakimov, D. V. Tsarevskii, O. A. Golovanova, V. V. Sukhikh, and T. R. Griffiths, "Electronic absorption spectra of rare earth (iii) species in nacl–2cscl eutectic based melts", AIP Conference Proceedings **1767**, 020023 (2016).

[33]E. Yablonovitch, "Inhibited spontaneous emission in solid-state physics and electronics", Phys. Rev. Lett. **58**, 2059–2062 (1987).

[34]B. Osting, "Bragg structure and the first spectral gap", Applied Mathematics Letters **25**, 1926–1930 (2012).

[35]P. Yeh and M. Hendry, "Optical waves in layered media", Physics Today **43**, 77 (1990).

[36]R. Kashyap, *Fiber bragg gratings*, Optics and Photonics (Elsevier Science, 2009).

[37]E. Garmire, "Theory of quarter-wave-stack dielectric mirrors used in a thin fabry-perot filter", Appl. Opt. **42**, 5442–5449 (2003).

[38]L. Gao, F. Lemarchand, and M. Lequime, "Refractive index determination of sio2 layer in the uv/vis/nir range: spectrophotometric reverse engineering on single and bi-layer designs", Journal of the European Optical Society - Rapid publications **8** (2013).

[39]H. R. Philipp, "Optical properties of silicon nitride", **120**, 295 (1973).

[40]S. Larouche and L. Martinu, "Openfilters: open-source software for the design, optimization, and synthesis of optical filters", Appl. Opt. **47**, C219–C230 (2008).

[41]P. D. Davidse and L. I. Maissel, "Dielectric thin films through rf sputtering", Journal of Applied Physics **37**, 574–579 (1966).

[42]Q. H. Fan, L. Q. Zhou, and D. Stevenson, "High rate sputtering deposition of silicon oxide thin films from new sio2:si target composition", Journal of Vacuum Science & Technology A **27**, 979–985 (2009).

[43]M. Signore, A. Sytchkova, D. Dimaio, A. Cappello, and A. Rizzo, "Deposition of silicon nitride thin films by rf magnetron sputtering: a material and growth process study", Optical Materials **34**, 632–638 (2012).

6

MEASUREMENT OF THE THULIUM ION SPIN HAMILTONIAN IN A YTTRIUM GALLIUM GARNET HOST CRYSTAL

Jacob H. Davidson, Philip J. T. Woodburn, Aaron D. Marsh, Kyle J. Olson, Adam Olivera, Antariksha Das, Mohsen Falamarzi Askarani, Wolfgang Tittel, Rufus L. Cone, and Charles W. Thiel

You have to have the right sort of stone.
Peridot for mothers, girasol for lovers, sapphire for sadness, and garnet for joy.

Catherynne M Valente

We characterize the magnetic properties for thulium ion energy levels in the $Y_3Ga_5O_{12}$ (Tm:YGG) lattice with the goal to improve decoherence and reduce line-width broadening caused by local host spins and crystal imperfections. More precisely, we measure hyperfine tensors for the lowest level of the $^3H_6$, and excited $^3H_4$ states using a combination of spectral hole burning, absorption spectroscopy, and optically detected nuclear magnetic resonance. By rotating the sample through a series of angles with an applied external magnetic field, we measure and analyze the orientation dependence of the Tm^{3+} ion's spin-Hamiltonian. Using this spin-Hamiltonian, we propose a set of orientations to improve

Parts of this chapter, marked with a *, have been published in Physical Review B **104**, 134103 (2021) [1].

material properties that are important for light-matter interaction and quantum information applications. Our results yield several important external field directions: some to extend optical coherence times, another to improve spin inhomogeneous broadening, and yet another that maximizes mixing of the spin states for specific sets of ions, which allows improving optical pumping and creation of lambda systems in this material.

6.1. PREAMBLE

Creating good AFC quantum memories relies on knowledge of a number of material parameters including but not limited to ground state splittings, spin level lifetimes, excited state splittings, hole/anti hole structure for a given magnetic field, orientation of the magnetic and optical dipole moments for all involved atoms, and even site orientations throughout the crystal. Some of the shortcomings in chapter 4 are direct results of creating memories without knowledge of some of these important parameters.

The work described in this chapter confirms long suspected crystal structure assumptions about the locations of Tm ions in the YGG lattice. Additionally it supplies the key information about level splittings that allows us to address single classes of ions that experience the same electro-magnetic environment in future. Finally, knowledge of interesting orientations for clock transition, and branching ratio will inform future choices for purchasing boules and cuts of this crystal for further investigation.

6.2. INTRODUCTION*

RARE-earth-ion-doped crystals (REIC) have long been studied for use in high frequency quantum and classical signal processing [2, 3]. The transitions of interest are those between states of the $4f^N$ configuration that are weakly permitted due to weak mixing with opposite parity states by the host crystal field. Additionally, these electrons are spatially isolated behind the 5s and 5p shell electrons that are distributed farther from the nucleus. These transitions have shown optical and spin coherence times of up to hundreds of microseconds and minutes, respectively, that enable interesting applications in quantum and classical data processing [4, 5]. This coherence, and the associated applications, are often limited by time-varying electromagnetic fields in the local crystalline environment [6, 7].

Trivalent thulium has received particular interest due to its simple energy level structure, long optical coherence time, and the availability of diode lasers at the 795 nm optical transition wavelength[8, 9]. Of particular interest is Tm^{3+} embedded in Yttrium Gallium Garnet ($Y_3Ga_5O_{12}$, Tm:YGG) for which optical coherence times (T_2) on the order of milliseconds have recently been measured [10, 11]. This ion and host crystal combination is still relatively unexplored compared to Tm:YAG. However, deeper understanding about the crystal dynamics, symmetry, and hyperfine structure has led to huge improvements in spectroscopic properties of optical and microwave transitions in other rare-earth-doped materials. One such example is the possibility of transitions with zero first order Zeeman shifts (ZEFOZ), which may be obtained by controlling the interplay of the measured terms of the ion's effective spin Hamiltonian, that can lead to orders of magnitude increase in spin coherence times [6]. Additionally, an effective spin Hamiltonian approximation can be used to improve and develop new experiments for applications of quantum networking and light matter interaction [12, 13].

In this letter, we present a complete characterization of the hyperfine structure in the ground and excited states of the 795nm optical transition of Tm^{3+} ions. To perform these measurements, we use absorption spectroscopy, spectral hole burning (SHB), and optically detected nuclear magnetic resonance (ODNMR) to isolate, measure, and confirm different terms of the effective spin Hamiltonian. These measurements individually

produce information about the coupled behavior of these levels and the six magnetically equivalent, orientationally in-equivalent sites. Only by cross referencing the spectra from different sets of measurements are we able to decouple the information into the individual orientational behavior of each thulium ion in each individual site for each electronic level. Our results are then confirmed to be in good agreement with initial assumptions about crystalline structure[10] and a pair of independent measurements of the spin Hamiltonian terms using a single crystalline direction of Tm:YGG. This new knowledge allows us to predict the presence of optical clock transitions in this material that may allow extending the optical coherence times for light storage and quantum memory.

This letter is presented in the following order: In Sec.6.3, we give a brief overview of the Hamiltonian of the system and the remaining unknowns to be measured. In Sec.6.4, we describe the general crystal geometry as well as the implications with regard to the Hamiltonian and how to isolate the specific projections of an external field on a specific ion site. Section 6.5 describes the experimental setups used to produce the results. In Secs. 6.6 and 6.7, we describe how we gather spectra from hole burning and ODNMR measurements with different crystal orientations and which hyperfine tensor values stem from the results. Section 6.8 contains details on a pair of independent measurements that confirm these tensor values for a specific orientation of the external field. In Sec. 6.9, we discuss our results in the context of optical clock transitions and we identify a series of field orientations that may lead to improved optical coherence in this material.

6.3. SPIN HAMILTONIAN FOR THE ENHANCED ZEEMAN AND QUADRATIC ZEEMAN EFFECTS *

For a non-Kramers ion contained in a crystal lattice of low symmetry, a six term Hamiltonian is often considered to describe the behavior of the ionic level structure [14, 15].

$$H = (H_{FI} + H_{CF}) + H_{HF} + H_Q + H_{eZ} + H_{nZ} \tag{6.1}$$

The first pair of terms describes the energy structure of a free ion (H_{FI}) coupling to the local crystal field (H_{CF}), which determines the energies of the states differentiated by total electron spin angular momentum that we are interested in for this work. The remaining four terms from contributions of the hyperfine (H_{HF}), quadrupole (H_Q), electronic Zeeman(H_{eZ}) and nuclear Zeeman (H_{nZ}) interactions are treated as small perturbations. The measurements conducted here focus on a specific pair of these electronic levels, specifically the lowest energy crystal field levels of the $^3H_6$ and $^3H_4$ multiplets. Additionally, the only isotope of thulium (^{169}Tm) possesses a nuclear spin of $\frac{1}{2}$ so that there is no nuclear quadrupole splitting and the H_Q term can be ignored [8, 16, 17].

The remaining terms of this Hamiltonian are magnetic in nature, corresponding to the hyperfine, electronic Zeeman, and nuclear Zeeman interactions. By expanding these remaining terms to second order as in Ref[15][16] we arrive at a three term Hamiltonian,

$$H = \boldsymbol{B}\cdot(-g_n\beta_n\mathbb{I} - 2g_J\mu_B A_J\boldsymbol{\Lambda}_J)\cdot\boldsymbol{I} - g_J^2\mu_B^2\boldsymbol{B}\cdot\boldsymbol{\Lambda}_J\cdot\boldsymbol{B} \tag{6.2}$$

where g_n is the nuclear gyro-magnetic ratio of thulium, β_n is the nuclear magneton, g_J

is electronic g factor for each level, μ_B is the Bohr magneton, A_J is the hyperfine interaction constant, $\boldsymbol{I}$ the ion's nuclear spin, $\boldsymbol{B}$ the applied external field, and, finally, $\boldsymbol{\Lambda}_J$ the hyperfine tensor. This tensor is given by second order perturbation theory as

$$\Lambda_{J,(\alpha,\beta)} = \sum_{n\neq 0} \frac{\langle 0|J_\alpha|n\rangle\langle n|J_\beta|0\rangle}{E_n - E_0}, \qquad \alpha,\beta \in \{x,y,z\} \tag{6.3}$$

where $\langle 0|J_\alpha|n\rangle, \langle n|J_\beta|0\rangle$ are wave-function matrix elements for the electronic levels of interest, and the sum is over the crystal field levels with energies E_n [8, 16, 17].

The first two terms in Eq.6.2 describe the enhanced effective nuclear Zeeman effect that results from the second order coupling of the hyperfine interaction between the electronic Zeeman effect and the first order nuclear Zeeman interaction. The third term is the quadratic Zeeman effect that results from the expansion of the electronic Zeeman term where the orientation dependence is again determined by a scaled version of the same hyperfine tensor, $\boldsymbol{\Lambda}$ [18]. Other terms that arise from the expansion to second order are small and neglected. With this description in place, the only unknowns in Eq.6.2 are the 18 matrix elements of the hyper-fine tensors $\boldsymbol{\Lambda_{g,e}}$, with each a 3x3 matrix that describes the magnetic interactions of these levels for Tm^{3+} ions in this material. The level structure with an applied magnetic field is shown in Fig. 6.2 a. The effect of the quadratic term can be seen as a shift of the whole electronic crystal field level, and the linear term (6.2 a.**Inset**) splits the pair of nuclear spin states. The number of unknown elements in this tensor drops further due to the local symmetry of the Tm^{3+} ions that occupy yttrium in the YGG lattice.

6.4. CRYSTAL SYMMETRY AND SITE SELECTION *

The location and symmetry of the yttrium sites is well understood for garnet crystals[4, 19, 20]. YGG is a cubic crystal with space group symmetry O_h^{10}, and the thulium sites feature D_2 point group symmetry[10]. The site symmetry, as described for the similar case of Tm:YAG[21] and depicted in Fig. 7.2, allows for six crystallographically equivalent yet orientationally in-equivalent substitution sites.

The magnetic behavior of Tm^{3+} in each of these sites is the same, due to the ion being locally surrounded by the same structural and chemical environment. However, the ion and its local environment occurs with six different orientations with respect to the cubic crystal cells of the garnet, leading to orientational, and in essence magnetic, in-equivalence between the sites. Here, as in Ref.[20][21] and Fig 7.2, there are specific directions with respect to the cubic crystal axes that cast different subsets of the orientationally in-equivalent sites into classes of ions that share the same projections of applied electromagnetic fields ($\vec{\boldsymbol{E}}, \vec{\boldsymbol{B}}$) onto the local Tm^{3+} site axes. For fields ($\vec{\boldsymbol{E}}, \vec{\boldsymbol{B}}$) directed along the crystalline <111> and <001> sets of directions (<110>,< $\bar{1}\bar{1}2$ > and <100>,<010> respectively) . These symmetric directions serve as a labeling convention for growth, dicing, and orientation of these crystals and are built into the models detailed below, which allows us to determine the relative projection of incident fields on each of the Tm^{3+} ion sites throughout our experiments.

On a more microscopic level, the local D_2 symmetry for each site is such that, by using a set of axes around the Tm^{3+} ion defined by that site symmetry, we can diagonalize the hyperfine tensor from Sec. 6.3. This leaves only the six diagonal elements,

$\Lambda_{J,(x,y,z)}$ (three for each electronic state J), which correspond to the tensor elements along the three axes shown in Fig.7.2 for "Site 1" of the six sites. Considering the crystal symmetry, the entire enhanced effective Zeeman term of Eqn. 6.2 for a given electronic level can be simplified to [8, 17]

$$H_{J,(x,y,z)} = -\hbar\sqrt{g_{J,x}^2 B_x^2 + g_{J,y}^2 B_y^2 + g_{J,z}^2 B_z^2}\cdot \boldsymbol{I} \tag{6.4}$$

for

$$g_{J,(x,y,z)} = -g_n\beta_n - 2g_J\mu_B A_J \Lambda_{J,(x,y,z)}. \tag{6.5}$$

The determination of the six remaining parameters (three per electronic level) will be discussed in later sections.

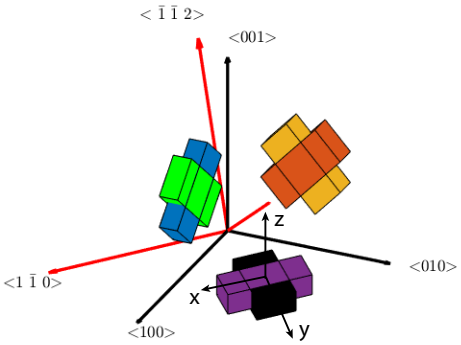

Figure 6.1: Possible sites of Tm^{3+} ions in a YGG crystal. Black thick axes denote the cubic unit cell boundaries. Each of the 6 colored cuboids denotes the location as well as the direction of the ion's local Y-axis (along the cuboids largest dimension),that is also expected to be the direction of the optical transition dipole moment of the thulium transition, relative to a cubic crystal cell. Each site is identified by a specific color throughout the remainder of this letter: "Site 1" (Black), "Site 2" (Purple), "Site 3" (Orange), "Site 4" (Yellow), "Site 5" (Green), "Site 6" (Blue). Red axes denote the symmetry axes along which the crystal is grown and oriented for these studies. Throughout this letter we will characterize rotations with respect to these directions $<1\bar{1}0>, <111>, <\bar{1}\bar{1}2>$. Finally, the labeled (x,y,z) thin black axes denote the local site axes as defined by the D_2 point group symmetry(shown for the example of Site 1).

To measure these parameters, we gather data on the splittings of the ground and excited hyperfine states for a series of different orientations of a Tm:YGG crystal sample. In spherical coordinates, each specific orientation (θ,ϕ) relative to the cubic crystal cell shown in Fig.7.2 has a fixed set of projections on each of the 6 potential Tm^{3+} ion site axes. Thus, for every angle of the magnetic field with a macroscopic, oriented sample, we can determine from the expected geometry the exact magnetic projection on each Tm^{3+} ion axis. By matching sets of these magnetic field projections to various measurements of the hyperfine splitting we determine the desired hyperfine tensor values.

6.5. EXPERIMENTAL SETUP *

To gather the data for our study, we used a total of five Tm:YGG crystals, each one cut along the symmetric dimensions of the cubic crystal cell. In addition, we employed several experimental setups. While similar in concept (Laser → Pulsing → Frequency

Control → Cold Crystal in a magnetic field → Detector), they featured technological differences. For example, we used different cryogenic systems –two helium flow cryostats reaching a base temperature of <2K, equipped with magnets that allow applying fields of up to 7 T and fitted with a gearing system that allows rotating the cooled sample by up to 360 degrees around a fixed optical axis for each crystal sample; and an adiabatic demagnetization refrigerator reaching 500 mK temperature, equipped with a 2T magnet as well as a static crystal holder.

To address the center of the inhomogeneously broadened $^3H_6 \Leftrightarrow {}^3H_4$ optical transition of thulium at 795.325 nm wavelength, we used either a titanium sapphire laser or an external cavity diode laser. The light was subsequently directed through an acousto-optic modulator (AOM), which allowed creating pulses out of the continuous-wave laser light. Additionally, we used either an AOM in double-pass configuration, or a phase modulator driven by a serrodyne signal, to frequency modulate the light. The appropriately prepared pulses were then directed to the cooled Tm:YGG samples either by free space or by using a single-mode optical fiber. The beam diameter inside the samples were around 500 μm in case of the flow cryostat and free-space coupling, and around 200 μm in the other case. Finally, the light was sent into a photodetector, and the electrical signals were displayed on an oscilloscope and recorded for analysis.

The set of ODNMR experiments detailed in section 6.7 also required the application of radio-frequency signals that vary between 20kHz and 10 MHz. Towards this end, one of the flow cryostats is equipped with an impedance matched copper coil that provides an adjustable frequency RF field around the crystal sample. This coil is driven using 5-10 W RF power, created by means of a RF signal generator, a pair of 40dB amplifiers, as well as variable attenuation. For each frequency, the output from the signal generator was set to the desired value and mixed with RF noise, low passed to 100kHz before being sent to the coil, and terminated to 50Ω. The added noise increases the RF tone bandwidth to provide an RF field capable of driving a larger population of spins, and in turn create signals with higher SNR.

Additional information about the experimental setups will be given in Sections 6.6, 6.7, & 6.8 along with the description of the measurements.

6.6. SPECTRAL HOLE BURNING DESCRIPTION AND RESULTS *

The six unknown tensor values appear in both the linear and quadratic terms of the Hamiltonian such that measurements of either term's orientation dependence is sufficient to determine the entire spin-Hamiltonian. The linear splitting of hyperfine levels the ground and excited states can be observed through spectral hole burning measurements [14]. With a magnetic field applied, both the ground and excited electronic states split into spin up $+\frac{1}{2}$, ($|\uparrow\rangle$) and spin down $-\frac{1}{2}$, ($|\downarrow\rangle$) states, creating a pair of levels seen in Fig.6.2 a. (Inset). Even at cryogenic temperatures, both ground-state spin states are equally populated. Spectral hole burning drives atomic population through this level structure, resulting in long lasting population differences between the different spin states[9]. The details of this optical pumping mechanism are well understood and are detailed in Ref.[21,22][22, 23]. The initial pump pulse creates the main spectral hole: a reduction of the atomic absorption of the ensemble at the chosen pulse frequency within the in-homogeneous broadening of the crystal.

Considering only a single projection of the magnetic field on a site, ions in the selected bandwidth are pumped to the other ground-state hyperfine level and thereby create a feature with increased absorption, referred to as an anti-hole, at a frequency offset given by the ground-state splitting, Δ_g. Due to the inhomogeneously broadened nature of the transition, additional anti-holes and a single side hole arise symmetrically around the main hole at frequency offsets of $(\Delta_g \pm \Delta_e)$ and Δ_e, respectively. By frequency sweeping weak laser light over the spectral region surrounding the main hole and recording the transmitted intensity, these population differences are visible as shown in Fig.6.2 b. By measuring the frequency offset of side and anti-holes for a set of different orientations we can determine the hyperfine tensor in Eq.6.2.

For an arbitrary orientation, each site has a different projection of the external field on its local axes. Thus, based on that projection, it is possible that that the same spectral feature(e.g. the first anti-hole at Δg - Δe) from separate sites may be visible at different frequencies. In the worst case, this could result in crowded spectra that contain as many as 48 features that would need to be assigned to different sites and associated external field projections. Fortunately, due to the fixed orientations of the sites with respect to the symmetric crystal axes, some orientations cast sites into equivalent subsets, making their spectral features appear at the same frequencies. This is the case in Fig.6.2 b. where the visible features belong to three different sites 1, 3, and 5 that all share the same field projection. However, for a different case of Figure 6.2 c, the visible features show only the (Δg -Δe) anti-holes for a pair of Tm^{3+} sites with different magnetic field projections. Thus, with hole spectra from a series of different orientations, the problem then becomes interpreting each spectrum and making an assignment for each feature to a particular site and its corresponding external field projection. This process provides us with a set of splittings that can be used to determine the the tensor values for a given site at a given orientation.

This experiment was conducted in one of the flow cryostats described in Sec.6.4. The Tm:YGG sample was cooled to 2K and a fixed field of 300mT was applied as the sample was rotated through a series of angles. To create a hole spectrum, the experimental burning sequence at each angle involved a 1ms hole burning pulse, a waiting period of 10 ms for population to decay from the excited state, and finally a 100μs read pulse with a frequency chirped over a 40MHz region centered at the main hole to reveal any side and anti-hole structure. This sequence used circularly polarized light with ~10mW of power incident on the crystal and was averaged over dozens of scans to produce a single spectrum at each angle. Due to a combination of pump laser linewidth, sample temperature, and limited AOM frequency shifting efficiency, we were only able to monitor and record the frequency change of the first anti-hole, occurring at a frequency offset of (Δ_g -Δ_e), for all sites during these rotational SHB measurements.

Though not a direct measurement of the tensor values of either the ground or excited state, these values contain information that in conjunction, with the ODNMR data from Section 6.6, is used to compute the spin-Hamiltonian. Tracking these splittings through the series of different angles between an external magnetic field and the symmetric crystal axes, we define a "difference tensor" that best satisfies the measured (Δ_g -Δ_e) splittings for all sites at all angles.

More specifically, for a specific angle of external field with respect to a particular crys-

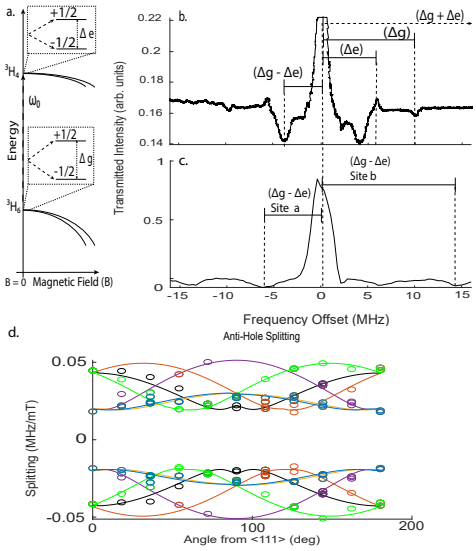

Figure 6.2: **a.** Diagram of the level structure for the optical transition in $^{169}Tm^{3+}$ with increasing magnetic field. Note that on a large scale, the change in energy of all the states is dominated by the quadratic term, but for small fields it is linear. **b.** A detailed serrodyne scan of a spectral hole structure measured for a magnetic field of 90 mT applied along the crystalline <111> axis. The small spectral feature at ~2 MHz likely arises from the only other set of sites for this orientation. **c**. Double passed AOM frequency scan of a broader spectral hole at 300mT. Only $\Delta_g - \Delta_e$ anti-holes are visible for a pair of differently oriented sites. **d**. Markers show the anti-hole frequencies plotted vs the angle between the external magnetic field and the crystal's <111> axis. Solid lines of each color are fits of a "difference" tensor to each of the six potential sites for the ions with a correlation coefficient $R^2 > 90\%$.

tal direction, there is a known projection of the magnetic field on each of the six sites. Our fitting procedure fits $g_{(x,y,z)}$ values in Eq.6.4 to a particular splitting that is assigned to a site and determines the three associated magnetic field projections (B_x, B_y, B_z) at each angle. Thus, one set of fitted values match an entire matrix of magnetic projections for a series of angles with regard to each site to a set of splitting values assigned to each site. The spectral locations of the visible anti-holes at the series of angles compared to the results of this least squares tensor fitting procedure can be seen in Fig.6.2d. This fitting procedure and analysis were repeated for two differently oriented Tm:YGG crystals, and good agreement was found between the resulting "difference tensors". For more information regarding the fitting procedure, and plots of the fit for the second crystalline direction, consult the supplementary material **??**.

6.7. ODNMR MEASUREMENT AND RESULTS *

In addition to SHB, where optical pumping drives changes in hyperfine level population by way of the optical excitation to the excited state followed by spontaneous relaxation, it is also possible to alter the relative hyperfine level populations by directly addressing the microwave transition between them. The relative population between the hyperfine levels can then be observed optically in a double resonance experiment known as opti-

cally detected nuclear magnetic resonance, which has been carried out with a number of REICs [14, 24, 25]. As opposed to SHB, ODNMR provides information directly about either Δ_g or Δ_e and thereby supplements the results in the previous section to extract the Hamiltonian in Eq.6.2. This approach, shown in Fig. 6.3a, involves first creating a population difference between the hyperfine levels via SHB. While viewing this hole profile optically, an RF pulse is applied that, if resonant with the spin transition at frequency Δ_g, partially re-equalibrates the population, resulting in a change of the absorption depth of the spectral hole. Since the energy difference between hyperfine states is unknown for a given external magnetic field the RF field is swept across a range of frequencies to find the resonance condition $\omega_{RF} = \Delta_g$. The excited state splitting Δ_e can be measured with a similar approach using an altered sequence of optical and RF excitation pulses such that population can be addressed and probed while in the excited state.

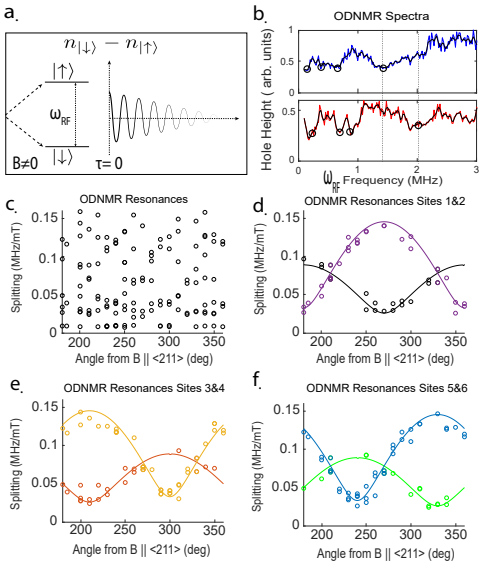

Figure 6.3: **a.** Diagrammatic view of the ODNMR experiment, including the driven spin transition that appears at small magnetic fields, and the coherent RF drive that equalizes the population between the $\pm\frac{1}{2}$ spin states. **b.** The ω_{RF} frequencies that diminish the height of a spectral hole are identified as resonances by a smoothing and peak finding algorithm and then confirmed manually. The top trace shows these resonances with an applied external field of 22.4mT, while the lower trace and dotted lines show the shift of a marked feature for an increased field of 31.4mT. A spectrum similar to these, each with unique resonance frequencies, is generated for many angles of the external field relative to the crystal orientation. **c**. A plot of resonances from all spectra at a series of angles between external field and the crystal < 211 > direction. **d,e,f** Site by site fitting of the tensors listed in 6.1 to the resonances from **c** across a series of angles.

This experiment was carried out in one of the helium flow cryostats, equipped with an RF coil on a rotation mount to apply the RF fields. The Tm:YGG sample is cooled to 2K and an external magnetic field of 20-40mT is applied perpendicular to the optical and rotational axis along the crystalline <211> direction. Using an altered SHB experimental sequence a spectral hole is prepared and read out, with burning and waiting times ad-

justed to ensure minimal contribution to the spectral hole depth from atomic population in the excited states while maximizing the repetition rate. Additionally, the duration and relative powers of the burn and read pulses were adjusted to produce a slightly shallower hole that could be read with less noise caused by laser power fluctuations.

While repeating the hole burning experiment, 100 ms long RF pulses are applied to the crystal. We tuned the frequency of the RF field in 20 kHz steps from 100kHz-4 MHz and five repetitions are averaged to produce spectra as seen in Fig.6.3 b. The broadening of the features is due to the convolution of the applied RF field linewidth of 100kHz and the RF resonance in-homogeneous linewidth. To ensure that these features showed the ground-state resonances, we first confirmed that each resonance frequency had a linear shift with increasing external magnetic field, and were absent when no external field was applied. We optimized the generation of the ODNMR spectra over the parameter space of RF drive power, optical hole burning power, duration, sample temperature, SHB duty cycle, and experimental repetition rate to produce the best signal to noise ratio for these resonance scans.

This experiment was repeated for a series of different angles between the crystal <211> axis and the externally applied magnetic field. All resonance frequencies were determined with help of a peak finding algorithm, and are displayed in Fig. 6.3 c. As before, all six Tm sites contribute to this set of resonances.

Here again, each specific angle of external field with respect to a particular crystalline direction defines six projections of the magnetic field on each site. Each angle is associated with a series of ODNMR resonances as well, such that a vector of ground state tensor values must solve, as closely as possible, a matrix equation that includes magnetic projections on each site for many local angles, to fit over more than 200 equally weighted resonance points. The resulting tensor fits are shown in Fig. 6.3 d,e,f. Site assignment and fitting was repeated for two differently oriented Tm:YGG crystals that show good agreement with one another. The results of the second fit can be seen in the supplementary material 6.11. It is interesting to note that the calculated tensor values are comparable to those measured with TmGG [26]. This gives us additional confidence in the results, as in the case of the confirmation between Tm:YAG and TmAG [23, 27].

This fitting procedure produces the three ground state tensor values $\Lambda_{g,(x,y,z)}$, and in conjunction with the “difference tensor" fits from the previous section, $\Lambda_{e,(x,y,z)}$ can also be determined. These results for the six spin-Hamiltonian components averaged over the four directional fits of sections 6.6 & 6.7 are shown in Table 6.1, where the signs are given by convention. Unfortunately, both spectral hole burning and ODNMR yield only the magnitude but not the sign of the different parameters because we cannot differentiate one hyperfine state from another. Nonetheless, and similarly to Ref.[28][28], for our purposes it is often enough to know the relative energy difference between the two hyperfine states of each electronic level, and not whether it happens to be the spin up or spin down state since their energy shifts will be symmetric.

	$^3H_6$(g)	$^3H_4$(e)
$g_n\beta_n$	-3.53(MHz/T)	-3.53(MHz/T) [27]
g_j	1.16	0.8
A_J	-470.3(MHz)	-678.3(MHz)
$A_J\Lambda_x$	-7.23 $\times 10^{-4}$	-1.55 $\times 10^{-4}$
$A_J\Lambda_y$	-4.47 $\times 10^{-3}$	-3.95 $\times 10^{-3}$
$A_J\Lambda_z$	-9.99 $\times 10^{-4}$	-5.57 $\times 10^{-4}$
g_x	27 ± 1.7 (MHz/T)	7 ± 2.5 (MHz/T)
g_y	146 ± 1.5(MHz/T)	92 ± 2.8 (MHz/T)
g_z	36 ± 2.6 (MHz/T)	16 ± 3.1 (MHz/T)

Table 6.1: Spin Hamiltonian values. The g_j values are calculated using the general formalism described in Ref.[14][15]. The A_J values are from Ref.[7][8] and can be recalculated from Ref.[14][15] as they depend only on the expectation value for electron radius for this Tm^{3+} transition. The $g_{x,y,z}$ values for the excited and ground states are measured in this work. Together with the listed constants, they allow calculating all $\Lambda_{J,\alpha}$ values using Eq.6.5.

6.8. VERIFICATION OF RESULTS *

In the following, we detail additional measurements based on alternative methods and on different Tm:YGG crystals. While being performed with a reduced set of parameters that does not allow independently establishing the Hamiltonian in Eq. 6.2, they nevertheless allow verifying the results presented in section 6.7.

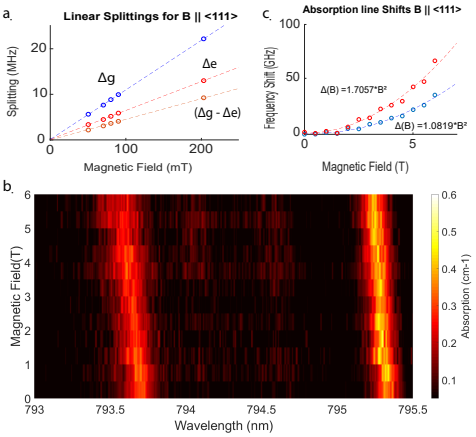

Figure 6.4: **a.** The linear splitting of the anti-holes shown in Fig.6.2 b. for the B || <111> orientation yields values of 45 and 108± 2 MHz/T and a side hole splitting of 63± 2 MHz/T. **b.** Absolute absorption frequency for the optical transitions from the lowest ground state crystal field level to the first (795.325 nm) and second(793.7nm) excited state crystal field levels with increasing magnetic field. **c.** A closer look at the behavior of these transitions reveals the expected quadratic nature of the frequency shift.

6.8.1. LINEAR ZEEMAN SHIFT

The enhanced effective Zeeman interaction given by the first two terms of Eq.(6.2) results in a linear splitting of the hyperfine levels in both the ground and excited states. As discussed in section 6.5, the Zeeman coefficient can be measured by first applying a magnetic field, then exposing the sample to narrow-band laser light, and finally probing the resulting sequence of holes and anti-holes by frequency scanning a weak laser across the created spectral features.

This experiment was performed inside the ADR and at a temperature of 500 mK. In this case, the magnetic field could only be applied along the crystal's <111> direction, resulting in magnetic projections of equal magnitude on the Y and Z components of sites 1,3, and 5, and the X and Z components of sites 2,4, and 6. The holeburning laser was frequency locked to around 10 kHz linewidth by means of a stable optical reference cavity and the Pound-Drever-Hall method, and we employed 1 mW of power incident on the crystal, burning pulses of 200ms duration, 10ms of waiting time to avoid spontaneously emitted signal, and a 1ms long read pulse. The lower temperature and narrower laser linewidth (compared to the measurements described before) allowed resolving all expected SHB features, including a pair of anti holes and a side hole, as seen in Fig. 6.2 b. for a field of 90 mT.

The splitting of these spectral features as a function of magnetic field shown in Fig.6.4 a. confirms the linear nature of the Zeeman interaction with splittings of the ground and excited states of 108 ± 2 MHz/T and 63 ± 2 MHz/T, respectively. This is in good agreement with the values calculated from the measured tensors, which we found to be $\Delta_g = 106 \pm 2.2$ MHz/T, $\Delta_e = 66 \pm 1.3$ MHz/T for sites 1,3, and 5 at this orientation.

6.8.2. QUADRATIC ZEEMAN SHIFT

The quadratic Zeeman interaction given by the third term of Eq.(6.2) shifts each electronic crystal field level, characterized by the total angular momentum J, parabolically due to the so-called VanVleck paramagnetism [29]. Each crystal field level shifts with its own rate, as depicted in Fig.6.2 a. and described by its hyperfine tensor. This creates an overall shift of the optical transition frequency with a B^2 dependence that varies based on the external field direction. It can be calculated using the ground-state and excited-state tensor values given in Table 6.1.

To measure the quadratic Zeeman effect, we used a flow cryostat operating at 5K with an applied magnetic field along the <111> direction of the Tm:YGG crystal. We performed white light absorption spectroscopy, similar to Ref.[16][17], i.e. we directed collimated CW white light through the crystal and to an optical spectrum analyzer to observe the entire inhomogeneous line of the $^3H_6 \Leftrightarrow ^3H_4$ transition at 795.325nm (see Fig.6.4b). The optical transition from lowest crystal field level of the ground state to the second crystal field level of the excited state at 793.7 nm was visible as well, confirming the expected crystal field spacing of 26 cm^{-1} in Ref.[3][4]. We monitored the absorption frequencies for this pair of transitions as the external magnetic field was increased from 0 to 6 T. The results are depicted in Fig. 6.4 c. A quadratic fit yields a frequency shift of $\Delta = 1.08 \pm 0.24$ GHz/T^2, which is in good agreement with the value of $\Delta_p = 1.09 \pm 0.25$ GHz/T^2 that we calculated from the measured hyperfine tensors.

6.9. OPTICAL CLOCK TRANSITIONS AND SPECIAL DIRECTIONS *

The frequency of the transition between two hyperfine states–one belonging to the electronic ground state and one of the excited state–depends on the applied magnetic field through the linear and quadratic Zeeman effects. Small field fluctuations therefore cause spectral diffusion and hence a reduction of the optical coherence time. It is sometimes possible to choose a magnetic field magnitude and a crystal orientation for which the transition energy becomes, to first order, insensitive to fluctuations in the magnetic field. These transitions are referred to as optical clock transition and are analogous to the ZEFOZ transitions from Ref.[5,28,30,31] [6, 28, 30, 31]. Clock transitions are extremely powerful tools used for reducing decoherence due to noisy magnetic fields [32]. These clock transitions exist in Tm:YGG and can be found for a particular site using the procedure detailed below.

Inspecting the third term of Eq. 6.2 and taking into account that the elements of the hyperfine tensor Γ_J are larger in the ground state than in the excited state (see Ref.[16][17] for a detailed explanation in Tm:YAG) the optical transition energy change caused by the quadratic Zeeman effect creates an increase in transition energy with magnetic field. This is depicted theoretically in Fig.6.2 a. and confirmed from the data in Fig. 6.4b.

Furthermore, looking at the first and second term of Eq. 6.2, which describe the linear Zeeman shift, we find that there exist ground and excited state pairs of hyperfine states for which the optical transition frequency decreases with applied magnetic field. Hence, for certain combinations of crystal orientation (or rather orientation of a local Tm^{3+} site) with respect to the magnetic field, magnetic field strength and spin values, the linear and quadratic Zeeman effects oppose each other, and an optical clock transition can be observed [33]. This transition must have a field magnitude insensitive point, which is shown in Fig. 6.5 a as the shift in optical transition frequency $\Delta E_{opt}(|B|,\theta,\phi)$ vs. applied field magnitude.

In these cases, the spin-Hamiltonian terms form a quadratic function that must have an extremum, i.e. a field-magnitude-insensitive point, at some positive field magnitude. The first condition of an optical clock transition, a field magnitude $|\boldsymbol{B}|$ such that $\frac{\partial \Delta E_{opt}}{\partial |\vec{\boldsymbol{B}}|} = 0$, is calculated for every orientation of magnetic field relative to the "Site 1" spin -1/2 conserving optical transition in Fig. 6.5 b using a mesh size of 1mT and 1 degree angular steps.

For the remaining angular derivatives ($\frac{\partial \Delta E_{opt}}{\partial B_\theta}, \frac{\partial \Delta E_{opt}}{\partial B_\phi} = 0$), there must also be angles for which ΔE_{opt} is also insensitive to first order angular change to complete each optical clock transition. Though all orientations have some field magnitude that results in an invariant point, only some orientations have angular gradients that simultaneously go to zero. Plotted in Fig. 6.5c is the magnitude of the angular gradient for both spin conserving optical transitions vs the optical transition frequency for all angles of magnetic field with respect to the crystal axes. Two angular points stand out, one for each spin conserving transition, whose gradient value becomes exceedingly small. By cross referencing the points of small angular gradient with the field at which the magnitude extrema appears, we can find an orientation that simultaneously brings all three derivatives to zero. In the case of the spin -1/2 conserving optical transition for "Site 1", we

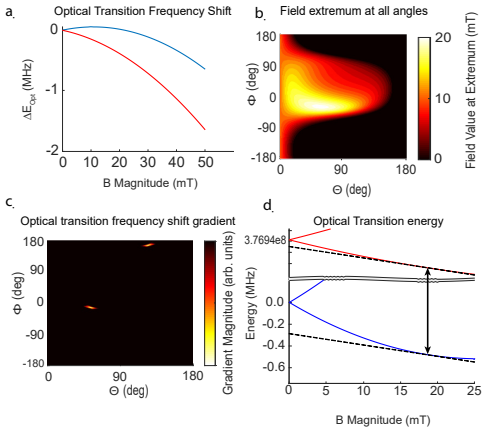

Figure 6.5: **a.** The shift in the optical transition frequency follows a quadratic dependence with an extrema that, for every orientation, appears at a positive field for the spin conserving -1/2 ⇔ -1/2 transition (blue) and at some negative field for the spin conserving +1/2 ⇔ +1/2 transitions (red). **b.** For the -1/2 ⇔ -1/2 spin conserving optical transition and for all angles, the magnetic field value of this extrema is identified. **c.** Angular gradient of the optical transition frequency at a field of 19mT. Two points are visible for which the angular gradient approaches zero. **d.** Energy shifts of the two -1/2 spin states at this particular direction vs. magnetic field magnitude. At 19mT, the slope of the energy change for both states with change in field magnitude is equal (along with the other derivatives) and an optical clock transition occurs.

arrive at a set of coordinates $\vec{\boldsymbol{B}}_{|\boldsymbol{B}|,\boldsymbol{\theta},\boldsymbol{\phi}} = (19mT, 55^o, -15^o)$ that correspond to an optical clock transition. The invariant energy levels of this transition at this field are shown in Fig. 6.5d. This procedure can be repeated for the remaining sites and potential optical transitions (spin crossing or preserving), giving us the list of optical clock transitions in this material shown in Table 6.2.

Past studies characterize the benefit to coherence gained by using a field invariant direction with the definition of transition curvature given by Ref.[30] [30]. All transitions in Table 6.2 share the same curvature of $\sim 36\text{Hz}/G^2$. Other REIC samples previously brought to invariant points with this magnitude of curvature have resulted in orders of magnitude improvement to spin coherence times. However, the amount of improvement in the case of Tm:YGG will depend heavily on the decoherence mechanisms involved for this optical transition.

Though the clock transition directions are important for maximizing optical coherence time, alternative crystal properties can also be optimized by choosing other external field directions. Following the arguments from Ref.[34] [34], we have found other orientations that are capable of minimizing the spin inhomogeneous broadening for the ground state spin transition. Similarly, according to Ref.[22,35] [23, 35] another orientation exists that allows maximizing the branching ratio of the available lambda system in this material. Details on the calculation of these orientations are available in the supplementary material 6.11.

Site #	$\|\boldsymbol{B}\|$	$\vec{\boldsymbol{B}}_{\boldsymbol{\theta}}$	$\vec{\boldsymbol{B}}_{\boldsymbol{\phi}}$	Spin Level Transition
1	19 mT	55^o	-15^o	-1/2 ⇔ -1/2
1	19 mT	125^o	166^o	+1/2 ⇔ +1/2
1	36 mT	64^o	-150^o	+1/2 ⇔ -1/2
1	36 mT	117^o	31^o	-1/2 ⇔ +1/2
2	19 mT	54^o	76^o	-1/2 ⇔ -1/2
2	19 mT	125^o	-105^o	+1/2 ⇔ +1/2
2	36 mT	116^o	120^o	-1/2 ⇔ +1/2
2	36 mT	63^o	-60^o	+1/2 ⇔ -1/2
3	19 mT	102^o	54^o	-1/2 ⇔ -1/2
3	19 mT	79^o	-127^o	+1/2 ⇔ +1/2
3	36 mT	64^o	120^o	+1/2 ⇔ -1/2
3	36 mT	118^o	60^o	-1/2 ⇔ +1/2
4	19 mT	38^o	20^o	-1/2 ⇔ -1/2
4	19 mT	143^o	-160^o	+1/2 ⇔ +1/2
4	36 mT	140^o	-45^o	-1/2 ⇔ +1/2
4	36 mT	40^o	135^o	+1/2 ⇔ -1/2
5	19 mT	38^o	110^o	-1/2 ⇔ -1/2
5	19 mT	142^o	-70^o	+1/2 ⇔ +1/2
5	36 mT	140^o	45^o	-1/2 ⇔ +1/2
5	19 mT	40^o	-135^o	+1/2 ⇔ -1/2
6	19 mT	78^o	37^o	-1/2 ⇔ -1/2
6	19 mT	102^o	-144^o	+1/2 ⇔ +1/2
6	36 mT	62^o	30^o	-1/2 ⇔ +1/2
6	36 mT	118^o	-150^o	+1/2 ⇔ -1/2

Table 6.2: Optical clock transitions with angular coordinates of $\vec{\boldsymbol{B}}$ given relative to the (<100>,<010>,<001>) crystalline axes. These positive and negative projections are based on the unit cell directions for the 6 sites for the Tm:YGG.

6.10. CONCLUSION *

We conducted a series of spectroscopic studies that allowed us to measure the full spin-Hamiltonian for Tm:YGG. Despite the multiple sites, a combination of SHB and ODNMR determined both the ground-state and excited-state hyperfine tensors. These tensors were confirmed to match the results of a pair of independent experiments with magnetic field directions limited to the <111> crystal axis. This new knowledge allowed us to determine a series of directions that should create optical clock transitions for specific thulium sites, and in turn, enhance the optical coherence of the transition in this material. This confirms the potential of Tm:YGG crystals for quantum networking and quantum memory applications.

6.11. SUPPLEMNTARY INFORMATION

6.11.1. FITTING DETAILS

To fit the data present in each of the angular scans we begin with a simple linear regression problem of the form:

$$\boldsymbol{A}\vec{\lambda} = \vec{\Delta} \tag{6.6}$$

where $\boldsymbol{A}$ is a m x 3 matrix of magnetic field projections, where each of the m rows, representing a particular ion site at a particular angle, is given by B_x, B_y, B_z. The $\vec{\Delta}$ is a vector that contains all the measured splittings from either ODNMR or SHB given the particular fit. Finally, the $\vec{\lambda}$ vector contains the hyperfine tensor values that solve this system of equations for the series of ion sites at a series of angles. Since no tensor values will fit the measured splittings with zero error and $\boldsymbol{A}$ may not be invertable, the matrix equation in Eq. 6.6 must be generalized to its ordinary least squares version given by

$$\vec{\lambda} = \left(\boldsymbol{A}^{\boldsymbol{T}}\boldsymbol{A}\right)^{-1}\boldsymbol{A}^{\boldsymbol{T}}\vec{\Delta} \tag{6.7}$$

which gives the closest possible fit for the linear sytem of equations. Generalizing again, since the splittings do not depend linearly on the magnetic field projections, we solve the new matrix equation using the nonlinear modeling function of MATLAB for which the user supplies the input vectors $\vec{\lambda}$, $\vec{\Delta}$, and the nonlinear model that describes their relationship, in this case,

$$\Delta_g = \sqrt{g_x^2 B_x^2 + g_y^2 B_y^2 + g_z^2 B_z^2} \tag{6.8}$$

or

$$\Delta_g - \Delta_e = \sqrt{g_x^2 B_x^2 + g_y^2 B_y^2 + g_z^2 B_z^2} - \sqrt{e_x^2 B_x^2 + e_y^2 B_y^2 + e_z^2 B_z^2} \tag{6.9}$$

for the ground and ground minus excited state splittings respectively. The only task remaining is to make sure that each row of projections is associated with the correct resonance splitting to produce the final set of values. These associations were made manually by relating each resonance to the most likely sites and angles using similar initial measurements from [26].

All magnetic field projections are computed based on a unit vector magnetic field in relation to the site axes pictured in main text Figure 1. Each site's axes given in the crystalline cubic cell frame are assumed to be the directions given in 6.3

Site	$\hat{x}$	$\hat{y}$	$\hat{z}$
1 (Black)	(1 -1 0)	(1 1 0)	(0 0 1)
2 (Purple)	(1 1 0)	(-1 1 0)	(0 0 1)
3 (Orange)	(0 1 -1)	(0 1 1)	(1 0 0)
4 (Yellow)	(0 1 1)	(0 -1 1)	(1 0 0)
5 (Green)	(-1 0 1)	(1 0 1)	(0 1 0)
6 (Black)	(1 0 1)	(1 0 -1)	(0 1 0)

Table 6.3: Defined directions in the crystal. These directions were normalized to compute all projections of the magnetic fields. The positive and negative axes are assumed by convention to keep the site $\hat{z}$ directions pointing into the unit cell.

Inverting the sign assumptions present in these directional definitions can result in some underlying changes to the signs but not the magnitudes of the determined tensor values and special directions relative to each defined axis [28].

From the set of all the points for a particular measurement, resonance points that showed no angular dependence or extremely weak signatures were also omitted from the fits. Many of the omitted resonance points appeared at all angles of ODNMR with a splitting of 9-11 MHz/T and are assumed to be the gallium nuclear spin splittings of the host crystal. Finally, a fixed angular correction was made to all points for each particular set of data to account for the experimental uncertainty in the crystal orientation.

6.11.2. SECONDARY FIT OF THE SHB DIFFERENCE TENSOR

Given the experimental uncertainty in angles and orientation, and the manually conducted site assignment for each of the splittings, it is important to verify that the tensor values that are produced by our fitting procedure explain the splitting behavior for multiple crystalline directions. To account for this we rotated the crystal to a new optical axis, defining a new plane in which to rotate the B field, and repeated our angular rotation while collecting SHB data for the new direction. The fitting procedure described above was applied to the resonances of the new direction independently of the data from previous directions. The resulting tensor values, with fits pictured in Fig.6.6, show close agreement with the values produced by the fit of the first direction. The tensor values from both directions are averaged together to give the final values listed for the excited state splittings in the main text.

6.11.3. SECONDARY FIT OF THE ODNMR DIRECTIONAL TENSOR

Following the same logic for all rotational measurements, we conducted ODNMR measurements while rotating around a pair of different optical axes as well. The resulting tensor values, with fits pictured in Fig.6.7, also show good agreement with the values produced by the fit of the first direction. The tensor values from both directions are averaged together to give the final values listed for the ground state splittings in the main text.

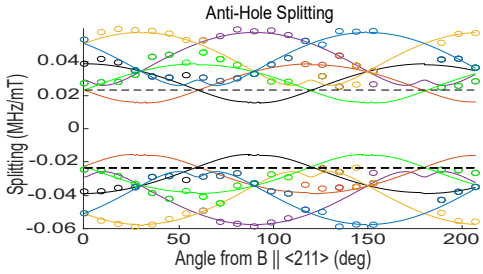

Figure 6.6: Secondary SHB directional fit. **a.** Spectral hole burning antihole splittings measured for an optical axis along the crystalline <110> axis. Dotted lines indicate the minimum measurable splitting due to the width of the central spectral hole.

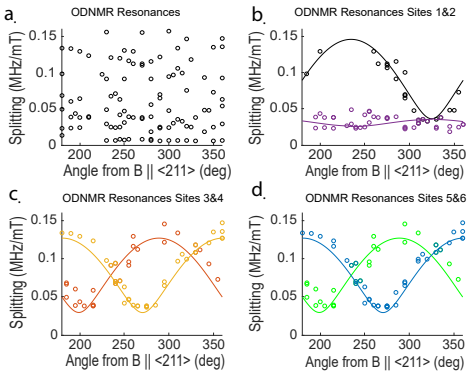

Figure 6.7: Secondary ODNMR directional fit using ODNMR data. **a.** All ODNMR resonances measured for an optical axis along the crystalline <110> axis. **b,c,d.** Site by site fitting of the tensors listed in the main text to the resonances from **a** across a series of angles.

6.11.4. MINIMIZE THE SPIN-INHOMOGENEOUS BROADENING

In the main text, the results for an optical clock transition are depicted to show an insensitive point between a pair of energy levels that belong to the optical transition for the Tm^{3+} ions in this material. The purpose of this point is to minimize the contribution of magnetic fluctuations to the uncertainty in optical transition energy. A similar analogy can be drawn to the pair of ground state hyperfine levels if that is instead the transition of interest. Since the nuclear spin of thulium is 1/2 however, these levels will always experience a linear splitting relative to the magnitude of the applied magnetic field. In other words, a complete ZEFOZ point is not accessible in this system. However, by choosing a specific orientation in the hyperfine tensor space, as in the case of [34], the effects on these spins due to orientation fluctuations of the local magnetic field can be minimized.

To improve future possibilities for spin control in Tm:YGG we have conducted the same analysis as in the case of [34]. We compute, for some magnetic field amplitude, the magnitude at all angles of the splitting of the ground state spin levels. Finding, for each of the present sites, extrema in this angular splitting landscape, we pinpoint orientations

where the splitting between hyperfine states has the smallest variation with respect to local angular change of an external magnetic field. The results of this computation are shown for each of the six sites in Fig.6.8. These external field orientations, computed

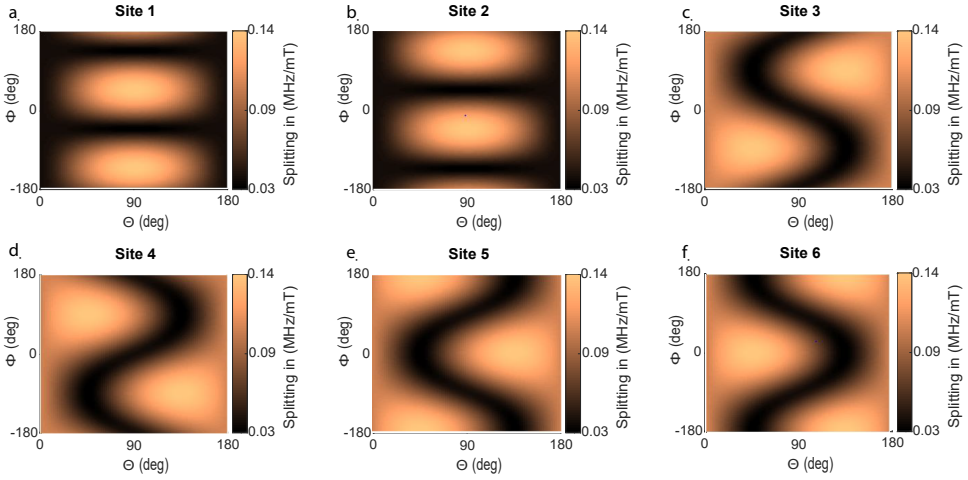

Figure 6.8: **a-f.**Site by site orientation map of the ground state splittings. The highlighted extrema of each surface indicate the orientations of reduced sensitivity to angular magnetic field fluctuations.

from the tensors, will result in the narrowest possible spin transition inhomogeneous broadening in this material, and have potential to enable dynamical decoupling and spin control sequences.

6.11.5. BRANCHING RATIO SIMULATIONS AND DIRECTIONS

An additional aspect of interest in these rare earth ion-doped crystal systems is to create a lambda system where two lower energy levels are each connected via optical transition to a single excited state [8, 23, 35]. Such a system is relevant to a number of different quantum memory schemes. Since there are only a pair of degenerate hyperfine levels in this spin 1/2 system, the pair of ground states that couple to a single excited level must be the $\pm 1/2$ ground-state hyperfine levels. Due to the hyperfine mixing of the electronic and nuclear wave-functions, such spin crossing transitions become weakly allowed, alongside their spin preserving counterparts. By describing an effective magnetic field felt by the nuclear spin due to each of the nearest crystal field levels, the amount of spin mixing that is possible can be calculated from the hyperfine tensor values of Tm:YGG. Following the definition of an effective B field vector in the ground and excited states from[35], we compute the likely branching ratio for each ion site at all possible orientations to determine which angles may yield the best spin crossing transition probability for each site in Tm:YGG. The results are shown in Fig.6.9 for a fixed field magnitude at all orientations. Due to the lower anisotropy of the hyperfine tensors, the maximum branching ratios that appear possible in Tm:YGG is $\sim 5\%$, much lower than the case of $\sim 25\%$ in Tm:YAG.

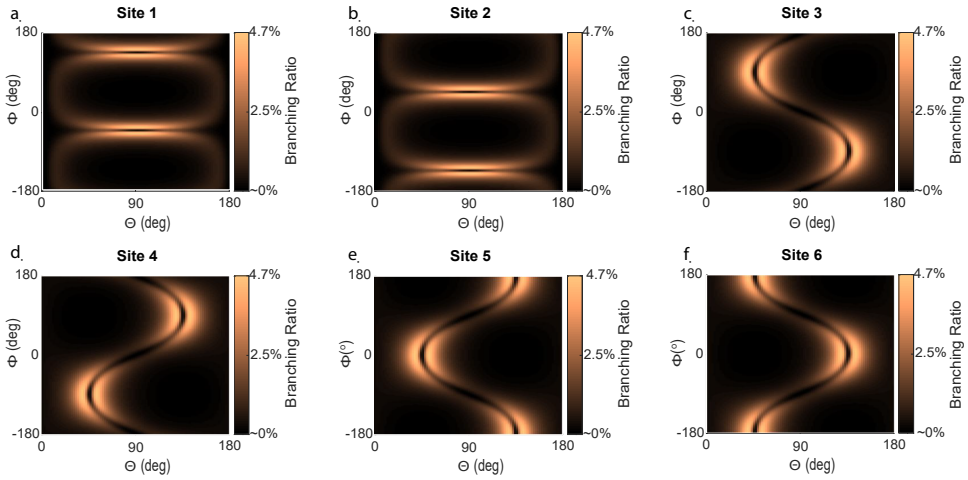

Figure 6.9: **a-f.**Site by site orientation map of the branching ratio R as defined in [35]. Each site reaches a maximum branching ratio of ~ 5% for certain angles close to the particular local $\hat{x}$ axis

ACKNOWLEDGMENTS*

All research at Montana State University was sponsored by Air Force Research Laboratory under agreement number FA8750-20-1-1009. Additionally, we acknowledge funding through the Netherlands Organization for Scientific Research (NWO), and the European Union's Horizon 2020 research and innovation program under grant agreement No 820445 and project name Quantum Internet Alliance. Finally, we appreciate the help of Thomas Rust for his work cutting and polishing some of the many crystal samples used in this work.

BIBLIOGRAPHY

[1] J. H. Davidson et al., "Measurement of the thulium ion spin hamiltonian in an yttrium gallium garnet host crystal", Phys. Rev. B **104**, 134103 (2021).

[2] W. R. Babbitt et al., "From spectral holeburning memory to spatial-spectral microwave signal processing", Laser Physics **24**, 094002 (2014).

[3] W. Tittel, M. Afzelius, T. Chaneliére, R. Cone, S. Kröll, S. Moiseev, and M. Sellars, "Photon-echo quantum memory in solid state systems", Laser & Photonics Reviews **4**, 244–267 (2010).

[4] Y. C. Sun, "Rare earth materiais in optical storage and data processing applications", in *Spectroscopic properties of rare earths in optical materials*, edited by R. Hull, J. Parisi, R. M. Osgood, H. Warlimont, G. Liu, and B. Jacquier (Springer Berlin Heidelberg, Berlin, Heidelberg, 2005), pp. 379–429.

[5] A. Kaplyanskii and R. McFarlane, *Spectroscopy of crystals containing rare earth ions* (Elsevier, 2012).

[6] E. Fraval, M. J. Sellars, and J. J. Longdell, "Method of extending hyperfine coherence times in $Pr^{3+}:Y_2SiO_5$", Phys. Rev. Lett. **92**, 077601 (2004).

[7] R. MacFarlane, C. Yannoni, and R. Shelby, "Optical line narrowing by nuclear spin decoupling in pr3+: laf3", Optics Communications **32**, 101–104 (1980).

[8] O. Guillot-Noël, P. Goldner, E. Antic-Fidancev, and J. L. Le Gouët, "Analysis of magnetic interactions in rare-earth-doped crystals for quantum manipulation", Phys. Rev. B **71**, 174409 (2005).

[9] N. Ohlsson, M. Nilsson, S. Kröll, and R. K. Mohan, "Long-time-storage mechanism for tm:yag in a magnetic field", Opt. Lett. **28**, 450–452 (2003).

[10] C. W. Thiel, N. Sinclair, W. Tittel, and R. L. Cone, "Optical decoherence studies of $Tm^{3+}:Y_3Ga_5O_{12}$", Phys. Rev. B **90**, 214301 (2014).

[11] C. W. Thiel, N. Sinclair, W. Tittel, and R. L. Cone, "$Tm^{3+}:Y_3Ga_5O_{12}$ Materials for spectrally multiplexed quantum memories", Phys. Rev. Lett. **113**, 160501 (2014).

[12] M. Zhong, M. P. Hedges, R. L. Ahlefeldt, J. G. Bartholomew, S. E. Beavan, S. M. Wittig, J. J. Longdell, and M. J. Sellars, "Optically addressable nuclear spins in a solid with a six-hour coherence time", Nature **517**, 177–180 (2015).

[13] M. Rančić, M. P. Hedges, R. L. Ahlefeldt, and M. J. Sellars, "Coherence time of over a second in a telecom-compatible quantum memory storage material", Nature Physics **14**, 50–54 (2018).

[14] R. MACFARLANE and R. SHELBY, "Chapter 3 - coherent transient and holeburning spectroscopy of rare earth ions in solids", in *Spectroscopy of solids containing rare earth ions*, Vol. 21, edited by A. KAPLYANSKII and R. MACFARLANE, Modern Problems in Condensed Matter Sciences (Elsevier, 1987), pp. 51–184.

[15] A. Abragam and B. Bleaney, *Electron paramagnetic resonance of transition ions*, English, Oxford, 2012.

[16] M. TEPLOV, "Magnetic resonance on pr 141 nuclei in a pr2 (s04) 3· 8h20 single crystal", Zh. Eksp. Teor. Fiz **53**, 1510–1515 (1967).

[17] L. Veissier, C. W. Thiel, T. Lutz, P. E. Barclay, W. Tittel, and R. L. Cone, "Quadratic zeeman effect and spin-lattice relaxation of Tm^{3+}:yag at high magnetic fields", Phys. Rev. B **94**, 205133 (2016).

[18] A. Abragam and B. Bleaney, "Enhanced nuclear magnetism: some novel features and prospective experiments", Proceedings of the Royal Society of London. Series A, Mathematical and Physical Sciences **387**, 221–256 (1983).

[19] J. F. Dillon and L. R. Walker, "Ferrimagnetic resonance in rare-earth doped yttrium iron garnet. ii. terbium substitution", Phys. Rev. **124**, 1401–1413 (1961).

[20] G. Menzer, "Xx. die kristallstruktur der granate", Zeitschrift für Kristallographie - Crystalline Materials **69**, 300–396 (01 Dec. 1929).

[21] Y. Sun, G. M. Wang, R. L. Cone, R. W. Equall, and M. J. M. Leask, "Symmetry considerations regarding light propagation and light polarization for coherent interactions with ions in crystals", Phys. Rev. B **62**, 15443–15451 (2000).

[22] R. Lauro, T. Chanelière, and J. L. L. Gouët, "Slow light using spectral hole burning in a tm3+: yag crystal", arXiv preprint arXiv:0902.2657 (2009).

[23] A. Louchet, J. S. Habib, V. Crozatier, I. Lorgeré, F. Goldfarb, F. Bretenaker, J.-L. L. Gouët, O. Guillot-Noël, and P. Goldner, "Branching ratio measurement of a Λ system in Tm^{3+} : YAG under a magnetic field", Phys. Rev. B **75**, 035131 (2007).

[24] L. Erickson, "The nuclear quadrupole interaction in pr3+:laf3 — an optical-rf double resonance measurement of the ground electronic state", Optics Communications **21**, 147–149 (1977).

[25] A. J. Silversmith, A. P. Radli ński, and N. B. Manson, "Optical study of hyperfine coupling in the $^7F_0$ and $^5D_0$ states of two Eu^{3+} centers in CaF_2 and CdF_2", Phys. Rev. B **34**, 7554–7563 (1986).

[26] E. Jones, "Observation of the tm169 nuclear magnetic resonance in thulium gallium garnet", Journal of Physics and Chemistry of Solids **29**, 1305–1308 (1968).

[27] V. H. Schmidt and E. D. Jones, "Nuclear-magnetic-rosonance study of thulium aluminum garnet", Phys. Rev. B **1**, 1978–1986 (1970).

[28] D. L. McAuslan, J. G. Bartholomew, M. J. Sellars, and J. J. Longdell, "Reducing decoherence in optical and spin transitions in rare-earth-metal-ion–doped materials", Phys. Rev. A **85**, 032339 (2012).

[29] J. V. Vleck, *The theory of electric and magnetic susceptibilities*. English ([s.n.], Oxford, 1932).

[30] J. J. Longdell, A. L. Alexander, and M. J. Sellars, "Characterization of the hyperfine interaction in europium-doped yttrium orthosilicate and europium chloride hexahydrate", Phys. Rev. B **74**, 195101 (2006).

[31] M. Lovri ć, P. Glasenapp, D. Suter, B. Tumino, A. Ferrier, P. Goldner, M. Sabooni, L. Rippe, and S. Kröll, "Hyperfine characterization and spin coherence lifetime extension in pr^{3+}:$la_2(wo_4)_3$", Phys. Rev. B **84**, 104417 (2011).

[32] D. Kielpinski, V. Meyer, M. A. Rowe, C. A. Sackett, W. M. Itano, C. Monroe, and D. J. Wineland, "A decoherence-free quantum memory using trapped ions", Science **291**, 1013–1015 (2001).

[33] R.-C. Tongning, T. Chanelière, J.-L. L. Gouët, and M. F. Pascual-Winter, "Optical clock transition in a rare-earth-ion-doped crystal: coherence lifetime extension for quantum storage applications", **605**, 012037 (2015).

[34] M. F. Pascual-Winter, R.-C. Tongning, T. Chanelière, and J.-L. Le Gouët, "Spin coherence lifetime extension in tm^{3+}:yag through dynamical decoupling", Phys. Rev. B **86**, 184301 (2012).

[35] F. de Seze, A. Louchet, V. Crozatier, I. Lorgeré, F. Bretenaker, J.-L. Le Gouët, O. Guillot-Noël, and P. Goldner, "Experimental tailoring of a three-level Λ system in Tm^{3+} : YAG", Phys. Rev. B **73**, 085112 (2006).

7

FREQUENCY DEPENDENT POPULATION DYNAMICS OF THULIUM DOPED YTTRIUM GALLIUM GARNET

Jacob H. Davidson*, Antariksha Das*, Nir Alfasi, Charles Thiel, Rufus Cone, Wolfgang Tittel

I'm Hanz... and I'm Franz, and we want to Pump... You Up!

Dana Carvey and Kevin Nealon

The creation of well understood structures using spectral hole burning is an important task in the use of technologies based on rare earth ion doped crystals. We apply a series of different techniques to model and improve the frequency dependent population change in the atomic level structure of Thulium Yttrium Gallium Garnet (Tm:YGG). In particular we demonstrate that at zero applied magnetic field, numerical solutions to frequency dependent three-level rate equations show good agreement with spectral hole burning results. This allows predicting spectral structures given a specific hole burning sequence, the underpinning spectroscopic material properties as well as the relevant laser parameters, and enables us to largely eliminate power dependent hole broadening through the use of adiabatic hole-burning pulses. Though this system of rate equations shows good agreement at zero field, the addition of a magnetic field results in unexpected spectral diffusion that is

Large portions of this chapter will be submitted to a journal.

*These authors contributed equally to this work.

proportional to the induced Tm ion magnetic dipole moment and average magnetic field strength and dominates the optical spectrum over long time scales. Our results allow optimization of the preparation process for spectral structures in a large variety of rare earth ion doped materials for quantum memories and other applications.

7.1. PREAMBLE

The work detailed in this chapter represents an optimization of our process for crafting AFC quantum memories in Tm:YGG. Until recently creating a good AFC with the desired storage time and the best efficiency in our group has been considered as much art as science to correctly optimize the resulting memory. With this work, we gain the ability to work from known parameters such as laser power, laser linewidth, and a programmed sequence of optical pulses in order to predict the eventual shape of an AFC. With that process in hand, we can now optimize the shape of AFC quantum memories in order to maximize storage efficiencies, storage times, multi-mode capacity, or other figures of merit. It is also worth a mention that this process applies to other rare earth ion doped materials as long as spectroscopic properties such as the relevant level lifetimes and branching ratios are well understood. I hope this chapter reads a bit like a recipe for crafting good spectral features using common methods in the field.

The goal is to create improvements across the different figures of merit mentioned in chapter 2. Efficiency is likely to increase as there will be less population lost within the comb bandwidth due to inaccurate pumping. Additionally, we can now more accurately project project the remaining optical depth after hole burning, which, in turn, is important for optimizing for impedance matched cavities. Multi-mode capacity is likely to increase because appropriate burn pulses should allow for creation of good AFC memories over broader bandwidths. Storage times are also likely to increase and approach limitations imposed by material properties rather than Fourier limits, although they are still ultimately limited by laser stability.

7.2. INTRODUCTION

RARE-EARTH ion doped crystals (REICs) are interesting materials due to their long-lived excited states and their exceptionally long optical coherence times at cryogenic temperature [1, 2]. In particular, along with the possibility for spectral tailoring of their inhomogeneously broadened $4f^N$-$4f^N$ transitions, this makes them prime candidates for a number of applications in classical and quantum optics. Examples include laser stabilization, RF spectrum analysis, narrow band spectral filtering, and quantum information storage and processing [2–8].

Thulium-doped Yttrium Gallium Garnet ($Y_3Ga_5O_{12}$, Tm:YGG) is one such material. Its $^3H_6 \leftrightarrow {}^3H_4$ transition at 795 nm wavelength features an optical coherence time of more than 1 ms [9–11], which is among the longest among all studied REICs. In combination with the accessibility of this transition—within the range of commercial diode lasers—this makes it a natural candidate for applications.

The quality of created features and the resulting consequences for associated applications, are dependent on the spectroscopic properties of the dopant ions and their numerous interactions with other atomic components in their local crystalline environment [12, 13], the details of the optical pumping process, and the frequency profile of the applied laser pulses[14, 15]. Deep understanding of the relation between spectroscopic properties, optical control fields, and spectral diffusion dynamics, has resulted in improvements to this process in a number of other rare-earth-doped materials including Tm:YAG, Eu:YSO, and Pr:YSO [16–18]. However, this important connection has thus

far not been made for Tm:YGG.

In this paper we track the evolution of population within the $^3H_6$, $^3H_4$ and $^3F_4$ electronic levels of Tm^{3+} ions in YGG (see Fig. XX for simplified level scheme) by semi-continuous monitoring of spectral holes for many sequences of applied spectral hole burning pulses. The characteristic shapes and sizes of these spectral features are matched to a rate equation model that encompasses the ground, excited, and bottleneck levels in this material with associated lifetimes. At zero magnetic field we see good agreement between our numerical model and measured results across many different pump sequences of varying duration, power, and spectral shape. With the addition of an external magnetic field the agreement with our numerical model disappears as spectral diffusion from local host spins begins to dominate the shape of all spectral features over long timescales. We characterize the nature of this unexpected behavior and expand our model accordingly by adding a spectral diffusion term to account for a quadratic Zeeman interaction with present noisy magnetic fields [19, 20].

The chapter is structured as follows: In section 7.3 we describe the experimental setup used to collect our measurements. In section 7.4 we detail the atomic level structure in Tm:YGG and introduce spectral hole burning, the workhorse of our investigations, to select a known set of atomic population. In section 7.5 we introduce and apply a rate equation model which shows good agreement to the measured spectral hole features. In section 7.6 we detail the use of adiabatic pulses to shape spectral holes at zero magnetic field with the goal of creating high-resolution features. Section 7.7 focuses on changes to spectral hole burning in the presence of magnetic fields and the observation of magnetic noise that creates un-controlled changes to measured results. Section 7.8 describes the characterization of this magnetic noise as a creator of spectral diffusion that differentiates the measured results from those predicted by our model over longer timescales. Finally section 7.9 concludes this chapter.

7.3. EXPERIMENTAL SETUP

To measure persistent and transient spectral holes over different timescales in Tm:YGG we use the setup detailed in figure 7.1. A CW diode laser tuned to the ion transition frequency at 795.325nm [21] is locked to a linewidth of roughly 5kHz [22]. To craft short pulses of high extinction ratio, its continuous wave emission is directed to a free space AOM. The sinusoidal driving signal of the AOM is mixed with a signal modulated by an arbitrary function generator, which allows programmable control of the transmitted pulse amplitude for the first order light.

After the amplitude control, the pulsed light is directed to a fiber coupled phase modulator driven using arbitrary waveforms for serrodyne frequency shifting and more complex chirped pulse shapes as detailed in section 7.6. The optical signals are then sent through a polarization controller to a 1% Tm:YGG crystal grown by Scientific Materials Corp. and housed in a pulse tube cooled cryostat at 500-700mK. A superconducting solenoid centered on the crystal applies a homogeneous magnetic field from 0-2T(using about 1mA/mT of current) along the crystal's <111> axis. Signals transmitted through the crystal are directed to a fiber coupled photo diode and recorded for subsequent analysis

Experimental control is handled on a number of different time scales via a custom

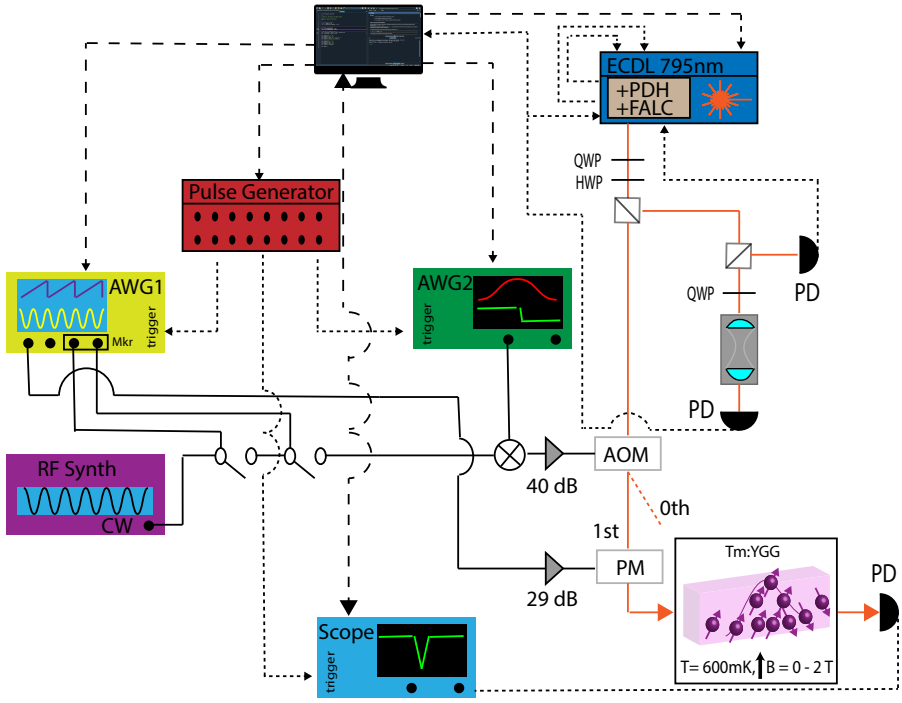

Figure 7.1: Schematic of the experimental setup. A PC programs a sequence on a pulse generator (SpinCore Pulseblaster) with nanosecond timing resolution that produces a set of trigger pulses for all devices. Waveforms written to an arbitrary waveform generator (AWG1,Tektronix AWG 70002A) voltage channel, are subsequently amplified (SHF S126 A), and drive an electro optic phase modulator (PM) to generate side bands on the laser light at arbitrary frequencies. The AWG marker channels drive a set of home-built electrical switches which gate the drive signal of an acousto-optic modulator (AOM) to create short pulses from the laser light. This gated AOM signal is mixed with fast arbitrary voltage pulses(AWG2,Tektronix AFG 3102), amplified (Mini-Circuits ZHL-5W-1+), and sent to an acousto-optic modulator (AOM Brimrose 400MHz) to synthesize controllable-amplitude laser pulses with rise times as short as 2.5ns. We use a single light source (Toptica DL Pro 795nm) for different tasks (optical pumping, pulse generation, etc). The laser frequency is set via a wavemeter (Bristol 871) and locked to a thermally and acoustically isolated high finesse optical cavity (Stable Laser Systems) via the Pound-Drever-Hall method and a fast feedback loop acting on the laser current and piezo voltage (Toptica PDH and FALC Modules). Transmitted signals from the crystal are directed to a variable-bandwidth photo detector (NewFocus 2051) and displayed on an oscilloscope (Lecroy Waverunner 8100A) configured by the PC and synchronized with the experimental sequence by a trigger signal.

python script that ensures signals are created at the correct moment [23]. For sequencing on timescales of longer than a second, the built-in python timing functions are used to adjust the experiment. On all timescale shorter than seconds, timing is handled by preprogramming a pulse generator that produces correctly timed trigger signals for the various devices. Waveforms for the arbitrary voltage signals are generated by custom scripts and uploaded to the respective devices for arbitrary control of instantaneous pulse frequencies and amplitudes.

7.4. TM:YGG SITE AND LEVEL STRUCTURE

Garnet crystals such as YGG have cubic crystal structure with O_h^{10} space group symmetry, which yields six Tm^{3+} ion substitution sites, each with D_2 point group symmetry[10, 24–26]. The magnetic and optical behavior of Tm^{3+} ions in each of these sites is identical but the crystal structure leads to effective magnetic inequivalence between the sites due to six different orientations that the ion and its entire local environment can take within the lattice [27]. However, for a few specific directions, ions at in-equivalent sites can be cast into classes that share the same projections of applied electromagnetic fields ($\vec{E}, \vec{B}$) onto their local site axes.

Given the orientation of the magnetic field, the crystalline <111> axis, we cast the ions into two different classes as depicted in Fig. 7.2 a. One class features projections along the local ion's X and Z axes (blue), and the other projections along the local Y and Z axes (red). The ions in each separate class experience different magnetic field projections. This becomes evident from a simple spectral hole burning experiment, which we use to introduce the remaining results of the paper.

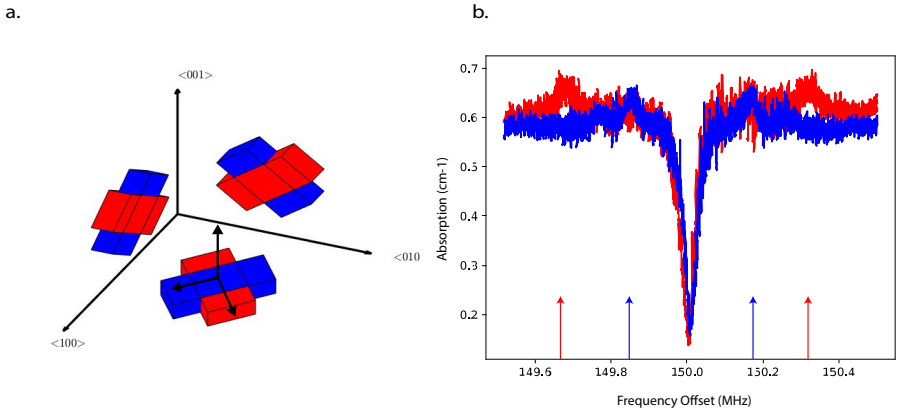

Figure 7.2: **a.** Depiction of the six ion substitution sites relative to the cubic crystal cell. For a magnetic field along the crystalline <111> axis the sites are cast into two classes of different field projection, shown in red and blue. Small black arrows indicate the local site X,Y,Z, axes for the red site in the <100> <010> plane. **b.** A pair of hole burning spectra with the main spectral hole pictured in the center. Each hole, shown in an associated color to part **a.**, is burned with a polarization that selects one of the two classes of ions and produces anti-holes with different splitting (indicated by the colored arrows). Additional modulations of the optical depth outside the hole originate from mistakes in the crystal orientation during fabrication.

In spectral hole burning, a long optical pump pulse excites atomic population in a narrow spectral window within an inhomogeneously broadened absorption line. Excited ions subsequently decay — either back into the original state, or into another energy level that often belongs to the electronic ground state manifold. Scanning a weak laser beam over a spectral interval centered on the frequency of the original pump pulse reveals sections of decreased and increased absorption — so-called spectral holes and anti-holes. Spectral holes occur at frequencies of reduced ground-state population, i.e.

with offset $\Delta = 0$ (for the central hole) and $\Delta = D_e$ (for the side hole), and anti-holes can be observed whenever the ground-state population is increased, which happens at $\Delta = D_g$ and $\Delta = D_g + D_e$. Here, D_g and D_e are ground and excited state splittings. Consult Ref.[14, 28, 29] for more details on spectral hole burning.

In our case, the ground and excited state splittings depend on the magnitude and direction of the applied magnetic field — that vary for each class of Tm ions [27]. At 7.5 mT we recorded a pair of hole burning spectra, shown in Figure 7.2 b, for orthogonal polarizations. This allowed us to selectively address ions in either of the two classes. We found two sets of anti-holes, each of which split according to the different field projections experienced by the two classes of Tm^{3+} ions. This ability to select out a single class of ions becomes important in section 7.8 spectral diffusion depends on the magnetic projection on each specific class of ions.

7.5. MODELING RESULTS USING THREE-LEVEL RATE EQUATIONS

To further understand the effects of a given hole burning process on our REIC ensemble we turn to solutions of the Maxwell-Bloch equations that describe the interaction of light with one or many two level systems. These differential equations can be quite difficult to solve, given the complexity that there does not exist a single fixed Rabi frequency to drive all ions [30]. For our case we make the simplifying assumption that all applied optical pulses are shorter than the coherence time of the addressed transition. The Maxwell-Bloch equations can then be reduced to a set of rate equations that describe the conserved total atomic population, and how it flows through the different available levels as a function of time [15].

Note that in the case of narrow band excitation, of an inhomogeneously broadened transition, where only a certain portion of atoms are driven, frequency dependence must be added. Following [15] and [16, 31] we describe the dynamics of our atomic ensemble with equations 7.1-7.3.

$$\frac{\partial n_g(t)}{\partial t} = R(\Delta)(n_e - n_g) + \frac{1-\zeta}{T_e} n_e + \frac{1}{T_b} n_b \tag{7.1}$$

$$\frac{\partial n_e(t)}{\partial t} = R(\Delta)(n_g - n_e) - \frac{1}{T_e} n_e \tag{7.2}$$

$$\frac{\partial n_b(t)}{\partial t} = \frac{\zeta}{T_e} n_e - \frac{1}{T_b} n_b \tag{7.3}$$

This system of coupled differential equations describes the relative change of atomic population, $n_{(g,e,b)}(\Delta)$ in three ion levels as a function of time. The branching ratio ζ determines how much population decays from the excited state $|e\rangle$ through the bottleneck state $|b\rangle$ before reaching the ground state $|g\rangle$ with respective level lifetimes T_e and T_b. To drive the system, a frequency dependent excitation rate $R(\Delta)$ is added which characterizes the applied pulses of light used for hole burning. For Tm:YGG, the level lifetimes and branching ratios are well known at zero magnetic field [21] leaving only one unknown,

the frequency dependent optical pumping rate which has to be matched with measured data.

This pumping rate $R(\Delta)$ is a function of both the individual ion properties and the applied sequence of laser excitation, or burning, pulses. Again from [16],

$$R(\Delta) \propto \gamma * \mathbb{F}(\Delta)_{Opt} \tag{7.4}$$

is a convolution of the two factors, the homogeneous linewidth γ of the ionic transition and the Fourier spectrum of the applied pulse sequence $\mathbb{F}(\Delta)_{Opt}$. For the case of Tm:YGG the homogeneous linewidth of the ions is expected to be narrower than 600Hz [21]. For any $\mathbb{F}(\Delta)_{Opt}$ with features greater than the homogeneous linewidth of the ions this convolution is dominated by the Fourier spectrum of the pumping pulse, which is determined by laser and sequence characteristics such as pump power, pulse duration, pulse spacing, and spectral line-shape.

We perform many different hole burning experiments with differently timed burning sequences of various powers, durations, and waiting periods. See figure 7.3 a. With these parameters set, and the known lifetimes and branching ratios of Tm:YGG, we numerically solve the rate equations above for all times in the burning sequence after setting the initial conditions before pumping to $n_g = 1$(i.e. after initializing all population in the ground state). An example is shown in Figure 7.3 b, showing the predicted development of a spectral hole over time for some chosen $R(\Delta)$ parameter. The measured evolution of the spectral hole after the same series of pumping pulses and waiting times is shown in Figure 7.3 c where the spectral hole is read out after the every burn pulse to capture the evolution.

As the optical depth of a measured spectral hole is proportional to the atomic population left to absorb in the ground state we normalize and match the results generated by experiment and by numerical simulation for a particular burning sequence [15, 16]. Note that since we do not have an analytical function which describes the solution to the system of rate equations, the matching is not a fit that outputs a mean standard error. However, as a "goodness of fit" metric, we calculate the point-wise average difference between the measured and simulated surfaces. Solutions and measurements are shown for a few different times in Figures 7.3 d,e to demonstrating close agreement for matched parameters. More examples of different burning sequences, a discussion of the resulting holes with respect to the level lifetimes, and a note on the power dependence of the laser line-shape are included in the supplementary information 7.10.

We consider many different $R(\Delta)$ functions to validate our model. Only one of which creates the closest match between measured results and our model across all different pumping sequences. This allows us to uniquely identify the $R(\Delta)$ parameter as a property of our laser source and its interaction rate with the ions.

All burning sequences match a source with a Lorentzian shaped laser line of $\gamma = 5$ kHz linewidth with a excitation rate amplitude a tunable between approximately 300 Hz and 2.5 kHz giving an $R(\Delta)$ function of the form

$$R(\Delta) = a\frac{\gamma^2}{\gamma^2 + (\Delta - \Delta_o)^2} \quad \text{for} \quad a \in [0.3, 2.5]kHz, \gamma = 0.005MHz, \Delta_o = 150MHz \tag{7.5}$$

where Δ_o is the detuning from the thulium absorption line center.

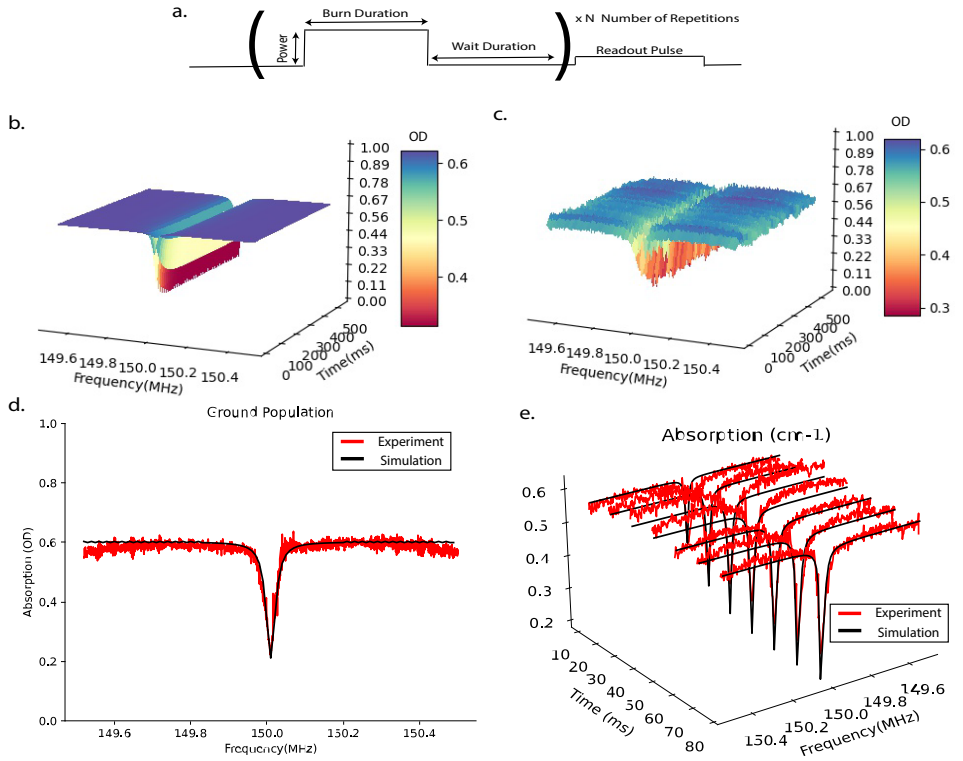

Figure 7.3: **a.** Simple hole-burning sequence used throughout the paper. **b.** Evolution of a spectral hole simulated using Eqs. 7.1-7.3. The hole is detuned by 150MHz from the peak of the Tm absorption line and develops slowly in time. **c.** Measured hole evolutio. The hole-burning sequence is as in b. The hole deepens as more burn pulses are applied. **d.** The final hole of both methods after 50 cycles of alternating 1ms long pump pulses and 10ms waiting periods. **e.** Overlaid slices at many times throughout the burning process.

Thus our model for population change driven by this known optical spectrum allows us to predict the size and shape of any spectral feature resulting from a given burning sequence in this material at zero external magnetic field. This strategy should extend to other materials as long as the relevant branching ratios and lifetimes are known.

7.6. ADIABATIC PULSE SHAPING

To further confirm our measurements, and eliminate hole broadening mechanisms from the optical pumping process, we sought to change the spectral shape of our excitation light to create predictable changes to the width and shape of the resulting spectral holes without dependence on our excitation laser line shape. We use adiabatic pulse shaping to isolate the shape and width of created spectral features for further optimization while continuing to match to solutions of our predictive model.

An important method for controlling the shape and width of a desired spectral feature stems from an early goal of NMR to design a pulse which creates highly efficient yet

highly selective population inversion [32]. The resulting coherent population inversion over a narrow frequency bandwidth is described by a unique but exact analytical solution to the Maxwell-Bloch equations [33]. This method is known as a hyperbolic secant pulse and relies upon slow adiabatic tuning of the amplitude and phase of the driving pulse to eliminate unwanted frequency components around the desired bandwidth [15, 34]. Put another way, the adiabatic change of the real and imaginary components of the light field creates a pulse with a particularly square spectrum as shown in figure 7.4 c. For REICs, hyperbolic secant pulses were first considered for quantum computing in order to create high fidelity π pulses for narrow bandwidth ensembles of ions [18, 35]. To craft adiabatic hyperbolic secant pulses experimentally, the first consideration is how to shape the appropriate modulations of the light field.

The original Maxwell-Bloch solutions call for simultaneous slow modulation of the amplitude and phase, each with a different shape. This is equivalent to modulation of the pulse amplitude and frequency shifting during the duration of the pulse [32]. From a hardware standpoint the problem becomes creating fast electronic control of the amplitude $A(t)$ and instantaneous frequency $f(t)$.

To control the amplitude in our setup we mix an AC voltage pulse of the required hyperbolic secant shape with our sinusoidal AOM drive signal to create a driving voltage signal given by

$$A(t) = a(\sin(\omega_{\mathrm{AOM}} t) \otimes \mathrm{sech}(\beta t)) \tag{7.6}$$

Here ω_{AOM} is the AOM drive frequency, a is the maximal pulse amplitude, and β is a parameter that sets the FWHM of the pulse relative to the required burning duration. The shape, shown in figure 7.4 a, and timing of the AC voltage pulse are adjusted and optimised using our custom python script to write the parameters to an arbitrary function generator.

Simultaneously, we change the frequency using a phase modulator driven either by a sinusoidal or a serrodyne signal to create, and shift, side bands on the pump light. This frequency modulation is described by

$$f(t) = \Delta_o + \frac{\delta}{2}\tanh(\beta t) \tag{7.7}$$

where Δ_o is the central frequency of the desired spectral feature as above in the expression for $R(\Delta)$. The same β parameter is included to ensure the peak amplitude of the pulse matches the duration of the central slope of the hyperbolic tangent frequency modulation. Finally, δ is the width of the desired spectral feature. The resulting shape of the frequency spectrum can be seen in fig 7.4 b.

To account for the separate elements responsible for each modulation, a variable delay is added to the amplitude modulation to ensure that the correct portion of each pulse is temporally aligned with the corresponding frequency shift.

This method of creating spectral features is in contrast to the common method of linearly swept serrodyne modulation [34, 36, 37]. To show the benefit we picture example Fourier transforms of pulses crafted by both methods in figure 7.4 c. For the broadband features both methods are fairly similar, but for creating narrow-band spectral features

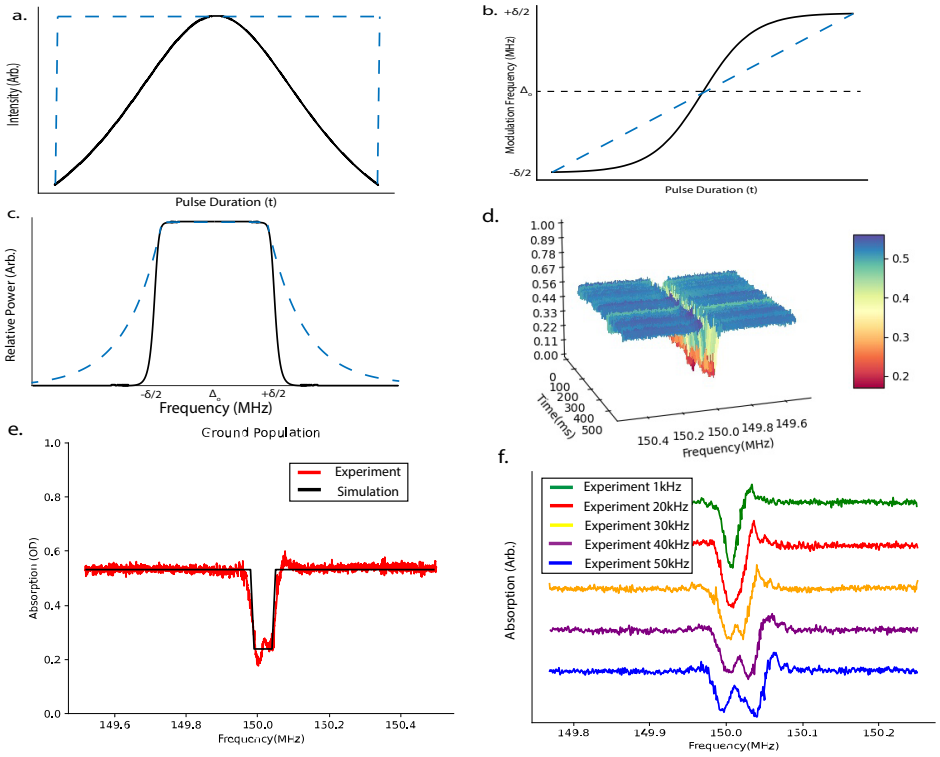

Figure 7.4: **a.** Amplitude shape of a hyperbolic secant shaped pulse. The dashed line shows a square pulse for comparison. **b.** Shape of a hyperbolic tangent frequency modulation. The dashed line shows a linearly chirped pulse for comparison.**c.** Example Fourier transforms for the pair of different types of modulation in **a,b.**. **d.** Spectral holes generated using hyperbolic secant burn pulses. **e.** Last hole obtained by means of simulation and measurement. The hole is square shaped compared to Lorentzian shaped ones in fig. 7.3. Modulations at the bottom of the hole are due to imperfections in the burning pulses, and the square line shows comparison to modeled results from a perfectly square $R(\Delta)$ function of matching bandwidth. **f.** Hyperbolic secant pulses set to create spectral holes with modulation widths between 1kHz and 50kHz for fixed burning duration and power. The hole width is controllable while maintaining its square shape as long as the modulation bandwidth is larger than the laser linewidth.

on the order of the pump laser linewidth, the spectrum of the adiabatic pulse shows much steeper rising and falling edges than that of the linearly shifted pulse.

To show the clear difference in spectral hole shape using this method, we carry out a hole burning experiment in the same fashion as in the previous section with the key difference of each burning pulse being subject to adiabatic amplitude and frequency modulation. The simulated and measured results of this hole burning experiment are compared in Figures 7.4 e. The hole shape clearly changes corresponding to the altered excitation spectrum $R(\Delta)$. The shape of the resulting hole spectrum is fully controllable in terms of width by altering the range of the hyperbolic secant pulse modulations. An example of approximately square spectral holes of differing widths is shown in figure 7.4 f for a series of different chirp bandwidths. The original pump laser linewidth before

modulation and the scaling of the excitation rate due to the Lorentzian wings of the spectrum with added laser power remains an experimental limit, which provides an ultimate lower bound for the minimum width of a spectral feature, square or otherwise.

7.7. MAGNETIC NOISE

With the ability to control the frequency chirp range, and the amplitude and duration of each burning pulse, creation of many possible spectral features, at zero magnetic field, is well understood from the model in Eqs. 7.1-7.3. However, the lifetime of $^3F_4$ the bottleneck level in Tm:YGG creates an upper limit for burning deep yet sharp holes with a reasonable laser power. To improve the depth and lifetime of the resulting features, we now add a magnetic field to create a longer-lived bottleneck state; a ground state spin level with lifetimes of seconds.

It is worth noting at this point, that $R(\Delta)$ is the only term with frequency dependence in the model. Thus, with applied field an identical set of initial population is excited by the same pulse sequences carried out at zero field. Ideally, only the duration of the subsequent decay path from the excited state can change as magnetic fields are applied and lifetimes are changed. However, it will be seen in the following section(s) that though we can initially create spectral features of a shape matching the zero field case, quadratic Zeeman coupling between magnetic field noise and the local spin environment of the Tm ions creates vast changes to these features over long time scales.

With the addition of a magnetic field the ground and excited states of Tm:YGG each split into spin states with a spin-Hamiltonian given by [27]. The created ground state spin level has a much longer lifetime than the $^3F_4$ state previously used as the bottleneck level, prolonging eventual decay to the ground state [38].

A significant portion of electronic population from the $^3F_4$ level decays to the additional spin level before reaching the original ground state, creating, as in [16], an equivalent three level system that should be goverened by the same rate equations after associating the bottleneck level and its lifetime with the new spin level. In addition, to ensure that population accumulates in this level, waiting times between burn pulses must be on the order of the $^3F_4$ state lifetime to prevent population storage in the $^3F_4$ state from where it can decay to the original ground state much more quickly. Measuring the create spectral holes over these longer burning and waiting sequences, previously unavailable without applied field, significant differences compared to the between the modeling become apparent. To assess these differences, spectra in this section and in section 7.8 are taken post burn sequence on a longer timescale than those presented in the previous sections. More speciffically, we measure a created hole periodically, every 10 seconds for minutes.

At higher magnetic fields we observe a clear impact from magnetic field noise on the width and center frequency of the spectral holes. This is evident from figure 7.5 a and b. Here the hole is initially centered at the programmed frequency, but the shape and center proceed to change in an uncontrolled manner. The magnitude of these changes fall within bounds of magnetic field noise caused by variations of the solenoid supply specified by the manufacturer.

To confirm the nature of the measured effect we create a narrow spectral hole at a fixed magnetic field. A short time after burning has completed, we alter the field by a

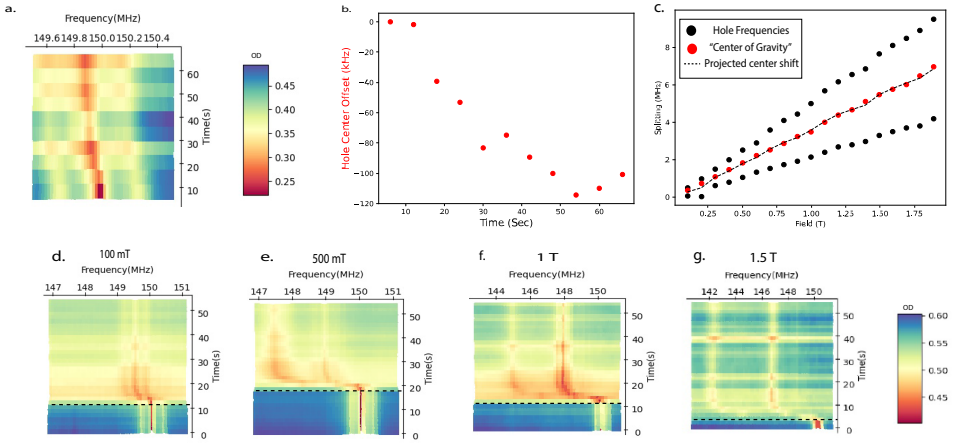

Figure 7.5: **a.** Spectral hole crafted at 1.8 T, and read out repetitively over the course of one minute. **b.** Shift of the center frequency of the spectral hole in time.**c.** Shift of the hole "center of gravity" and splitting into separate features for a fixed change of 1.6mT at initial magnetic fields from 0.1-2 T. The dashed line is the calculated center shift. **d.-g.** Shift of the hole "center of gravity" and splitting into separate features for a fixed change of 1.6mT at initial magnetic fields from 0.1-1.5 T. The dashed line shows the moment when the small change in field was made. The magnitude of the center shift and the splitting both grow as expected from [27] for higher absolute fields.

fixed amount of 1.6 mT, the smallest increment possible with our experimental setup, and measure all subsequent changes to the hole. We expect a splitting and shifting [39] from the linear and quadratic Zeeman terms of the ion spin-Hamiltonian as ions change optical transition frequency in the altered field. We estimate the noise in our system to be a factor of 10 smaller than the applied magnetic field change. The results of these measurements are depicted in Figs. 7.5 c-f. We find that the splitting and shifting of the spectral hole increases drastically from the value of the initial magnetic field was changed from 0.1 to 1.5 T, for constant field changes of 1.6mT.

The measured values of the center shift, and splitting of the pair of resulting holes are in good agreement with expectations from the quadratic and linear components of the hyperfine tensor for these ions [27] using Eq. (5) from [19] to calculate the frequency difference of the optical transition for a pair of fields before and after the 1.6mT change. The implication is that at high magnetic fields, noise on the order of μT can cause many kilohertz of change in the center hole frequency. This result will prove critical for understanding and creating narrow spectral features at high magnetic fields.

7.8. SPECTRAL DIFFUSION

In addition to the central frequency shift, all measured holes are broadened compared to expectations from the burning parameters modeled and tested at zero field, a telltale sign of spectral diffusion [13].

Magnetic field dependent spectral diffusion of spins is well understood in the field of rare earths, although it has more often been considered for the case of Kramers, rather

than non-Kramers ions [20]. The problem is often cast in terms of interactions in which nearby spins that have not been excited swap energy with excited members of the ensemble leading to a general loss of coherence and a spreading, or broadening, of spectral features in time [40, 41]. Both magnetic field and sample temperature play enormous roles as they both mediate how much energy is being interchanged directly through spin-spin interaction or through coupling to host phonons[19]. On short to medium timescales the characteristic rate and magnitude of these processes are often measured via two and three pulse photon echo that allow for spin interactions during their variable delay times[20]. For longer timescales spectral hole burning can accomplish a similar task by mapping the change of the hole shape and size as a function of time, magnetic field, and temperature [13].

By adjusting the polarization of the pump light, we first isolate ions with a particular spin splitting at a certain magnetic field, as discussed in section 7.4. Again, we perform spectral hole burning measurements where burning pulses and waiting periods are timed to guarantee population arrives in the required spin level. Once hole burning is complete, the hole is read out after varying waiting times using, as above, a weak probe in order to leave the hole unperturbed. We determine (i.e. fit) the widths of all holes for a series of different magnetic field amplitudes. Following its change as a function of time it can be described by [20]

$$\Gamma_{hole} \propto \Gamma_o + \frac{1}{2}\Gamma_{SD}(1 - e^{-R_s t_{delay}}). \tag{7.8}$$

Here, Γ_o is some initial hole width given by $R(\Delta)$ of the burning process, which broadens in time. This diffusion approaches a maximum value of Γ_{SD} at a characteristic rate given by R_s. The functional form of the magnetic field and temperature dependence for Γ_{SD} and R_s can be used to link spectral diffusion to a specific broadening mechanism [20, 42, 43].

The first portion of evidence for determining the source of the measured diffusion is the different behavior of each magnetic class of ions. Shown in figure 7.6 a is the hole width of each such class as a function of time for an applied field of 500mT. For the same external field each class broadens at a different rate. However, when different fields are applied, such that the Zeeman splittings of each class are roughly equivalent, the broadening occurs at the same rate, see figure 7.6 b. This contrast likely rules out contributions of two level systems [38] on this time scale, which are likely to be located randomly throughout the material without an orientation dependent response. Instead, the diffusion depends upon the magnitude of the created magnetic dipole moment of the Tm ions.

To further isolate the cause of the diffusion we analyze the behavior of a single class of ions as a function of applied field. Utilizing the model in Eq. 7.8 we fit Γ_{SD} and R_s exclusively for each magnetic class of ions where the functional form of Γ_{SD} is given by [20],

$$\Gamma_{SD}(B,T) = \Gamma_{max}\,\mathrm{sech}^2\left(\frac{g_{env}\mu_B B}{kT}\right) \tag{7.9}$$

Here g_{env} is the g-factor of spins in the local crystalline environment, μ_B is the Bohr magneton, B is the applied field, k is the Boltzmann constant, T is the sample temper-

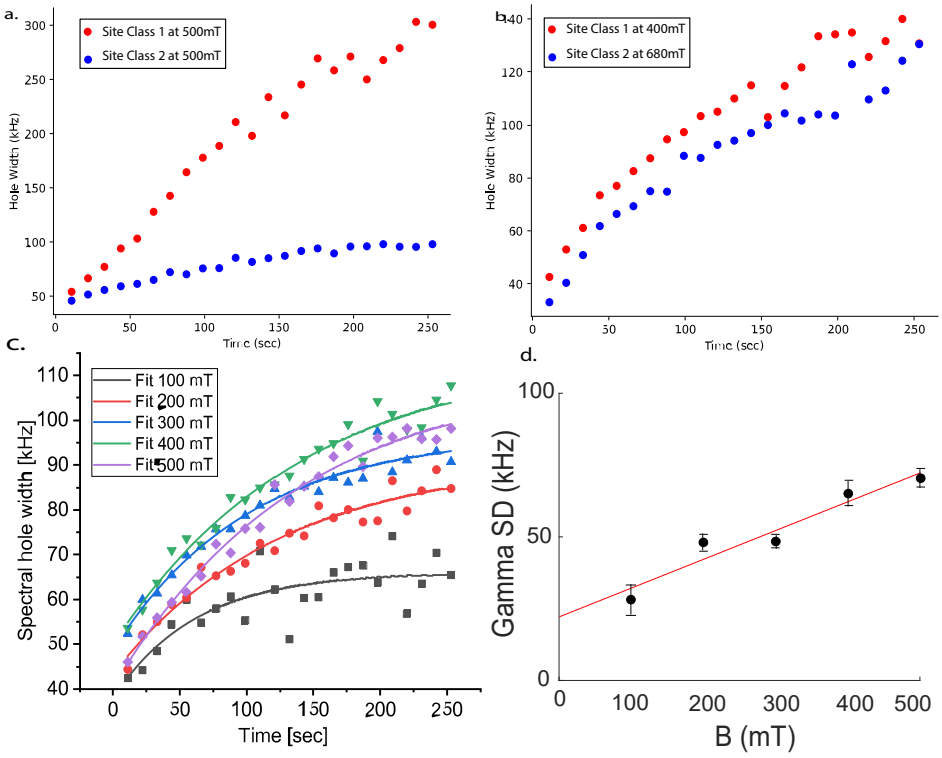

Figure 7.6: **a.** Spectral hole widths for ions in both magnetic classes as a function of time at 500mT. The class of ions with the larger magnetic field projection shows significantly more spectral diffusion. **b.** Spectral hole widths for ions in both magnetic classes as a function of time where the applied magnetic field for each class of ions creates roughly equivalent splitting. The spectral diffusion is comparable **c.** Hole width versus time for a single class of ions at many different magnetic fields. **d.** The fitted Γ_{SD} increases proportionally to the magnetic field.

ature, and $\Gamma_{max}(B)$ is the full width half max of the broadening of the optical transition due to external sources.

For non-Kramer's ions in general, and all atomic species in the YGG host, since the g-factors, g_{env}, are quite small, the thermal distribution of population in various spin levels remains nearly constant for the temperatures and applied fields in this work, making the sech^2 factor effectively constant as well. Any field dependence of Γ_{SD} can then be attributed to the field dependence of $\Gamma_{max}(B)$. As shown in Fig. 7.6 d we find Γ_{SD} to increase as the magnetic field increases while R_s remains fairly constant for the measured fields. Inspired by [20, 43] we fit this behavior using a functional form of $\Gamma_{max}(B)$ that relates the optical transition broadening to the quadratic Zeeman effect.

$$\Gamma_{max}(B) = g_j^2 \mu_B^2 B \cdot |\mathbf{\Lambda_e} - \mathbf{\Lambda_g}| \cdot B_{Noise} + \Gamma_{max}(0). \tag{7.10}$$

Here, g_j is the electron g factor, μ_B the Bohr magneton, $\mathbf{\Lambda}_i$, $i \in \{g, e\}$ is the hyperfine tensor for the ground and excited states in the transition, B is the applied magnetic field,

Species	Concentration	Average distance (r)	Effective g factor	Average Field (B)
$^{169}Tm^{3+}$	1%	17 Å	0.0077	500 nT
^{71}Ga	40%	3 Å	0.00071	10.5 μT
^{69}Ga	60%	3 Å	0.00092	14 μT
^{89}Y	99%	4 Å	0.00014	850 nT

Table 7.1: Magnetic fields experienced by the average Tm ion site from spin flips in the other spins throughout the crystal. Following calculations from [44] and using a model of the YGG crystal cell from [45] we estimate the magnetic field at an average Tm ion site due to spin flips of each host crystal constituent.

and B_{Noise} is a relative small variations in the applied magnetic field from local host spins or external noise. All factors in this expression are known save the empirical B_{Noise}, which is fit to a value of 120 μT .

Table 7.1 contains estimated magnetic fields at a potential Tm ion site due to spin flips from each of the possible crystal constituents. All fields are smaller by at least an order of magnitude than the projected noise, leading us to conclude that it is largely caused by our measured solenoid supply noise. An order of magnitude less supply noise is likely to reveal effects of a bath of local gallium spin flips.

7.9. CONCLUSION

We conducted a series of spectroscopic measurements that leads to a detailed understanding of how to create high-resolution spectral features using Tm:YGG. The possibility for controlling pump field amplitude, frequency chirp, pulse duration, and pulse power give a number of experimental handles with which to optimize the shape of the desired spectral feature. Experimental results were shown to be in good agreement with predictions from a three level, frequency dependent, rate equation model for any given set of input pulses shorter than the transition lifetime. However, when applying the same model to a three level system that includes a ground state spin level split by magnetic field, magnetic noise, and spectral diffusion dominate the resulting features over long timescales. The quadratic Zeeman effect in combination with time varying magnetic fields was shown to create large shifts to each ions optical transition frequency as the likely cause of the diffusion. This in depth analysis will aid applications that employ spectral features created using Tm:YGG such as spectral hole-based laser stabilization, RF frequency analysis, and optical quantum memories.

7.10. SUPPLEMENTARY MATERIAL

7.10.1. MORE EXAMPLES OF DIFFERENT BURNING SEQUENCES

In the main text we show examples of modeled and experimentally created spectral holes using a single burning process. However the good agreement between these two methods extends to a large variety of create procedures. We measured holes created using burn pulses with 5 different optical powers, with 2 different durations, and 4 different

waiting times giving us more than 40 individual experiments with which to match behavior and predictions.

7.10.2. HOLES AND LEVEL LIFETIMES

Some examples of the previous section showcase the behavior of spectral holes relative to the different level lifetimes. They are worth a deeper look. We measure only a pair of burning times, 100us and 1ms, as burning pulses longer than around 1 ms or so were observed to heat the crystal. For burning pulses of each length we examine a set of different waiting times between the pulses of the sequence from Fig 7.3 a : 1ms,10ms, 50ms, and 100ms. Each is selected for a reason. One millisecond is on the order of the the excited state lifetime and much shorter than the bottleneck lifetime. Ten milliseconds is much longer than the excited lifetime and much shorter than the bottleneck lifetime. Fifty milliseconds is much longer than the excited and on the same order as the bottleneck lifetime, and 100ms is much longer than both lifetimes.

As the waiting time approaches the bottleneck level lifetime the additive nature of multiple burn pulses start to disappear and the hole depth reaches a much smaller steady state. When the waiting time exceeds the bottleneck lifetime we are essentially re-pumping the same population with each burn pulse, interacting with a nearly unchanged material absorption profile. For waiting times on the order of the excited state lifetime, we see a slight broadening of the hole due to power broadening as well as due to the potential for frequency shifts caused by excited ions within the pump bandwidth [18, 35]. This indicates that the optimum wait duration with which to create features is longer than the excited state lifetime so that most pumping occurs without population in the excited state, but still much shorter than the bottleneck level lifetime to allow population to accumulate in the bottleneck over many successive burning pulses.

7.10.3. POWER DEPENDENCE DUE TO MODEL NON-LINEARITY

Of the many measured data sets, a key portion involves the same optical pumping sequence with a series of different optical powers. This tuning is done by changing the peak to peak amplitude of the AOM driving signal over a range of voltages. Different initial laser line-shapes, $R(\Delta)$ with different amplitudes broaden the resulting holes at different rates. This study allowed us to determine the spectral shape of our applied $R(\Delta)$ function by comparing measured results to the scaling predicted by our model. First we show a series of hole burning experiments conducted with different optical powers using our un-modulated laser. The clear broadening of the spectral hole is not power broadening as in [15] but rather an effect due to the Lorentzian shape of the applied laser line. With increased amplitude the wings of the Lorentzian shape gain the ability to efficiently change ground state population, broadening the resulting hole. Additionally we show the scaling of a spectral hole for hyperbolic secant modulated pulses using a burning sequence with matching timing as above. As seen from figure 7.7 b, the broadening is nearly absent because the pulse modulation reshapes the applied $R(\Delta)$ function into a square shape that does not possess wings that strengthen with added burning power. This is the more desirable scaling, so that added power results in a higher excitation rate and deeper rather than broader spectral holes.

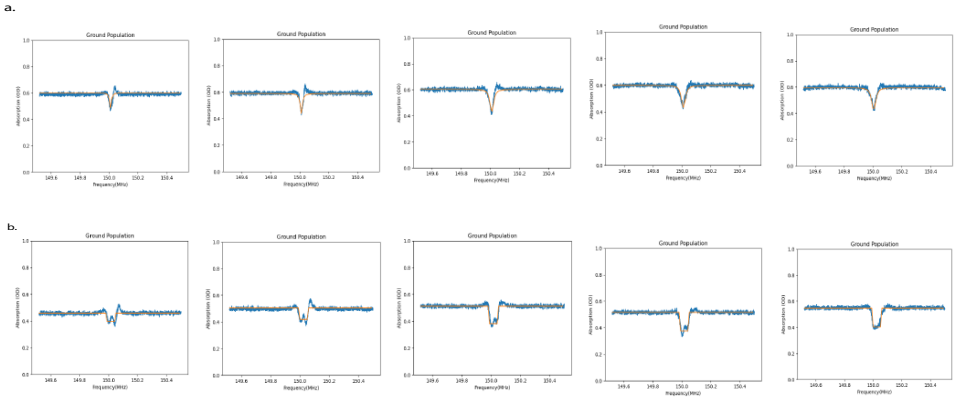

Figure 7.7: **a.** A series of spectral holes after 50 cycles of 1 ms burning and 50ms waiting between at five linearly increasing optical powers. **b.** A similar experiment, but each burn pulse is a hyperbolic secant pulse.

BIBLIOGRAPHY

[1] W. R. Babbitt et al., "From spectral holeburning memory to spatial-spectral microwave signal processing", Laser Physics **24**, 094002 (2014).

[2] W. Tittel, M. Afzelius, T. Chaneliére, R. Cone, S. Kröll, S. Moiseev, and M. Sellars, "Photon-echo quantum memory in solid state systems", Laser & Photonics Reviews **4**, 244–267 (2010).

[3] P. B. Sellin, N. M. Strickland, J. L. Carlsten, and R. L. Cone, "Programmable frequency reference for subkilohertz laser stabilization by use of persistent spectral hole burning", Opt. Lett. **24**, 1038–1040 (1999).

[4] P. B. Sellin, N. M. Strickland, T. Böttger, J. L. Carlsten, and R. L. Cone, "Laser stabilization at 1536 nm using regenerative spectral hole burning", Phys. Rev. B **63**, 155111 (2001).

[5] M. Colice, F. Schlottau, K. Wagner, R. K. Mohan, W. R. Babbitt, I. Lorgere, and J.-L. L. Gouet, "RF spectrum analysis in spectral hole burning media", in Optical information systems ii, Vol. 5557, edited by B. Javidi and D. Psaltis (International Society for Optics and Photonics, 2004), pp. 132–139.

[6] P. Berger, Y. Attal, M. Schwarz, S. Molin, A. Louchet-Chauvet, T. Chanelière, J.-L. L. Gouët, D. Dolfi, and L. Morvan, "Rf spectrum analyzer for pulsed signals: ultra-wide instantaneous bandwidth, high sensitivity, and high time-resolution", J. Lightwave Technol. **34**, 4658–4663 (2016).

[7] F. Bussières, C. Clausen, I. Usmani, A. Tiranov, N. Sangouard, H. de Riedmatten, M. Afzelius, and N. Gisin, "Quantum memories with rare-earth-ion doped crystals", in 2013 conference on lasers and electro-optics pacific rim (2013), MG2$_2$.

[8] A. Kinos et al., *Roadmap for rare-earth quantum computing*, 2021.

[9] M. F. Askarani et al., "Long-lived solid-state optical memory for high-rate quantum repeaters", Phys. Rev. Lett. **127**, 220502 (2021).

[10] C. W. Thiel, N. Sinclair, W. Tittel, and R. L. Cone, "Optical decoherence studies of Tm^{3+} : $Y_3Ga_5O_{12}$", Phys. Rev. B **90**, 214301 (2014).

[11] C. W. Thiel, N. Sinclair, W. Tittel, and R. L. Cone, "Tm^{3+} : $Y_3Ga_5O_{12}$ Materials for spectrally multiplexed quantum memories", Phys. Rev. Lett. **113**, 160501 (2014).

[12] R. MacFarlane, C. Yannoni, and R. Shelby, "Optical line narrowing by nuclear spin decoupling in pr3+: laf3", Optics Communications **32**, 101–104 (1980).

[13] C. Thiel, T. Böttger, and R. Cone, "Rare-earth-doped materials for applications in quantum information storage and signal processing", Journal of Luminescence **131**, Selected papers from DPC'10, 353–361 (2011).

[14] W. Moerner et al., *Persistent spectral hole-burning: science and applications*, Topics in Current Physics (Springer Berlin Heidelberg, 1988).

[15] L. Allen and J. Eberly, *Optical resonance and two-level atoms*, Dover Books on Physics (Dover Publications, 2012).

[16] M. Bonarota, J. Ruggiero, J. .-. L. Gouët, and T. Chanelière, "Efficiency optimization for atomic frequency comb storage", Phys. Rev. A **81**, 033803 (2010).

[17] P. Jobez, N. Timoney, C. Laplane, J. Etesse, A. Ferrier, P. Goldner, N. Gisin, and M. Afzelius, "Towards highly multimode optical quantum memory for quantum repeaters", Phys. Rev. A **93**, 032327 (2016).

[18] L. Rippe, M. Nilsson, S. Kröll, R. Klieber, and D. Suter, "Experimental demonstration of efficient and selective population transfer and qubit distillation in a rare-earth-metal-ion-doped crystal", Phys. Rev. A **71**, 062328 (2005).

[19] L. Veissier, C. W. Thiel, T. Lutz, P. E. Barclay, W. Tittel, and R. L. Cone, "Quadratic zeeman effect and spin-lattice relaxation of Tm^{3+}:yag at high magnetic fields", Phys. Rev. B **94**, 205133 (2016).

[20] T. Böttger, C. W. Thiel, Y. Sun, and R. L. Cone, "Optical decoherence and spectral diffusion at 1.5 μm in $Er^{3+}:Y_2SiO_5$ versus magnetic field, temperature, and Er^{3+} concentration", Phys. Rev. B **73**, 075101 (2006).

[21] C. W. Thiel, N. Sinclair, W. Tittel, and R. L. Cone, "Optical decoherence studies of $Tm^{3+}:Y_3Ga_5O_{12}$", Phys. Rev. B **90**, 214301 (2014).

[22] E. D. Black, "An introduction to pound–drever–hall laser frequency stabilization", American Journal of Physics **69**, 79–87 (2001).

[23] J. H. Davidson, *Custom python scripts available on git hub*, 2021.

[24] J. F. Dillon and L. R. Walker, "Ferrimagnetic resonance in rare-earth doped yttrium iron garnet. ii. terbium substitution", Phys. Rev. **124**, 1401–1413 (1961).

[25] G. Menzer, "Xx. die kristallstruktur der granate", Zeitschrift für Kristallographie - Crystalline Materials **69**, 300–396 (01 Dec. 1929).

[26] Y. C. Sun, "Rare earth materiais in optical storage and data processing applications", in *Spectroscopic properties of rare earths in optical materials*, edited by R. Hull, J. Parisi, R. M. Osgood, H. Warlimont, G. Liu, and B. Jacquier (Springer Berlin Heidelberg, Berlin, Heidelberg, 2005), pp. 379–429.

[27] J. H. Davidson et al., "Measurement of the thulium ion spin hamiltonian in an yttrium gallium garnet host crystal", Phys. Rev. B **104**, 134103 (2021).

[28] R. Lauro, T. Chanelière, and J. L. L. Gouët, "Slow light using spectral hole burning in a tm3+: yag crystal", arXiv preprint arXiv:0902.2657 (2009).

[29] A. Louchet, J. S. Habib, V. Crozatier, I. Lorgeré, F. Goldfarb, F. Bretenaker, J.-L. L. Gouët, O. Guillot-Noël, and P. Goldner, "Branching ratio measurement of a Λ system in Tm^{3+} : YAG under a magnetic field", Phys. Rev. B **75**, 035131 (2007).

[30] Y. Sun, G. M. Wang, R. L. Cone, R. W. Equall, and M. J. M. Leask, "Symmetry considerations regarding light propagation and light polarization for coherent interactions with ions in crystals", Phys. Rev. B **62**, 15443–15451 (2000).

[31] H. Linget, T. Chanelière, J.-L. Le Gouët, P. Berger, L. Morvan, and A. Louchet-Chauvet, "Interlaced spin grating for optical wave filtering", Phys. Rev. A **91**, 023804 (2015).

[32] M. S. Silver, R. I. Joseph, and D. I. Hoult, "Selective spin inversion in nuclear magnetic resonance and coherent optics through an exact solution of the bloch-riccati equation", Phys. Rev. A **31**, 2753–2755 (1985).

[33] F. T. Hioe, "Solution of bloch equations involving amplitude and frequency modulations", Phys. Rev. A **30**, 2100–2103 (1984).

[34] M. Tian, T. Chang, K. D. Merkel, and W. Randall, "Reconfiguration of spectral absorption features using a frequency-chirped laser pulse", Appl. Opt. **50**, 6548–6554 (2011).

[35] I. Roos and K. Mølmer, "Quantum computing with an inhomogeneously broadened ensemble of ions: suppression of errors from detuning variations by specially adapted pulses and coherent population trapping", Phys. Rev. A **69**, 022321 (2004).

[36] L. Johnson and C. Cox, "Serrodyne optical frequency translation with high sideband suppression", Journal of Lightwave Technology **6**, 109–112 (1988).

[37] E. Saglamyurek, N. Sinclair, J. A. Slater, K. Heshami, D. Oblak, and W. Tittel, "An integrated processor for photonic quantum states using a broadband light–matter interface", **16**, 065019 (2014).

[38] C. W. Thiel, R. M. Macfarlane, Y. Sun, T. Böttger, N. Sinclair, W. Tittel, and R. L. Cone, "Measuring and analyzing excitation-induced decoherence in rare-earth-doped optical materials", Laser Physics **24**, 106002 (2014).

[39] Y. Sun, C. W. Thiel, and R. L. Cone, "Optical decoherence and energy level structure of 0.1% tm^{3+}:$linbo_3$", Phys. Rev. B **85**, 165106 (2012).

[40] J. R. Klauder and P. W. Anderson, "Spectral diffusion decay in spin resonance experiments", Phys. Rev. **125**, 912–932 (1962).

[41] W. B. Mims, "Phase memory in electron spin echoes, lattice relaxation effects in $cawO_4$: er, ce, mn", Phys. Rev. **168**, 370–389 (1968).

[42] R. M. Macfarlane, "Photon-echo measurements on the trivalent thulium ion", Opt. Lett. **18**, 1958–1960 (1993).

[43] T. Lutz, L. Veissier, C. W. Thiel, R. L. Cone, P. E. Barclay, and W. Tittel, "Modification of phonon processes in nanostructured rare-earth-ion-doped crystals", Phys. Rev. A **94**, 013801 (2016).

[44] T. Böttger, "Laser frequency stabilization to spectral hole burning frequency references in erbium-doped crystals: material and device optimization", PhD thesis (Apr. 2002).

[45] K. Persson, *Materials data on y3ga5o12 (sg:230) by materials project*, An optional note, July 2014.

8

Conclusions and Outlook

Why didn't the astronaut brush his teeth? ... They were already experiencing zero cavity.

In this chapter summarize the results of this thesis. This is followed by a brief discussion of the immediate research questions raised by this work, and the proposal of some interesting future studies. Finally, I conclude with some remarks on this work's impact on the study of thulium doped garnets, optical quantum memories, and frequency multiplexed quantum repeaters.

8.1. SUMMARY OF RESULTS

This thesis describes progress in creating and improving optical quantum memories using thulium doped garnets for use in frequency multiplexed quantum repeaters. In particular, it focuses on improvements to memory recall efficiency, and storage time.

- **Chapter** 3, shows a quantum memory with improved storage efficiency of up to 27% that is capable of high fidelity qubit storage. It exploits a Tm:YAG inside a monolithic impedance matched cavity memory. Quantum state storage is demonstrated using weak coherent pulses and heralded single photons. These results show a route to high-efficiency quantum memories based on impedance matched AFC devices using thulium atoms.
- In **chapter** 4, I show storage of classical pulses for long storage times up to 100 μs, simultaneous storage of pulses at multiple frequencies, as well as proof-of-principle shifting and filtering for frequency multiplexed quantum repeaters using a Tm:YGG optical memory. These results show the promise of thulium doped garnet materials for frequency multiplexed quantum repeaters.
- In **chapter** 5, I measure the optical properties of YGG material by way of variable-angle spectroscopic ellipsometry and determine a process for creating thin film mirrors directly on the crystal. These results forward our ability to create high precision optical cavities out of Tm:YGG for impedance matched AFC quantum memories.
- In **chapter** 6, I conduct measurements of the hyperfine tensors of the $^3H_4$ and $^3H_6$ states of Tm:YGG using a combination of ODNMR, spectral hole burning, and absorption spectroscopy. The results of these measurements confirm the site structure of this material, determine the level splittings for all orientations, and reveal the presence of optical clock transitions.
- In **chapter** 7, I conduct an in-depth study matching numerical solutions of frequency dependent rate equations to our optical pumping process to further understand how to create high resolution spectral features in Tm:YGG. The modeling of this chapter provides a recipe for burning well understood spectral features and improved AFC quantum memories in this material.

In the following sections, I propose some deeper questions for study which show immediate promise based on the results of the work described above. Additionally, I discuss the implications of this work in the field of optical quantum memory, rare earth ion doped materials, and frequency multiplexed quantum repeaters.

8.2. IMMEDIATE QUESTIONS FOR FURTHER STUDY

We have seen studies ranging from quantum memory demonstrations to detailed study of magnetic properties of Tm ions in YGG. Each of these studies reveals avenues through which we can learn more and build upon the results of this thesis. Some of these questions and the studies to answer them are proposed below in relation to the work of each chapter.

8.2.1. CHAPTER 3

Will there be an upper limit to the storage efficiency in impedance matched cavities due to other effects such as temporal photon shape [1]? Additionally, the only way to push this system to unit efficiency is through the use of high finesse AFC memories. To meet the impedance matched condition for higher finesse AFC structures the cavity must also become higher finesse (Less intra-cavity loss must be matched by less mirror reflectivity loss) [2]. Depending on cavity design and mode volume the impedance matched regime may begin to approach the world of Purcell enhancement and strongly coupled cavities [3]. Will a resulting trade-off be created between memory storage time and improved efficiency as the devices approach this regime? More studies, similar to [4, 5], probing use of rare earths coupled to high finesse cavities as memories have potential to find the answer.

8.2.2. CHAPTER 4

The results of chapter 4 represent some of the longest storage for light using only optical coherence. The questions raised in the work itself of how to improve the memory to match the decay constant limit imposed by coherence time of the optical transition.

8.2.3. CHAPTER 5

All nano fabrication using rare earth doped materials builds a library of standard recipes required for moving this technology from bulk crystals to on-chip [6]. Likewise, this mirror fabrication recipe could yield a number of different improvements for future designs possibly including impedance matched cavities on chip. Firstly, can the mirrors be improved by deposition of more single-crystalline films by processes such as chemical vapor deposition? Additionally, actively controlling the index of the silicon nitride layers during deposition would allow controlling the reflection bandwidth of a particular layer stack [7]. A study building upon initial results from this chapter could delve into many of the process parameters that we did not explore in this work to optimise and control the mirror design giving precise control to impedance matched cavity designs in future.

8.2.4. CHAPTER 6

Does the use of an optical clock transition allow further improvement of the optical coherence time T2 reported in chapter 4? Additionally, can the coupling to the gallium atoms that was visible throughout the ODNMR results be further controlled to yield a useful resource in this material such as a local qubit register similar to [8]? To delve deeper, through use of a neutron beam scattering, one could probe fundamental physics to further separate the individual factors within the ion structure that lead to the measured splittings [9].

8.2.5. CHAPTER 7

Can the measured spectral diffusion be improved with the addition of RF pulse sequences, or by moving to a clock orientations from chapter 6? With the ability to create adiabatic pulses over bandwidths available using separate optical elements is there also the possibility to modulate the spectral shape of heralded single photons for more efficient packing of spectral modes in frequency multiplexed quantum repeaters? Could it also be

possible to control pump pulses routed to non-linear crystals for SPDC to further tailor the resulting spectral shape of the generated photons?

8.3. APPLICATIONS OF THULIUM GARNETS

Rare earths are employed in a number of different technologies today [10–16]. Experimental studies such as those presented in this thesis help to form a library of properties based on which one can create real technological advances. Spectroscopy of thulium doped devices will always have interest to further the goals of these exciting technologies.

One route which shows promise is further examination of the $^3F_4$ bottleneck level which has a fairly long lifetime in YGG hosts [17, 18]. This state could make an interesting additional level for optical studies because it includes transitions in the ~1400 nm and ~1800 nm range and presents an interesting opportunity for a telecom frequency transition in rare earth doped materials.

Thulium doped garnets in particular remain some of the most promising materials for these purposes because of the long optical coherence times and easily accessible optical transitions, within range of commercial laser diodes and biological tissue transparency [19–21]. Its simple level structure compared to other rare earths makes use of Tm ions straightforward for developing useful technologies.

The only drawback to garnets is that they will always be affected by the crystalline spin environment from the additional species that makes up the crystal, be it aluminum, gallium, iron or other. These spins may affect many of the use cases of these crystals. However, they can also become a resource if used correctly [8, 22]. Note that, alongside the common Czochralski growth method there is also the possibility to deposit garnets via nano fabrication processes [23, 24]. With the inclusion of rare earths, this process could lead to on chip devices with properties akin to those of the bulk samples used in this work.

8

8.4. THULIUM GARNETS AS OPTICAL QUANTUM MEMORIES

In terms of the specific goal of two level AFC quantum memories, Tm doped garnets are one of the most attractive candidates. In the immediate term there are a number of avenues for improvement of our particular quantum memories. The first is the addition of microwave control to our experimental setup. With added microwaves we gain added control of the spin population in our samples [25, 26]. With short RF pulses of the appropriate frequency and magnitude, we can target different ensembles of ions within the crystal and initialize population on a smaller timescale compared to the long optical lifetimes in these materials. There may indeed be techniques that improve two level optical AFC storage using RF pulses applied to the spin transition to maintain good optical coherence[25].

A second key improvement is improved magnetic field stability and magnetic shielding of our cryostat. Measurements of chapter 7 show high sensitivity to magnetic noise for our atomic ensemble. Estimating the effect from our knowledge of magnetic tensors (See chapter 6) shows that we are likely sensitive on the μT scale. Another key step in extending storage times is increased laser stability. Though we can create square exci-

tation profiles from Lorentzian linewidths, the Lorentzian laser line is still the ultimate lower bound for the width of these features. With improved control, both of the magnetic field and laser frequency, capabilities of our memories will certainly continue to improve alongside correctly designed impedance matched cavities.

Considering another perspective, in the field of quantum information we must be concerned not only with fundamental limits to performance but also the scaling that it will take to achieve useful technology. For the case of Tm doped garnet materials, scaling presents a complex challenge that must still be solved. For thulium ions, many of the parameters necessary for improvement and tuning of the memory performance are coupled together by the only method for experimental control, an external magnetic field. Since there are only non-degenerate hyperfine levels with an applied magnetic field, all lifetimes and coherence properties, as well as spectral diffusion mechanisms are controlled by this single experimental parameter. If that parameter is optimized for one purpose, then the effects across all the other dependent variables must be dealt with on an ever increasing scale as more memory channels are added.

Consider the case discussed in chapter 7 of spectral diffusion in Tm:YGG. The bottleneck level lifetime increases with applied magnetic field and the created splitting of the ground state spin levels. A long spin-level lifetime, one of the most attractive features of REIC systems [27, 28], is essential because it improves our ability to craft high quality spectral features for long storage times. However, spectral diffusion in this material also scales directly with magnetic field in this material, resulting in a trade-off. To further complicate matters, for high efficiency or high-bandwidth storage, both necessary properties of two level AFC quantum memories, high magnetic fields are needed to create AFC structures of the large bandwidth or high finesse. In the short term, there are certainly compromises between these many trade-offs that allow for progress. However, with so many degrees of freedom coupling to a single control mechanism, optimization of all parameters at the scale required for a functional quantum network may eventually prove untenable unless methods of isolating the different dependencies can be developed.

8.5. OUTLOOK FOR FREQUENCY MULTIPLEXED QUANTUM REPEATERS

This thesis focuses on optical quantum memory and allows some informed comments on the state of frequency-multiplexed quantum repeaters. It builds upon an existing argument that frequency multiplexing represents a valuable route to high rate entanglement generation over long distances [29, 30]. Multiplexing across many possible degrees of freedom, including frequency, will be required to counter the effects of loss with distance. However, it appears unlikely that any single degree of freedom for multiplexing alone will allow achieving useful entanglement generation rates. The number of modes required to overcome transmission loss, many potentially lossy devices, and inefficient entanglement swapping measurements means that quantum repeaters will need to rely on every available mode to produce a sufficient rate for applications.

In this light, it is important to examine the costs of adding temporal multiplexing as well. The entanglement generation rate then depends on the rate at which entanglement

sources can generate photon pairs, the bandwidth of the memories, and duty cycle constraints of procedures like spin level transfer pulses and non-experimental periods to stabilize lasers or interferometers. Experiments that take advantage of temporal multiplexing are currently the state of the art and have produced the fastest entanglement generation rates over distance at the time of writing. This was shown with 62 temporal modes producing an entanglement rate of 1.4 kHz over 50 meters for an experimental setup approximating an elementary link[31].

While there have been no demonstrations of frequency multiplexing for a full elementary link, quantum storage with up to 28 frequency modes has been reported [29]. Similar results for longer storage times over 10 simultaneous frequency modes were shown in chapter 4. Other devices required for full frequency multiplexed quantum repeaters such as frequency multiplex sources, and frequency resolved Bell state measurements are progressing as well [32–35]. Current demonstrations have all been carried out with modes spaced within the range of a single electro-optic modulator bandwidth over a few GHz. This capacity is far from the ultimate limit for modes that can be captured within the inhomogeneous broadening of many REIC materials, thulium doped garnets included. Finding effective methods for scaling up to these material limits remains a key goal for the spectral multiplexing.

Both strategies can lead to rate increases so combining both will prove valuable pursuits in scaling towards high rate entanglement generation [30, 36]. A better question than which degree of freedom to choose for multiplexing is how best to integrate them to make the most of the available bandwidth in time-frequency space. Any viable method for dividing all available bandwidth will lead to the highest possible distribution rate.

8.6. GENERAL IMPACT

Rare earth ion doped crystals, and in particular thulium doped garnets, hold great promise as a platform for establishing interesting classical and quantum technology. As quantum memories, we have found their particular niche and continue to improve their parameters. As a component of other devices, further understanding and spectroscopy continues to improve existing technology.

In the coming years, we expect to see quantum networks that transmit quantum information over large distances. This thesis, although it only covers a small part of the required components adds to the development of quantum communication and computing technology. We have always lived in a quantum world, but this fact is on the verge of being thrown front and center, for all to benefit from the changes that quantum information technology promises to create in our world.

BIBLIOGRAPHY

[1] C. Liu, Y. Sun, L. Zhao, S. Zhang, M. M. T. Loy, and S. Du, "Efficiently loading a single photon into a single-sided fabry-perot cavity", Phys. Rev. Lett. **113**, 133601 (2014).

[2] M. Afzelius and C. Simon, "Impedance-matched cavity quantum memory", Phys. Rev. A **82**, 022310 (2010).

[3] E. M. Purcell, H. C. Torrey, and R. V. Pound, "Resonance absorption by nuclear magnetic moments in a solid", Phys. Rev. **69**, 37–38 (1946).

[4] T. Zhong et al., "Nanophotonic rare-earth quantum memory with optically controlled retrieval", Science **357**, 1392–1395 (2017).

[5] I. Craiciu, M. Lei, J. Rochman, J. G. Bartholomew, and A. Faraon, "Multifunctional on-chip storage at telecommunication wavelength for quantum networks", Optica **8**, 114–121 (2021).

[6] J. G. Bartholomew, J. Rochman, J. M. Kindem, A. Ruskuc, I. Craiciu, M. Lei, T. Zhong, and A. Faraon, "Coherent control of rare-earth ions in on-chip devices for microwave-to-optical transduction", in Conference on lasers and electro-optics (2019), FM1A.6.

[7] D. K. T. Ng, Q. Wang, T. Wang, S.-K. Ng, Y.-T. Toh, K.-P. Lim, Y. Yang, and D. T. H. Tan, "Exploring high refractive index silicon-rich nitride films by low-temperature inductively coupled plasma chemical vapor deposition and applications for integrated waveguides", ACS Applied Materials & Interfaces **7**, 21884–21889 (2015).

[8] A. Ruskuc, C.-J. Wu, J. Rochman, J. Choi, and A. Faraon, *Nuclear spin-wave quantum register for a solid state qubit*, 2021.

[9] A. Abragam and B. Bleaney, "Enhanced nuclear magnetism: some novel features and prospective experiments", Proceedings of the Royal Society of London. Series A, Mathematical and Physical Sciences **387**, 221–256 (1983).

[10] P. B. Sellin, N. M. Strickland, J. L. Carlsten, and R. L. Cone, "Programmable frequency reference for subkilohertz laser stabilization by use of persistent spectral hole burning", Opt. Lett. **24**, 1038–1040 (1999).

[11] P. B. Sellin, N. M. Strickland, T. Böttger, J. L. Carlsten, and R. L. Cone, "Laser stabilization at 1536 nm using regenerative spectral hole burning", Phys. Rev. B **63**, 155111 (2001).

[12] M. Colice, F. Schlottau, K. Wagner, R. K. Mohan, W. R. Babbitt, I. Lorgere, and J.-L. L. Gouet, "RF spectrum analysis in spectral hole burning media", in Optical information systems ii, Vol. 5557, edited by B. Javidi and D. Psaltis (International Society for Optics and Photonics, 2004), pp. 132–139.

[13] P. Berger, Y. Attal, M. Schwarz, S. Molin, A. Louchet-Chauvet, T. Chanelière, J.-L. L. Gouët, D. Dolfi, and L. Morvan, "Rf spectrum analyzer for pulsed signals: ultra-wide instantaneous bandwidth, high sensitivity, and high time-resolution", J. Lightwave Technol. **34**, 4658–4663 (2016).

[14] W. Tittel, M. Afzelius, T. Chaneliére, R. Cone, S. Kröll, S. Moiseev, and M. Sellars, "Photon-echo quantum memory in solid state systems", Laser & Photonics Reviews **4**, 244–267 (2010).

[15] F. Bussières, C. Clausen, I. Usmani, A. Tiranov, N. Sangouard, H. de Riedmatten, M. Afzelius, and N. Gisin, "Quantum memories with rare-earth-ion doped crystals", in 2013 conference on lasers and electro-optics pacific rim (2013), MG2$_2$.

[16] A. Kinos et al., *Roadmap for rare-earth quantum computing*, 2021.

[17] M. F. Askarani et al., "Long-lived solid-state optical memory for high-rate quantum repeaters", Phys. Rev. Lett. **127**, 220502 (2021).

[18] C. W. Thiel, N. Sinclair, W. Tittel, and R. L. Cone, "Optical decoherence studies of Tm^{3+} : $Y_3Ga_5O_{12}$", Phys. Rev. B **90**, 214301 (2014).

[19] C. Venet, M. Bocoum, J.-B. Laudereau, T. Chaneliere, F. Ramaz, and A. Louchet-Chauvet, "Ultrasound-modulated optical tomography in scattering media: flux filtering based on persistent spectral hole burning in the optical diagnosis window", Opt. Lett. **43**, 3993–3996 (2018).

[20] Y. Li, H. Zhang, C. Kim, K. H. Wagner, P. Hemmer, and L. V. Wang, "Pulsed ultrasound-modulated optical tomography using spectral-hole burning as a narrowband spectral filter", Applied Physics Letters **93**, 011111 (2008).

[21] C. Venet, B. Car, L. Veissier, F. Ramaz, and A. Louchet-Chauvet, "Deep and persistent spectral holes in thulium-doped yttrium orthosilicate for imaging applications", Phys. Rev. B **99**, 115102 (2019).

[22] C. E. Bradley, J. Randall, M. H. Abobeih, R. C. Berrevoets, M. J. Degen, M. A. Bakker, M. Markham, D. J. Twitchen, and T. H. Taminiau, "A ten-qubit solid-state spin register with quantum memory up to one minute", Phys. Rev. X **9**, 031045 (2019).

[23] E. Sawatzky and E. Kay, "Preparation of garnet films by sputtering", Journal of Applied Physics **39**, 4700–4706 (1968).

[24] J. E. Mee, J. L. Archer, R. H. Meade, and T. N. Hamilton, "Chemical vapor deposition of epitaxial yig on yag and epitaxial gdig on yag", Applied Physics Letters **10**, 289–291 (1967).

[25] R. Lauro, T. Chanelière, and J.-L. Le Gouët, "Adiabatic refocusing of nuclear spins in tm^{3+}:yag", Phys. Rev. B **83**, 035124 (2011).

[26] M. F. Pascual-Winter, R.-C. Tongning, T. Chanelière, and J.-L. Le Gouët, "Spin coherence lifetime extension in tm^{3+}:yag through dynamical decoupling", Phys. Rev. B **86**, 184301 (2012).

[27] Y. C. Sun, "Rare earth materiais in optical storage and data processing applications", in *Spectroscopic properties of rare earths in optical materials*, edited by R. Hull, J. Parisi, R. M. Osgood, H. Warlimont, G. Liu, and B. Jacquier (Springer Berlin Heidelberg, Berlin, Heidelberg, 2005), pp. 379–429.

[28] A. Kaplyanskii and R. McFarlane, *Spectroscopy of crystals containing rare earth ions* (Elsevier, 2012).

[29] N. Sinclair et al., "Spectral multiplexing for scalable quantum photonics using an atomic frequency comb quantum memory and feed-forward control", Phys. Rev. Lett. **113**, 053603 (2014).

[30] S. Guha, H. Krovi, C. A. Fuchs, Z. Dutton, J. A. Slater, C. Simon, and W. Tittel, "Rate-loss analysis of an efficient quantum repeater architecture", Phys. Rev. A **92**, 022357 (2015).

[31] D. Lago-Rivera, S. Grandi, J. V. Rakonjac, A. Seri, and H. de Riedmatten, "Telecom-heralded entanglement between multimode solid-state quantum memories", Nature **594**, 37–40 (2021).

[32] R. Ikuta, R. Tani, M. Ishizaki, S. Miki, M. Yabuno, H. Terai, N. Imoto, and T. Yamamoto, "Frequency-multiplexed photon pairs over 1000 modes from a quadratic nonlinear optical waveguide resonator with a singly resonant configuration", Phys. Rev. Lett. **123**, 193603 (2019).

[33] A. Seri, D. Lago-Rivera, A. Lenhard, G. Corrielli, R. Osellame, M. Mazzera, and H. de Riedmatten, "Quantum storage of frequency-multiplexed heralded single photons", Phys. Rev. Lett. **123**, 080502 (2019).

[34] M. Grimau Puigibert, G. H. Aguilar, Q. Zhou, F. Marsili, M. D. Shaw, V. B. Verma, S. W. Nam, D. Oblak, and W. Tittel, "Heralded single photons based on spectral multiplexing and feed-forward control", Phys. Rev. Lett. **119**, 083601 (2017).

[35] N. B. Lingaraju, H.-H. Lu, D. E. Leaird, S. Estrella, J. M. Lukens, and A. M. Weiner, *Bell state analyzer for spectrally distinct photons*, 2021.

[36] C. Simon, H. de Riedmatten, M. Afzelius, N. Sangouard, H. Zbinden, and N. Gisin, "Quantum repeaters with photon pair sources and multimode memories", Phys. Rev. Lett. **98**, 190503 (2007).

ACKNOWLEDGEMENTS

First of all I want to thank you, the reader, for sticking with me so far. I'm sure a this thesis can be a grueling read, and I appreciate you for sticking with it. Now comes the part where I thank everyone else who helped to produce this work because there is no way on earth that I could have done this alone. My PhD has come in many distinct phases each teaching me more than the last while on the way to pursue this crazy goal.

My PhD started with a stint working abroad in a lab that was familiar but with the beginning of a new culture growing around me. **Daniel** I would like to thank you for taking a chance on me for on those first few months of my degree. I was certainly not capable of doing everything I am now and without your input and help I would not have been able to do that first cavity experiment. You also brought in a lovable cast of fellows to help and work with in those early months. **YanJuan** it was always a pleasure having you around to chat with, I hope all is well in Ontario. **Sarvin** you have become a great friend and I hope we get to go to another Quiz shoe soon! **Jun** You were a motivated and excellent postdoc during the beginning of this PhD, and I was always amazed by how quickly we learned from and taught each other during those few months. **Pascal** you were there during my masters, but our game nights (and afternoons) in the lab were always of highlight of my stay. **Hridya** that chunk of time was the start of our multi-continental friendship, and hope I get the chance to come visit you in India. I hope you are well. Finally, **Shahrzad** we have never met in person, but you are a good friend and researcher and I look forward to the day when we get the chance. You are all amazing connections that I am luck to have had the chance to experience.

The second time I ventured abroad actually turned out to be a trap. In March 2020 on the way to the APS meeting all hell broke loose in the world and I was left scrambling. I was taken in by one of the kindest groups that I have had the experience to work with. **Rufus** and **Charles** thank you for your immediate and generous response at the beginning of COVID when it was unclear how easy it would be to get back to Europe. You truly made everything work out for the best at such a chaotic time. **Aaron** and **Tino** you two were essential to life in Bozeman. I learned how to function in that lab from you two, and without both of your help there is no way we would have succeeded in our measurements. I hope life post PhD is treating you both well. **Adam** and **Tom** I will never forget any of our in depth discussions or the surprise pizza while the experiment was running. We picked the best day to hit the great one. Finally **Kyle** I hope we keep running into each other all over the world. You are a good friend, and whether we are in the Alps or the Bridgers, I hope we find some good tracks.

Visits to other labs aside, I am a Delft Student and there is no way that I could have accomplished this without all of the amazing people here. To all of those who I have worked with around Qutech: **Seebe**, **Remco**, **Roy**, **Raymond**, **Olaf**, **Jason**, **Raymond**, **Jenny**, **Shannon**, **Leonie**, **Mariya**, **Bas**, and **Lodi** you are all amazing and your help along the way to our shared goal was invaluable.

Beyond permanent staff there are also all of the other students around at Qutech that have completed the culture here. Joining various organizations here like the Qutech speakers, and the QINC social team has been a wonderful experience. I was lucky to cross paths with you there **Max**, **Joe**, **Francisco**, **Sjoerd**, and **Yanik**. I also want to specifically thank **Matthew**, **Matteo**, **Mohammed**, **Nina**, **Jaap**, **Yanik** and **Max** for the sporadic research work and conversations we shared over the years that proved essential. To those of you from around the coffee table, throughout the halls and labs, and even at the Leiden 10k **Connor**, **Matteo**, **Sophie**, **Willemijn**, **Pablo**, **Guus**, **Tim**, **Hans**, **Julia**, **Marie-Christine**, **Arian**, **Siddharth**, **Francesco**, **Lukas**, **Damian**, **Nicholas**,**Hans**, **Siddhant**, and **Maarten** thank you all. You are a great community, that I consider my self lucky to be a part of.

Speaking of luck I was also lucky to have the support of my group here in Delft. To the masters students around **Jorge**, **Oriol**, **Shenke**, and **Elsie**, it was great to work with you all and hear about the interesting work you were up to in our lab. I hope I get to hear about your adventures in research going forwards. To postdocs and past lab memebers, you were the ones around both in Delft and in Calgary to learn from. **Gustavo**, **Sara**, **Josh**, and **Qiang** thank you for everything you have taught me through the years. To the previous students in the group **Neil**, **Thomas**, **Raju**, and **Marcel.li** I would not be nearly the researcher I am today without the foundation of skills that I learned from all of you. **Iraji** You were the other guy who made the trek from Canada to Europe. Having you around as a friend and co-worker through the transition made everything easier. I cannot wait to see what you get up to with your career. To **Tanmoy**, **Dorian** and **Nir** I am in your debt. Throughout all of the pandemic you have been family here in Delft as much as my own so far away. I would never have survived the past year without you.

There is a special bond formed from years of work and research with people around you. **Mohsen** we have had ups and downs throughout our years together both in Calgary and in Delft. You are a true friend and I wish you nothing but the best. I hope we will even cross paths in Philly or Toronto someday. **Anta**, we have spent way too many hours together over the last few years, but I value all of those moments. You have been a good friend whether during work, dancing to music from home, or out in Frankfurt. I am excited to see Dinhata.

A group is nothing without the man with a plan who assembled the whole thing. Thank you **Wolfgang**. You have given me quite an opportunity in working for you and I will always be thankful for it. I have seen your group through many stages over our past 5+ years together and I wish you great (again!) success with your work going forwards.

From a professional perspective I think that is everyone. But I could also not have done this without my closest friends across the world. I am thankful to have all of you in my life. **David** You have been my best friend since we were 6. Nothing has changed that through this tough period while I have lived so far away. I hope we get to see a bit more of each other soon, especially as Lexi starts growing up. To the Wuncher guys, we are far flung, but **Alex**, **Tori**, and **Jacob** I love you guys. The league is the highlight of my fall every year and I am sure I will see more of you in person soon. To my Madison men, **Andrew** and **Kyle** you are great friends. Andrew I hope we get called in for another impromptu virtual trivia night sometime soon. **Kim**, you were a great roommate and remain a dear friend. You future looks bright and I hope it crosses paths with mine either professionally

8

and personally going forwards. To the Calgary contingent, **Garret** and **Matt**, I thought that we would all have a few more years to get up to some great backcountry hijinks when I found out I would be moving. I hope we get the chance to head out together again skiing, climbing, kayaking, playing polo, or even for a Trifecta!

Lastly, and thus most importantly, come the family. **Stephen** and **Mimi** You put me up for months while I was working in Calgary. You truly feel like my pseudo-parents once removed or something like that. It was wonderful to discover you and get to know you over the years there and I hope to see you again soon. **Alex** Thank you for putting up with this degree that turned into something more difficult for us than I had ever imagined. I love you tons and I cannot wait to jump headfirst into this next year together. Your love and support has been a keystone that has held me soundly together throughout my work over our last 6+ years together.

Finally, **Mom** and **Dad** you are the reason I am here. I have gotten my world from you. **Karen** from you I got my inquisitive nature and deep engagement with the world and people around me. The idea of questioning, digging and condensing knowledge like your stories of law school has always stuck with me throughout my work over this degree. Alongside this, you always encouraged in me to have a deep sense of myself, my valuable relationships, and a love of genuine interaction with everyone around me. **Marc** from you I got my perseverance and my love for hands on science. The idea of taking responsibility and doing things the right way are all from you. You always taught me to carry on with it despite hard work and dirty hands. Acting as mechanics in the driveway has been an inspiration for me to pursue all of my work. I have the drive that I do today from the input and encouragement you both gave to me throughout my life. Thank you both for everything.

LIST OF PUBLICATIONS

6. *Spectral population dynamics of thulium doped yttrium gallium garnet,*
Jacob H. Davidson[1], Antariksha Das[1], Nir Alfasi, and Wolfgang Tittel
In preparation, tentative title.

5. *Optical properties of thulium doped yttrium gallium garnet,*
Jacob H Davidson, Dorian Oser, and Wolfgang Tittel
In preparation, tentative title.

4. *Measurement of the thulium ion spin Hamiltonian in an yttrium gallium garnet host crystal,*
Jacob H Davidson, Philip JT Woodburn, Aaron D Marsh, Kyle J Olson, Adam Olivera, Antariksha Das, Mohsen Falamarzi Askarani, Wolfgang Tittel, Rufus L Cone, Charles W Thiel,
Phys. Rev. B **104**, 134103 (2021). Featured as an editor's suggestion.

3. *A long-lived solid-state optical quantum memory for high-rate quantum repeaters,*
Mohsen Falamarzi Askarani[1], Antariksha Das[1], **Jacob H Davidson**, Gustavo C Amaral, Neil Sinclair, Joshua A Slater, Sara Marzban, Charles W Thiel, Rufus L Cone, Daniel Oblak, Wolfgang Tittel,
Phys. Rev. Lett. **127**, 220502 (2021).

2. *Improved Light-Matter Interaction for Storage of Quantum States of Light in a Thulium-Doped Crystal Cavity,*
Jacob H Davidson, Pascal Lefebvre, Jun Zhang, Daniel Oblak, Wolfgang Tittel,
Phys. Rev. A **101**, 042333 (2020).

1. *Entanglement and nonlocality between disparate solid-state quantum memories mediated by photons,*
Marcelli Grimau Puigibert[1], Mohsen Falamarzi Askarani[1], **Jacob H Davidson**, Varun B Verma, Matthew D Shaw, Sae Woo Nam, Thomas Lutz, Gustavo C Amaral, Daniel Oblak, Wolfgang Tittel,
Phys. Rev. Research , **2**, 013039 (2020).

[1] These authors contributed equally to this work

CURRICULUM VITÆ

Jacob Harley DAVIDSON

08-09-1992 Born in Philadelphia, Pennsylvania, USA.

EDUCATION

1998-2011 Friends School Haverford and Friends Central, Philadelphia, PA, USA

2011–2015 Undergraduate in Mathematics & Physics
Thesis: "*Gravitational Waves and Polarization of the Cosmic Microwave Background*"
Under supervision of Dr. Seth Major
Hamilton College, Clinton, NY,USA

2015 - 2016 Buisness Intelligence Developer Epic Systems Corperation
Madison, WI, USA

2016 - 2018 MSc. Physics and Astronomy, University of Calgary, Alberta, Canada
Thesis: "*Storing Quantum Correlations in Different Rare Earth Ion-doped Solids*"
QC2 Lab under supervision of Prof. Wolfgang Tittel

2018 - 2022 Doctorate in experimental Quantum Physics
Delft University of Technology, Delft, The Netherlands
Thesis: Thulium doped Garnets for Quantum Repeaters and Optical Quantum Memory
Promotor: Prof. dr. W. Tittel

2018 Visiting Researcher, University of Calgary, Alberta, Canada
Cavity based Quantum Memory in a Thulium Doped Crystal
Quantum Cloud Lab under supervision of Dr. Daniel Oblak

2020 Visiting Researcher, Montana State University, Bozeman, MT, USA
Measurement of Rare Earth Ion hyperfine tensors
Cone/Thiel Lab under supervision of Dr. Charles Theil and Prof. Rufus Cone